MATURATION AND IMPLEMENTATION OF HUMAN INDUCED PLURIPOTENT STEM CELL DERIVED CARDIOMYOCYTES FOR MODELING CARDIAC DISEASE

By

Shan S. Parikh

Dissertation

Submitted to the Faculty of the

Graduate School of Vanderbilt University

in partial fulfillment of the requirements

for the degree of

DOCTOR OF PHILOSOPHY

in

Pharmacology

June 30, 2018

Nashville, Tennessee

Approved:

Björn C. Knollmann M.D., Ph.D. (Mentor)

Dan Roden M.D. (Committee Chair)

Eric Delpire Ph.D.

Charles C. Hong M.D., Ph.D.

David Weaver Ph.D.

This work is dedicated to my parents, who strove to provide the best academic opportunities, my brother who inspired me to pave my own way, and especially Meghana, who has been unconditionally encouraging.

ACKNOWLEDGEMENTS

During my graduate studies, I have been fortunate to train at two highly accredited academic institutions. My pursuit of a career as a physician-scientist provided me a multi-institutional experience influenced by numerous excellent mentors. I am grateful to Temple University School of Medicine and Dr. Thomas Force and Dr. Hind Lal, my past mentors, with whom I began this journey. In addition to exposing me to the power of a center-based approach for facilitating multidisciplinary research, my experiences at the Center for Translational Medicine at Temple inspired me to pursue a career investigating therapeutic strategies for combating heart failure.

I then transferred to Vanderbilt with my past mentor Dr. Thomas Force, who encouraged me to complete my graduate studies with him. It was here I discovered the Department of Pharmacology and the enriching environment within, which provided me a foundation in receptor theory (Dr. Seva Gurevich and Dr. Terry Kanakin), pharmacokinetics, and drug metabolism (Dr. Scott Daniels). However, due to the unfortunate retirement of my mentor after completion of my qualifying exam, I embarked on identifying a new mentor. The training set forth by the Pharmacology Department enabled me to persevere in light of the limitations encountered during this lab change. In addition, it was during my classwork in Pharmacology where I met my current mentor, Dr. Bjorn Knollmann.

I am especially grateful for Dr. Knollmann, who provided me an opportunity to finish my graduate studies in his laboratory. Aside from including me in his team assembled with generous, passionate, and patient scientists, he helped re-align my career goals after transitioning to a new lab. His team was exceedingly patient in training and teaching me technical aspects of conducting research. Dr. Lili Wang was especially helpful, as we spent countless hours debating optimization of cardiomyocyte differentiation and strategies for successful gene editing. In addition, her willingness to share her expertise and try new ideas was essential to experiments performed in both chapters of this thesis. Her constant presence in the lab and dedication to her projects helped build my work ethic. Dr. Kyungsoo Kim shared his expertise in use of the IonOptix instrument and learning from him helped me pay more attention to detail. Dr. Nieves Gomez-Hurtado was an essential component for my transition to Vanderbilt as I learned molecular biology and in-vivo techniques for arrhythmia interrogation from her. More importantly, her constant critique encouraged me to be more critical myself. Dr. Dima Kryshtal provided electrophysiological expertise and he has always taken time to explain relevant aspects of patch clamping. Dr. Dan Blackwell was supportive both in acquisition of data and in moral support, as I was fortunate to share an office area with him. I have further improved my scientific approach through observing his attention to detail and experimental design, which has been indispensable for my training. Kaylen deserves many thanks as she was instrumental in daily aspects of my laboratory needs. Not only did she ensure I had required reagents, but she was always willing to problem-solve and assist in resolving new issues that surfaced during my training. Other members of the team including Drs. Chris Johnson and Frank Raucci, and Beau were also incredibly supportive during my time in the lab.

I consider the Roden and Wells Lab a part of this wonderful network- Drs. Andrew Glazer and Kevin Bersell helped me troubleshoot my experiments and career trajectory, while Marcia Blair helped train me when I joined. Christian Shaffer was integral in accelerating our analysis of Cardioexcyte96 data as he generated data conversion tools which saved a lot of time. The work in **Chapter 2** was made possible by the Wells lab, as Dr. Quinn Wells recruited the family with dilated cardiomyopathy that I am studying. I am thankful for the participation of the family members in this study and grateful for their permission for

generation of human induced pluripotent stem cells for our investigation. Overall, I am extremely fortunate to have joined such a valuable network of helpful and kind individuals. They made the remainder of my graduate studies more enriching than I could have ever imagined.

I would also like to thank my committee members, Drs. Dan Roden, Eric Delpire, Charles Hong, and David Weaver for providing guidance and support during my transition into a new lab and facilitating completion of my graduate studies. Their understanding and willingness to help was very much appreciated. Dr. David Weaver was my connection to high-throughput screening and not only did he provide an excellent experience- but he influenced my gravitation to the Cardioexcyte96, which was widely used during my graduate studies. Dr. Delpire showed great kindness and patience while providing guidance on gene editing techniques, which subsequently led to my successful generation of the first autosomal dominant mouse model of CPVT (Casq2K180R). I also appreciate the many career related discussions with Dr. Hong who provided an alternative perspective to research in academia.

Lastly, I would like to acknowledge my support from the National Institute of General Medical Sciences T32 GM07347, T32 GM07628, and National Heart, Lung, and Blood Institute F30 HL131179. This work was supported, in part, by grants from the US National Institutes of Health (R01HL71670, R01HL128044, R01HL124935, P50GM115305, and U01HL131911) to my mentor B.C. Knollmann.

TABLE OF CONTENTS

LIST OF TABLES

Page

LIST OF FIGURES

ABBREVIATIONS

Bin-1	bridging integrator-1
Ca^{2+}	Calcium
Cas9	Clustered Regularly Interspaced Short Palindromic Repeats-associated protein 9
Casq2	Calsequestrin
Cav-3	caveolin 3
CHIR	CHIR99021 GSK3α/β inhibitor
CICR	calcium induced calcium release
CIPA	Comprehensive *In-vitro* Proarrhythmia Assay
CM	cardiomyocyte(s)
CRISPR	Clustered Regulatory Interspaced Short Palindromic Repeats
DCM	dilated cardiomyopathy
Dex	dexamethasone
EC	excitation-contraction
ECC gain	excitation-contraction coupling gain
ECM	extracellular matrix
EF	ejection fraction
EFP	extracellular field potential
FDC	familial dilated cardiomyopathy
FFT	fast Fourier transform
FPD	field potential duration
HDR	homology directed repair
HF	heart failure

hiPSC	human induced pluripotent stem cell(s)
hiPSC-CM	human induced pluripotent stem cell derived cardiomyocyte(s)
hPSC	human pluripotent stem cell(s)
I_{K1}	inward rectifier potassium ion channel
I_{Kr}	rapid activating potassium ion channel
I_{Ks}	slow activating potassium ion channel
IMP	Impedance
I_{Na}	sodium current
ICH	International Council for Harmonization of Technical Requirements for Pharmaceuticals for Human Use
Jph2	junctophilin 2
LMNA	lamin A/C
LTCC	L-type calcium channels
NCX	sodium/calcium exchanger
NHEJ	non-homologous end joining
NRVM	neonatal rat ventricular myocyte
PAM	protospacer adjacent motif
PMCA	plasmalemmal calcium ATPase
PTC	premature termination codon
qRT^{2}PCR	quantitative reverse transcriptase polymerase chain reaction
RLFP	restriction length fragment polymorphism
RT	room temperature
RyR2	ryanodine receptor

SCD	sudden cardiac death
SERCA	sarcoplasmic reticulum calcium transport ATPase
ssODN	single stranded oligonucleotide
sgRNA	single guide RNA
SR	sarcoplasmic reticulum
T3	triiodo-L-thyronine
TALENs	Transcription Activator-like Effector Nucleases
TdP	Torsades de Point
TNNT2	cardiac troponin-T
TR	thyroid receptor
Trdn	triadin
VUS	variant of unknown/uncertain significance
ZFN	Zinc-Finger Nucleases
$\tau 1$	time constant indicating voltage dependent inactivation of LTCC
$\tau 2$	time constant indicating calcium dependent inactivation of LTCC

CHAPTER 1

INTRODUCTION

1.1 Overview

The two predominant driving forces that maintain the heart as a central focus for intensive investigation include: 1) the statistic that cardiovascular disease is the leading cause of death worldwide[1] and 2) a majority of drug attrition is due to cardiovascular toxicity[2]. While the cause of death from cardiovascular disease ranges from sudden cardiac death to primarily heart failure, the high rates of drug attrition are largely attributed to potential cardiac toxicity[2, 3]. Despite the growing population of patients with heart failure, which is projected to rise 46% by 2030[1], cardiovascular drug development has continued to decrease, evidenced by a 33% decline in newly approved cardiovascular drug therapies since 2000-2009[4]. Although financially motivated justification are primarily responsible for failures in cardiac drug development, failures due to toxicity and limited efficacy remain equally important[5]. Current methods for investigating cardiac disease and drug toxicity primarily rely on mouse models and heterologous expression systems. However, these tools are not always reliable models of human disease nor do they accurately reflect toxicity in humans[6-8]. Despite the genetic similarity of mice and humans, gene expression and associated gene networks responsible for determining cellular function and response are quite different[9-11]. This is evident by differences in electrophysiological properties in the mouse versus human (e.g. the heart rate is 600 beats per minute in a mouse in contrast to 70 beats per minute in a human)[12]. Limitations of animal models for studying human disease have accelerated efforts to supplement animal models with more relevant human cellular models[13-15]. Recent technological advances in the generation of human induced pluripotent stem cell derived cardiomyocytes (hiPSC-CMs)[16] has facilitated their implementation in both academia[17, 18] and industry[19, 20] such that these cells are considered a revolutionary tool for reducing drug attrition and enhancing translation of cardiac disease findings.

In this introductory chapter, I first review hiPSC technology and its current applications relevant to cardiomyocytes (CM) and cardiac disease. The current limitations of existing hiPSC-CM and subsequent implications that reduce their implementation are also discussed. Next, the cardiac physiology relevant to the use of hiPSC-CM is reviewed, followed by a brief overview of dilated cardiomyopathy (DCM) and the use of hiPSC-CM for its investigation.

1.2 Human Induced Pluripotent Stem Cells

The development of reliable human *in-vitro* cellular models has remained an unmet need in both academia and industry for drug screening, disease modeling, and cardiac toxicity assessment. Although primary human cardiomyocytes of high quality would be ideal, limited availability and difficulty in their use prevent widespread utilization. Alternatively, stem cells provide a suitable starting material for producing cardiac cells; however, stem cells derived from embryonic sources have generated ethical concerns, limiting their development. Thus, the discovery that human induced pluripotent stem cells (hiPSC) can be derived from somatic adult cells has revolutionized our use of human cells, because the iPSC technology allows for an unlimited production of human derived cells, free from the ethical concerns surrounding use of human embryos.

The Yamanaka laboratory first defined 4 key factors, Oct3/4, Sox2, c-Myc, and Klf4 which were sufficient for reprogramming fully differentiated mouse and human cells to their pluripotent precursor, termed pluripotent stem cell (PSC)[21, 22]. Reprogramming somatic cells into the pluripotent state allows for indefinite self-renewal and the potential for tri-lineage differentiation (endoderm, ectoderm, and mesoderm). Subsequent efforts by others identified methods for reprogramming a multitude of somatic cells. Typical examples are mononuclear peripheral blood cells[23], urine cell isolates[24], extra-embryonic tissue[25], and fibroblasts[22]. Methods for delivery of reprogramming agents originated with low efficiency viral vectors which require integration into the genome[26]. Due the safety concerns of genomic integration and potential tumorigenicity, non-integrating methods have been developed ranging from use of recombinant proteins[27] to small molecule approaches[28] **(Figure 1)**. Recent efforts have focused on trans-differentiation methods, which allow for rapid conversion of one cell type directly into another cell type without having to pass through a pluripotent precursor[29]. The generation of hiPSC from various cell types is becoming a routine laboratory protocol; however, concerns regarding hiPSC quality and “stemness” have stimulated the development of guidelines surrounding generation and validation of hiPSC. The current consensus is that proper characterization of hiPSC should include validation of pluripotency as evidenced by self-renewal and expression of associated markers, tri-lineage differentiation capacity, genomic stability via karyotyping, and recently suggested assessment of epigenetic stability[30]. With the rapid adoption of hiPSC technology and initiation of large-scale banking of disease and gene edited hiPSC lines, its use in biomedical research is on an upwards trajectory.

1.3 Gene Editing in hiPSC

Generation of disease mutation containing hiPSC lines and comparison against unrelated population controls has been widely performed, and are especially important in studying the impact of genetic background or additive mutations. However, these studies are limited by line-to-line variability and require a large number of population and disease lines to generate confidence in findings. Simultaneous advances in the field of gene editing now allow for the introduction of genetic modifications in hiPSCs for creation of isogenic lines for comparison. These include: **1)** generation of disease lines on a characterized and well-established population control or **2)** correction of mutation-causing disease line. In **Chapter 2**, CRISPR/Cas9 was used to correct a disease-causing mutation in a patient-derived hiPSC. The following provides a background on gene editing, a brief overview of the framework used for gene editing in **Chapter 2**, and limitations that guided experimental strategies for successful gene editing.

Methodologies for gene editing include Zinc-Finger Nucleases (ZFNs), Transcription Activator-like Effector Nucleases (TALENs), and Clustered Regulatory Interspaced Short Palindromic Repeats (CRISPR)/CRISPR-associated protein (Cas9)[31, 32]. Due to the ease of use and efficiency of CRISPR/Cas9, it has become the gene editing tool of choice and is supported by user friendly, free online design tools and resources[33]. CRISPR/Cas9 based gene editing is modified from a microbial adaptive immune system which employs a RNA-guided nuclease to destroy foreign genetic elements[34]. Although six systems exist, the Type II system is the most characterized and best used for gene editing (**Figure 2**)[35]. The two-component system includes: Cas9, a nuclease responsible for DNA cutting, and the single guide RNA (sgRNA) which contains a targeting sequence (crRNA sequence) and a Cas9 nuclease recruiting sequence (tracrRNA). The crRNA contains a 20-nt guide sequence which is homologous to the targeted region in a gene of interest and guides the Cas9 nuclease activity. The tracrRNA provides secondary structure that is required for the crRNA-tracrRNA complex to activate the Cas9 nuclease[35]. The target DNA must immediately precede a 5’-NGG termed the protospacer-adjacent motif (PAM) and is essential for

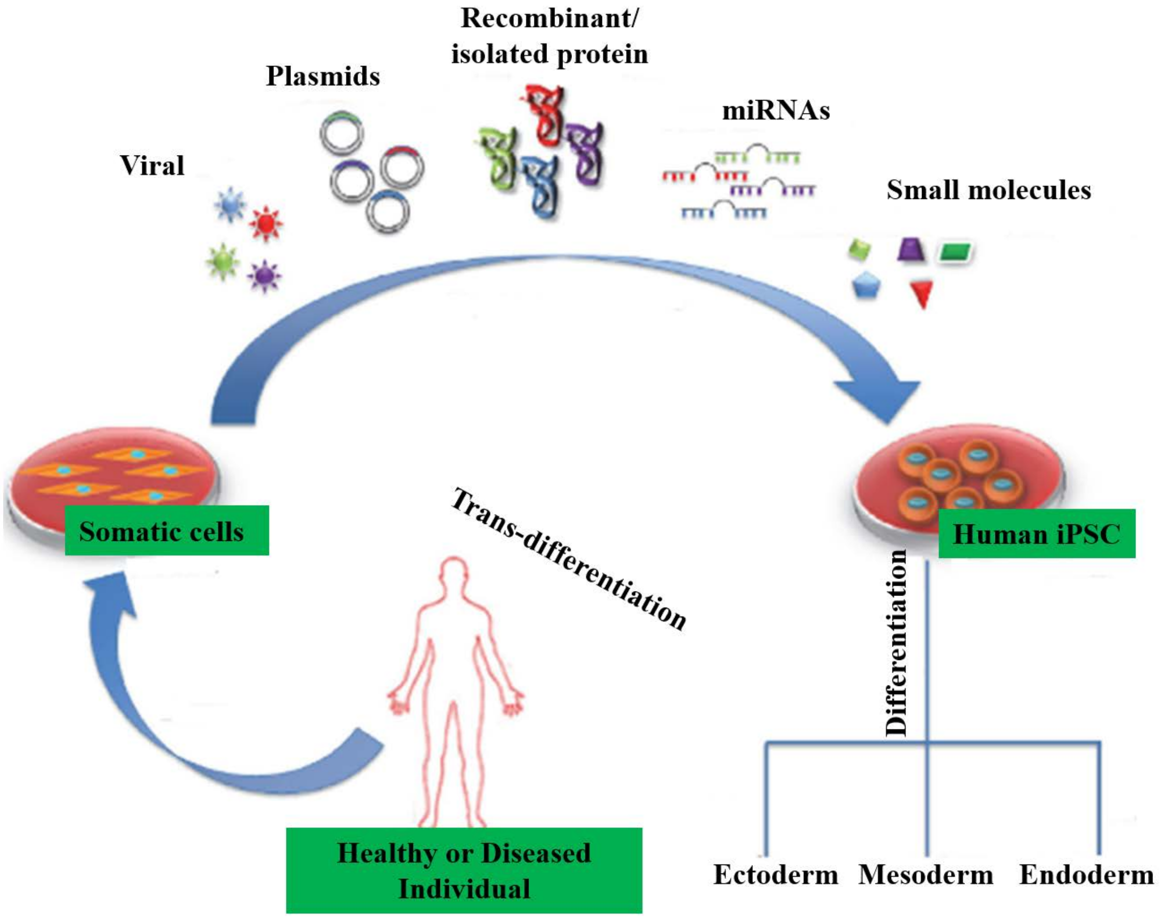

Figure 1: Workflow for generation of human induced pluripotent stem cells (hiPSC). Somatic cells are isolated and reprogrammed into hiPSC through various methods ranging from viral transduction, plasmid based approaches, use of recombinant proteins, to miRNA and small molecule transfection. Reprogrammed cells now possess tri-lineage potential and can be differentiated as needed. Alternative approaches allow for small molecule based trans-differentiation. Figure modified from[36].

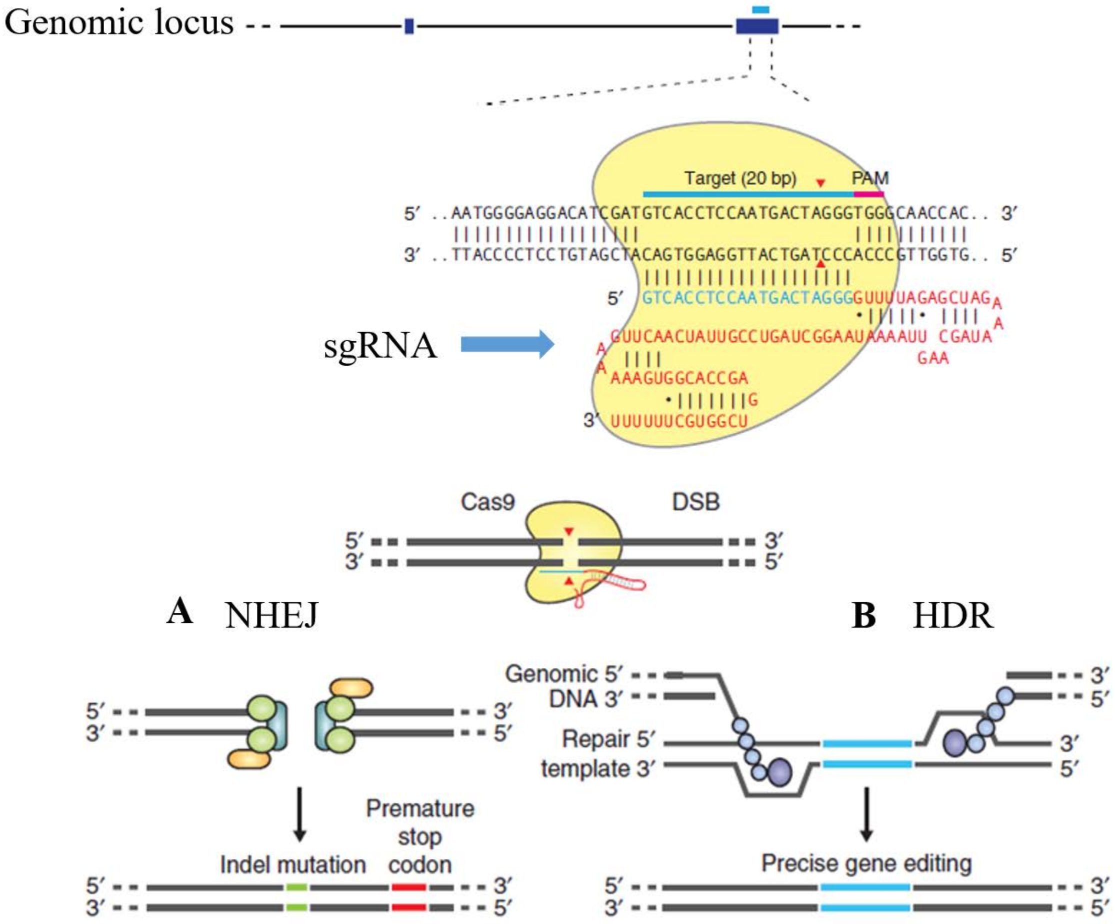

Figure 2: **Schematic of CRISPR/Cas9 mediated gene editing.** The Cas9 nuclease from Streptococcus pyogenes (depicted in yellow) is targeted to the genomic region of by the sgRNA, consisting of a 20 nucleotide sequence homologous to the genomic region being targeted. Directly upstream is a critical 5’ NGG sequence noted as the PAM sequence. Cas9 mediated nuclease activity results in a double stranded DNA break 3 base pairs upstream of the PAM sequence. Upon DNA cleavage, two distinct DNA repair pathways can occur: **A)** Non-homologous end joining (NHEJ) or **B)** Homology directed repair (HDR). NHEJ can generate an insertion or deletion resulting in a premature stop codon. In the presence of a suitable repair template, HDR can generate the designed gene edit from the template. Figure modified from [35].

Cas9 binding to the DNA. Cas9 mediated DNA cleavage at this region results in a double stranded break and subsequent activation of non-homologous end joining (NHEJ) or homology directed repair (HDR). NHEJ is error prone and commonly used for generation of an insertion/deletion at the site of cutting: ultimately resulting in a premature stop codon and is therefore useful for generating gene knockout models. Alternatively, HDR allows for precise genomic editing in the presence of exogenous DNA (repair template) and useful for generation of knock-in models.

The workflow for use of CRISPR/Cas9 technology for gene editing of hiPSC as performed in this thesis are described in **Figure 3**. Briefly, in-silico design of a gRNA (the targeting sequence) with maximal predicted cutting efficiency and minimal off-target cutting is performed. A plasmid-based approach is used to deliver gene editing machinery for expression of the Cas9 and the sgRNA into the hiPSC. Successfully transduced hiPSC can be selected by incorporating an antibiotic resistance gene or fluorescent tag into the plasmid. Although non-plasmid based approaches for delivering Cas9 mRNA or protein into the hiPSC are more efficient[37], the use of a plasmid encoding a selection marker facilitates identification of successfully edited cells. For HDR, the plasmid and repair template is electroporated into the hiPSC. Following clonal selection via antibiotics or other selection method, single colonies are picked and expanded prior to identification of colonies with required mutation. As a restriction enzyme site can be incorporated into single stranded oligonucleotide (ssODN) using a silent mutation, restriction length fragment polymorphism (RLFP) can be used to identify clones with successful HDR. Verified clones are then differentiated into cell type of choice for further characterization.

While utilization of CRISPR/Cas9 system for mammalian gene editing is rapidly evolving, use of current techniques results in poor HDR meditated repair efficiency, estimated at less than 1%[38]. In addition, off-target activity of gRNAs further limits successful generation of gene edited

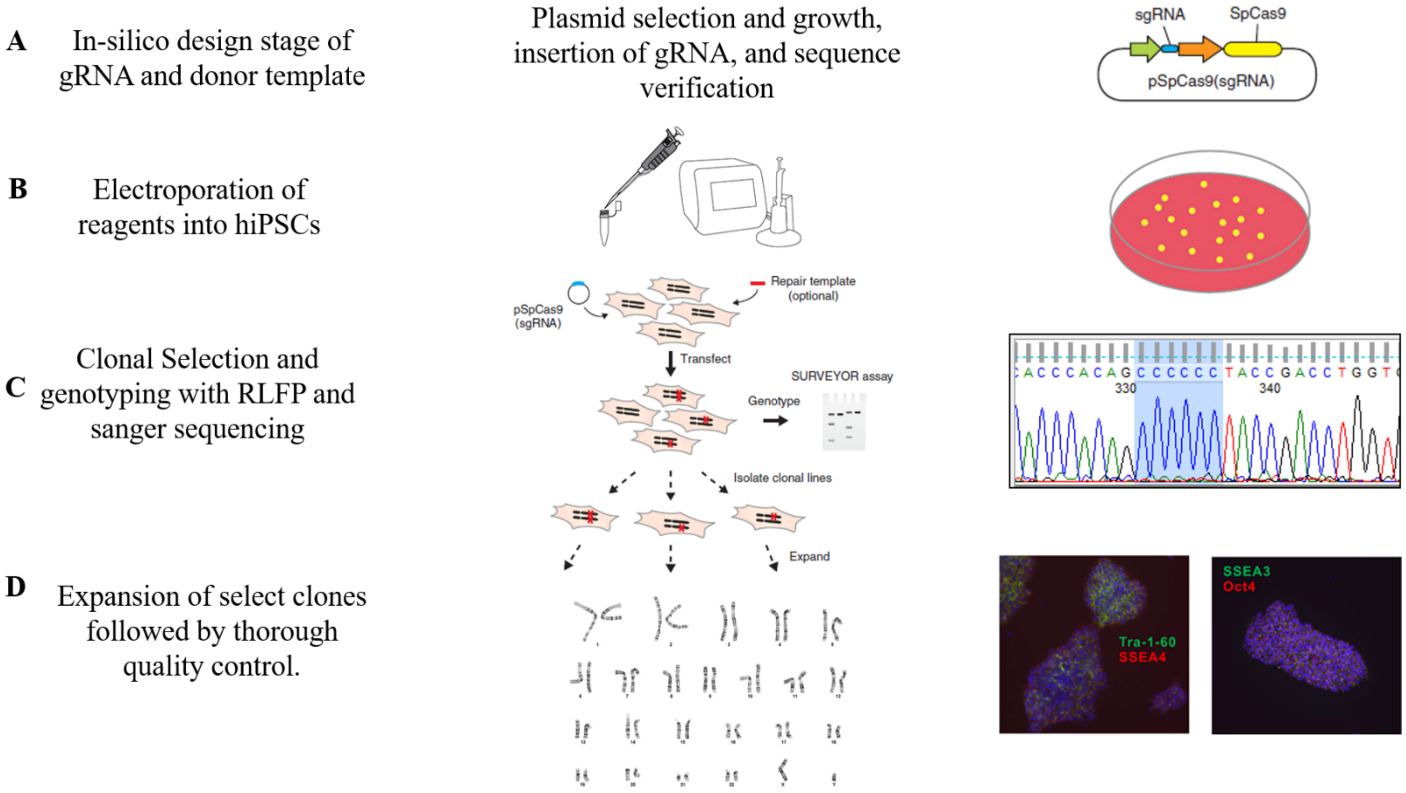

Figure 3: Workflow for CRISPR/Cas9 mediated gene editing. A) In-silico design of a gRNA with maximal predicted cutting and minimal off-target cutting is performed using online tools. For hiPSC, a plasmid- based approach is commonly used for expression of Cas9 and sgRNA. Once gRNA has been incorporated into specified plasmid-containing Cas9, surrounding nucleotides encoding the full length sgRNA, and a selection cassette, it is sequence verified and prepared for electroporation. **B)** Depending on the goal of the gene editing (knockout or knockin), either the plasmid alone or plasmid with repair template in the form of an ssODN, is electroporated into hiPSCs. **C)** Clones are selected using antibiotics, single colonies are manually picked and expanded, and restriction length fragment polymorphism (RLFP) for identification is used to identify colonies with the designed mutation. Sanger sequencing is used to ensure purity of genetic change. **D)** Select clones are expanded followed by quality control. Examples shown are karyotyping and immunohistochemistry for markers of pluripotency Tra-1-60, SSEA4, SSEA3, and Oct4. Verified clones are differentiated and functionally characterized. Figure adapted from [35, 39].

lines. Strategies to combat these deficiencies currently emphasize proper design and methods for enhancing rates of HDR and inhibit NHEJ[40]. While inhibiting NHEJ has demonstrated variable results and requires pharmacological targeting[41] or manipulation of gene expression pathways[42], changes in design strategies are benign and easy to incorporate into standard workflow **(Figure 4).** Incorporation of blocking mutations in the repair template can enhance accuracy of editing 10-fold[38]. The absence of blocking mutations is known to increase rates of target re-cutting followed by NHEJ causing unwanted insertions/deletions, thus further reducing repair efficiency. Additionally, the further away the cut site is from the mutation, the lower the efficiency of repair, with one study showing efficiency dropping by half with a distance of 10 nucleotides[38]. Furthermore, studies show that a preferential production of heterozygous vs homozygous mutations can be performed by manipulating the distance between the cut site and mutation[38]. Additional strategies for enhancing Cas9-mediated HDR frequency include rational design of the symmetry and length of the donor ssODN. Significantly higher efficiency of HDR has been demonstrated when using optimal repair template length ranges between 80-100 nucleotides with 36-40 bases of homology on adjacent sides[38, 43, 44]. Multiple studies also provide evidence for the design of asymmetric donor templates where there is a shorter 3’ end with ~30 bases and a long 5’ arm with ~60 bases[43, 44]. Although much of the published work on enhancing HDR efficiency uses cell lines, such as HEK cells, findings of rational HDR design have been successful reproduced in hiPSCs. As low efficiency of HDR is a major limitation of the use of CRISPR/Cas9 based gene editing in hiPSC, methods for increasing HDR efficiency are needed for advancing the use of this technology.

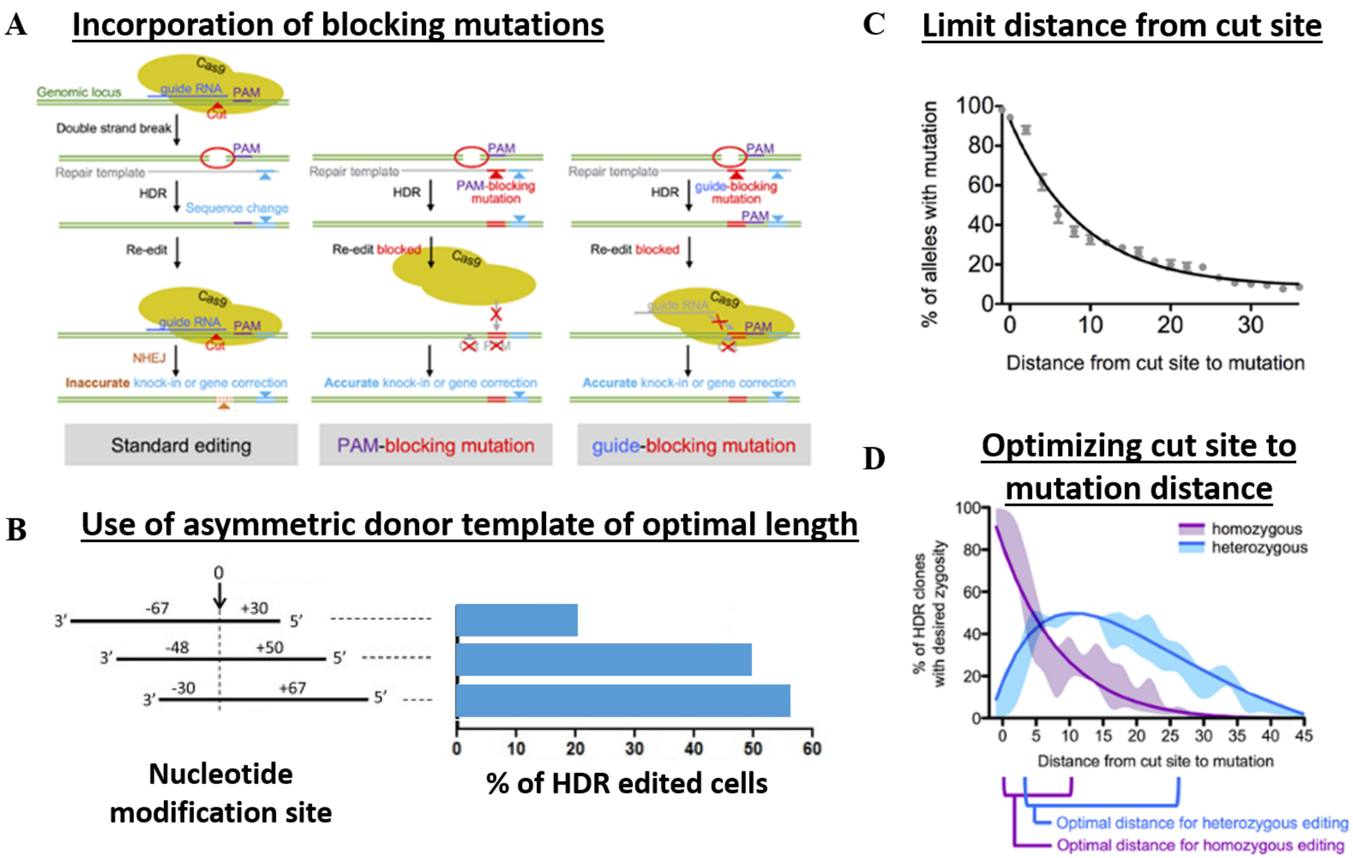

Figure 4: Strategies for optimal donor template design. A) Incorporation of blocking mutations and predicted consequence on HDR mediated repair. **B)** Impact of asymmetric repair template design on edit success rate. Graphical illustration based on data from [43, 44]. **C-D)** Pictorials demonstrating the need for rationale selection of distance between cut site and mutation site. The data suggests an exponential decline in efficiency of repair with greater distances between two sites. Recommendations based on data from [38] and image adapted from addgene.com.

1.4 Differentiation of hiPSC into cardiomyocytes

Spontaneous differentiation of human embryonic stem cells into embryoid bodies with contracting cells provided proof of concept for the possibility of *in-vitro* production of human CM[45]. Shortly thereafter, protocols for directed differentiation of pluripotent stem cells were developed using co-culture methods with mouse visceral endoderm cells[46]. Although early protocols were inefficient and generated a low yield of hiPSC-CM, they provided key insights for further improvement. Steps taken towards enhanced differentiation started with the removal of FBS, addition of L-ascorbic acid, and removal of insulin during the initiation of cardiac differentiation[47, 48]. Building upon these improvements, current methods for hiPSC-CM differentiation include a directed embryoid body method and monolayer method[49]. Both methods require generation of sequential environments intended to replicate signaling changes during fetal cardiac development [49, 50]. The embryoid body method requires a forced aggregation of hiPSCs. This method is limited due to its technical difficulty and lower hiPSC-CM yields. Chemical differentiation using the monolayer method (**Figure 5**) is currently the most widely adopted protocol due to its relatively high efficiency and reproducibility and is the method used to generate hiPSC-CM in this thesis[51, 52]. In this method, hiPSCs are maintained on 1:200 diluted Matrigel substrate in defined media such as Essential-8 media or mTeSR1, which supports pluripotency. The efficiency of CM differentiation is dependent on the starting cellular confluence of the hiPSCs, however; optimal confluence can vary between cell lines. To optimize efficiency of differentiation many users recommend identifying an optimal cell confluence for each cell line[52]. At a cellular confluence generally between 60-90%, cardiac induction toward the mesodermal lineage is initiated using a GSK3α/β inhibitor CHIR99021 (CHIR) in a basal media RPMI supplemented with B27 minus insulin. After three days, cells are exposed to the WNT inhibitor IWR1 for differentiation into the CM lineage. Glucose starvation is employed at days 10-16 to increase the fraction of cardiomyocytes, taking advantage of the glucose reliance of non-myocytes. Starting from days 16 to 30, hiPSC-CM are maintained in RPMI with glucose + B27 with insulin. Differentiations can be variable across hiPSC lines but this protocol is reported to generate 90% cardiac troponin-T (TNNT2) expressing CM[51, 53]. Although differentiation efficiency is regularly reported to be as high at 70-90% TNNT2+, internal variability among differentiations remains high and requires lab-to-lab quality control efforts to standardize the quality of differentiations. As variability of differentiation drives both purity (cardiomyocyte-like vs fibroblasts) and quality (cellular maturity) of hiPSC-CM, further optimization remains necessary to generate high yields of structurally and functionally mature hiPSC-CM.

1.5 Primary applications of hiPSC-CM and limitations

Current use of hiPSC-CM falls into three major categories: 1) evaluation of drug induced cardiac toxicity, 2) disease modeling, and 3) regeneration of the injured myocardium. The combination of gene editing and increasing ease of generation of hiPSC-CM has enabled advancements in each application. Although human pluripotent stem cell (hPSC) derived from embryonic stem cells are still used, the majority of the following studies focus on use of hiPSCs. The use of hiPSC-CM for evaluating drug induced cardiac toxicity is a concerted effort between industry and regulators who are currently developing revisions to international recommendations on pre-clinical cardiac safety assessment. Guidelines led by the International Council for Harmonization of Technical Requirements for Pharmaceuticals for Human Use (ICH), finalized in 2005, were devised in response to the skyrocketing cases of drug induced arrhythmias (termed Torsades de Point (TdP)) in the early 1990s[54]. Of these guidelines, ICH S7B details the non-clinical

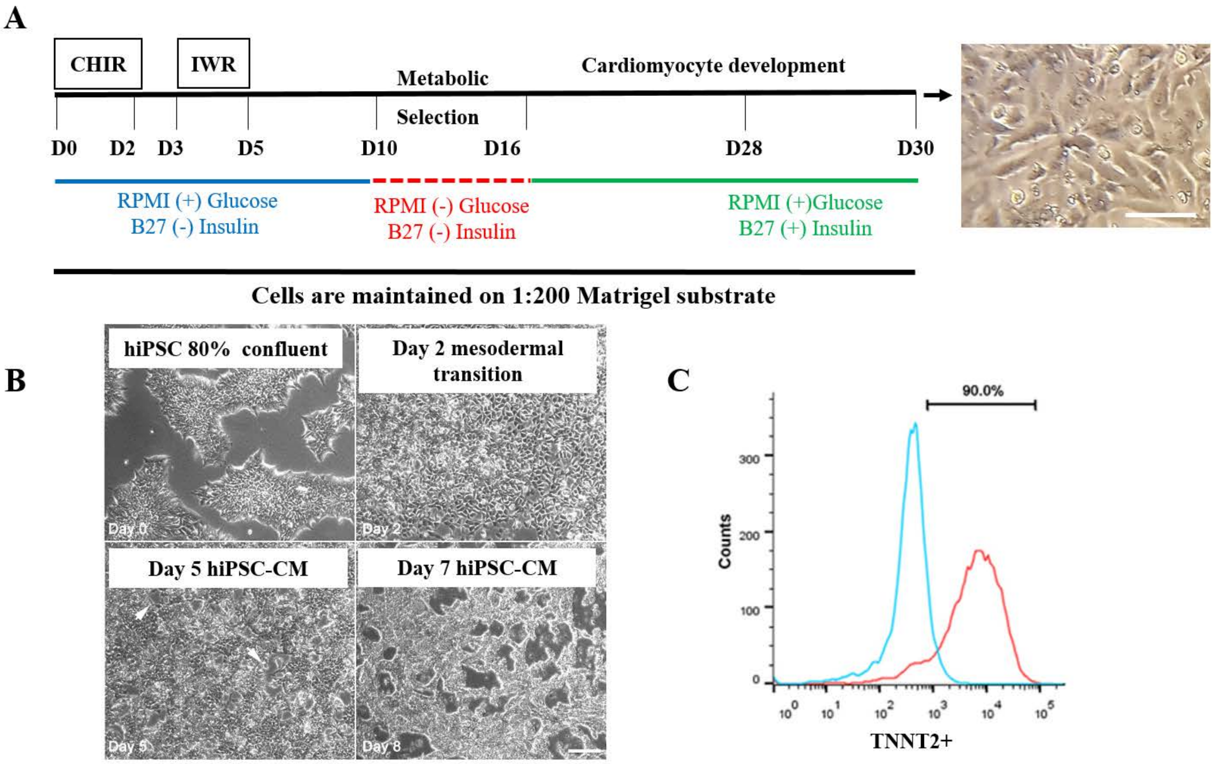

Figure 5: Monolayer method for generation of hiPSC-CM. A) Chemical differentiation protocol for cardiac induction and maintenance with representative day 30 hiPSC-CM in monolayer (scale bar = 100 µm). Cells are maintained on a 1:200 Matrigel substrate during this process. Although cells can generally be used for applications after day 21, many labs prefer to utilize cells at day 30 onwards. CHIR99021 indicates GSK3α/β inhibitor, IWR-1 indicates Wnt antagonist. **B)** Bright field images tracking hiPSC induction into mesoderm to differentiation into CM between days 0 to 8 (scale bar = 200 µm). **C)** Flow cytometric analysis showing up to a 90% TNNT+, demonstrating high purity of CM. Images for B and C adapted from[51].

evaluation for delayed ventricular repolarization by human pharmaceuticals. The changes directed by these recommendations and those that preceded[55] it were highly effective in pre-screening compounds with TdP liability as zero new drugs have been withdrawn from the world market since 2004[54]. The changes directed by these recommendations and those that preceded[55] it were highly effective in pre-screening compounds with TdP liability as zero new drugs have been withdrawn from the world market since 2004[54]. However, this approach is criticized to be overly conservative due to its single-channel-centric screening approach, in which drugs are primarily screened for a potential to block I_{Kr} (a potassium channel) in a heterologous expression system. Indeed, I_{Kr} blockade alone is not entirely predictive of a drug's impact on ventricular repolarization as a multitude of channels are responsible for this process[56]. The consequences of this approach are increased cost, slower development, and often result in attrition of many promising new chemical entities[54]. As such, regulators worldwide are working to reform the ICH S7B recommendations through the development of the Comprehensive *In-vitro* Proarrhythmia Assay (CIPA). Although a multicomponent pipeline combining both *in-vitro* and *in-silico* evaluation, it hinges on the successful implementation of hiPSC-CM for evaluation of the pro-arrhythmic risk of new compounds. Standardization of hiPSC-CM production and methodology for high-throughput evaluation is critical to the successful implementation of CIPA.

Industry-led efforts account for the majority of hiPSC-CM production and multiple commercial entities now provide standardized, "high quality" hiPSC-CMs for purchase. However, functional assays to evaluate electrophysiological and contractile properties are often not amenable for use with hiPSC-CM. For example, contractile measurements have been limited due to the lack of cellular shortening of hiPSC-CM. To address this, investigators have developed intricate methodologies including: atomic force microscopy, micropost arrays, and substrate based maturation techniques to enable cellular shortening[57-59]. While useful for single cell studies[39, 59], these experiments are low-throughput and technically challenging. Difficulties in adapting functional measurements of hiPSC-CM to commonly used techniques has led to parallel efforts to develop high-throughput and more specialized tools for evaluation of contractile and electrophysiological properties of the hiPSC-CM[60, 61]. The success of high-throughput devices for assessing hiPSC-CM is evident by the shift from pharmacological responses of only 60 compounds in hPSC-CM before 2013[62], to single studies characterizing over 100+ compounds[63, 64]. The arrhythmogenic risk of 60 compounds with variable well-characterized TdP risk using hiPSC-CM showed a sensitivity of 81%, a specificity of 87%, and accuracy of 83%, further demonstrating the utility of this platform[65]. Improvements in devices allowing for high-throughput evaluation of electrophysiological and contractile properties of hiPSC-CM has been critical to this progress[66, 67]. The exponential rates of development in industry have allowed for the availability of high quality hiPSC-CM and new methodologies for functional analyses.

While industry-led efforts have predominantly focused on use of hiPSC-CM for drug development and toxicity evaluation, others have sought to use these cells to model cardiac disease and regenerate injured myocardium. Although methods used by industry for generation of high quality hiPSC-CM are not publicly available, commercial hiPSC-CM at ~ $500 per million cells are cost prohibitive for academic investigators. Moreover, commercially available hiPSC-CM cannot be gene-edited for production of differentiated cells (e.g. for disease modeling with patient derived hiPSC). Furthermore, there is limited functional (electrophysiological, contractility, and calcium handling properties) and gene expression data for commercially available cells. To overcome these limitations, academic labs are increasingly generating their own hiPSC-CM for modeling disease including cardiomyopathies, inherited arrhythmias, and cardio-metabolic diseases[17]. Although several cardiac disease phenotypes have been successfully modeled, many aspects of disease cannot be modeled because of the immaturity of current hiPSC-CM[68]. For example, compared to human ventricular myocardium the electrophysiological phenotype of hiPSC-CM is relatively immature, as evidenced by a high expression of a pacemaker current (I_f) and low expression of a potassium current (I_{K1}) important during cardiac repolarization[69]. Thus, as the degree of repolarization reserve (contribution of multiple ion channels to repolarization) does not match that of the adult myocardium, drugs which prolong ventricular repolarization (e.g. through I_{K1}) are not accurately detected[70, 71]. In addition, diseases resulting and/or relying on I_{k1} are currently difficult to model using hiPSC-CM without injection of synthetic I_{K1}[72] or adenoviral overexpression[73] of the gene responsible for $I_{K1,}$ *KCNJ2*.

Another area of intense focus is the development of hPSC-CM for repairing the injured myocardium. Studies introducing hPSC-CM into rodent[74] and porcine models[75] of myocardial infarction showed significant improvements in cardiac function with reductions in detrimental myocardial remodeling. Similar studies performed in non-human primates following myocardial infarction showed comparable improvements in cardiac function with substantial re-p of the infarcted heart[76, 77]. However, primate models have shown significant development of ventricular arrhythmias which have been attributed to the relative immaturity of the hPSC-CM[78].

Overall, hiPSC-CM technology is rapidly growing and increasingly adopted by academia and industry alike. Its application for evaluation of pharmaceutical agents for arrhythmia risk is a clear driving force for this technology with enthusiasm from both regulatory agencies and within the pharmaceutical industry itself. Advances for disease modeling and repair of the injured heart have been met with comparable success. Nevertheless, deficiencies in hiPSC-CM have been acknowledged in all primary applications with their relative immature structural and functional properties remaining a key barrier to further advancement. An understanding of the excitation-contraction coupling properties of these cells (described above as: lack of repolarization reserve, arrhythmias post engraftment of hPSC into the injured heart, and deficiencies in recapitulating disease phenotypes) is central to addressing these deficiencies.

1.6 Cardiac Excitation-Contraction Coupling

The efficient and timely delivery of oxygen and other nutrients to tissues in the body is a primary function of the cardiovascular system. A specialized conduction system extending through the heart enables the timely initiation and spread of electrical activity that coordinates contraction and underlying pumping function of the heart. Of the various cells types within the heart, the ventricular CM is the predominant cell type responsible for force generation in the heart. At the level of the ventricular CM, the precise coordination of excitation-contraction coupling (ECC) is imperative for efficient cardiac function and deficiencies in ECC are often implicated in cardiac disease[79]. ECC can be divided into three processes 1) CM electrophysiology, 2) CM calcium handling, and 3) Activation of the contractile apparatus, which are described in detail below.

1) CM electrophysiology: The action potential (AP) of the ventricular CM is generated by coordinated activation and inactivation of membrane ion channels and transporters (**Figure 6**). The AP is subdivided into 4 phases. Ventricular CM are maintained in a resting state (phase 4) at a membrane potential of ~ -90 mV as a result of the relative distribution of ions inside versus outside of the cell in addition to the conductance of channels which allows ions to permeate the cell membrane. In contrast to ventricular CM, pacemaker cells have spontaneous activity. The spontaneous activity of pacemaker cells is largely driven by I_f, an inward current activated by membrane hyperpolarization. Spread of electrical activity from the specialized conduction system

opens voltage-gated sodium channels that depolarize the membrane (phase 0). The positive membrane potential opens transient outward potassium (I_{to}) channels which initiates early repolarization, contributing to the notch (phase 1) in the AP waveform. Simultaneous opening of voltage-gated L-type calcium channels (LTCC) counteracts the repolarization and maintain the plateau of the AP (phase 2). Repolarization of the cell rapidly ensues with closure of the LTCC and opening of the outward potassium channels (mainly those responsible for I_{Kr} and I_{Ks}, phase 3). The availability of multiple repolarizing potassium channels is critical to repolarization reserve. Potassium channels that remain open at the resting membrane potential of -90 mV (predominantly I_{K1}), stabilize the resting membrane potential until the subsequent cycle of activation.

2) CM calcium handling: Calcium serves as the intracellular 2nd messenger that links cardiac excitation (AP) to CM contraction. Hence, the kinetics of calcium rise and fall govern the rate of CM contraction and relaxation. Calcium entry is initiated by opening of LTCCs during the AP (**Figure 7A**). Subsequently, this relatively small rise in calcium triggers the opening of Ryanodine channels (RyR2) calcium release channel located in the sarcoplasmic reticulum (SR), which amplifies the calcium signal provided by LTCC. This process, known as calcium induced calcium release (CICR), is highly dependent on the close proximity of the LTCC to the RyR2 on the SR as well as the overall development of the SR. Key to the juxtaposition of LTCC and RyR2 in adult ventricular CM are t-tubules, which are cell membrane invaginations that bring membrane proteins such as LTCC in close proximity to its intracellular signaling target, the RyR2s. The rise in cytosolic calcium is required for activation of the contractile unit (**Figure 7B**). Following contraction, calcium removal from the cytoplasm enables rapid relaxation of the cell. This process is accomplished through two major pathways including: sarcoplasmic reticulum calcium transport

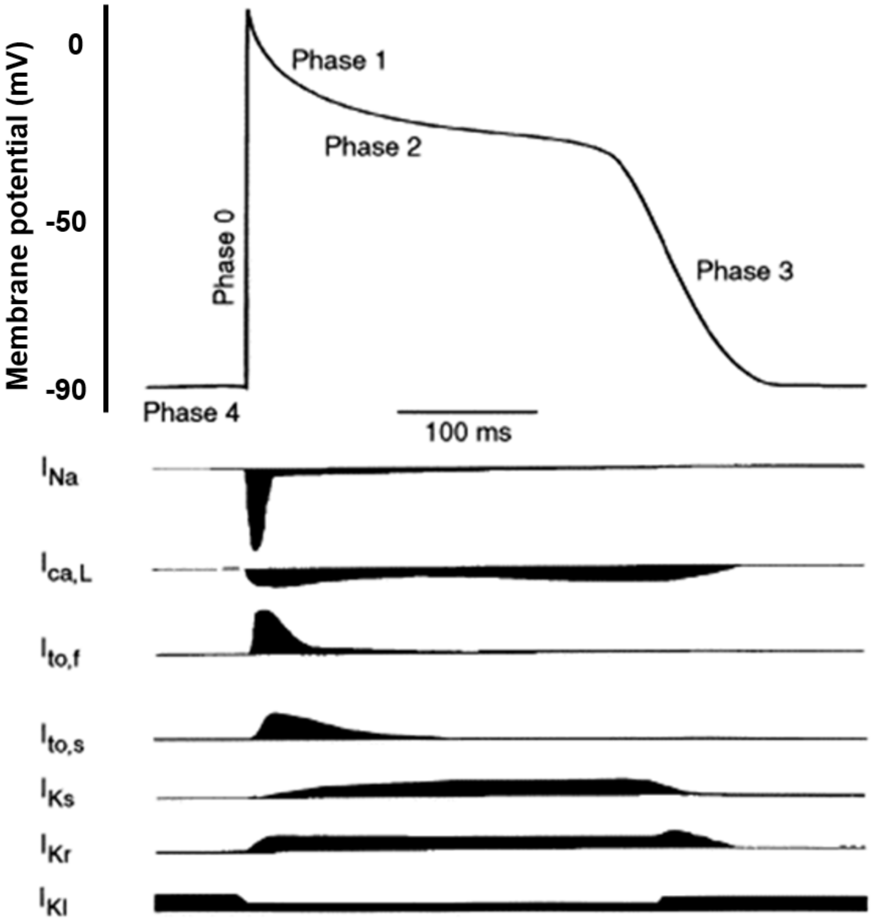

Figure 6: Human ventricular action potential and associated ion channels. The action potential trace illustrates the 4 phases with respective currents for each phase. Phase 4 is mainly driven by the potassium current I_{k1} which maintains the resting membrane potential. Upon spread of electrical activity from neighboring cells, the rapidly activating sodium current depolarizes the cell towards 0 mV in phase 0. Transiently activing outward potassium currents, I_{to}, generates the initial notch in phase 1. Phase 2 is a balance between L-type calcium current $I_{Ca,L}$ and polarizing potassium currents I_{Kr} and I_{ks}. As L-type calcium channels inactivate, the repolarizing currents accelerate to reach resting membrane conditions during phase 3. Adapted from [12].

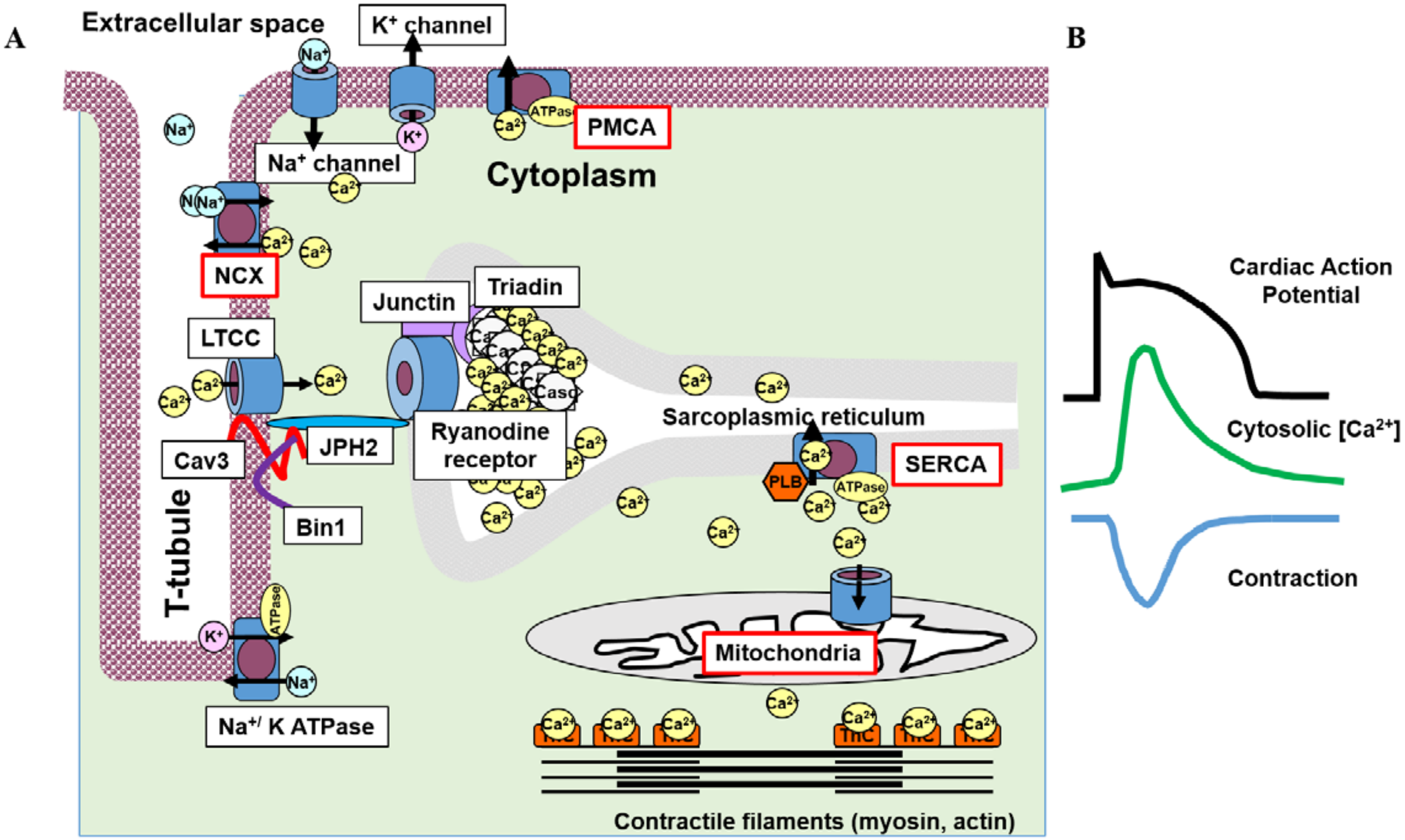

Figure 7: Excitation-Contraction Coupling. A) Schematic of the ventricular cardiomyocyte detailing pathways for calcium rise and fall. The depolarization of the membrane activates the L-type calcium channel (LTCC) allowing for entry of calcium in close proximity to the Ryanodine receptor (RyR2) on the sarcoplasmic reticulum (SR). Note presence of junctophilin 2 (JPH2), bridging integrator-1 (Bin1), and caveolin 3 (Cav3) at the interface of the LTCC and the SR. These factors are critical for invagination of the plasma membrane such that the LTCC and the SR are in close proximity allowing for efficient calcium induced calcium release (CICR). Calcium removal pathways include sarcoplasmic reticulum calcium transport ATPase (SERCA), sodium/calcium exchanger (NCX), the plasmalemmal calcium ATPase (PMCA), and the mitochondria. **B)** Temporal relationship between cardiac action potential, cytoplasmic calcium changes, and cardiomyocyte contraction and relaxation. Figure adapted from[80].

ATPase (SERCA) and sodium/calcium exchanger (NCX). In addition, calcium can be removed via “slow” pathways including both the plasmalemmal calcium ATPase (PMCA) and mitochondrial pathways.

Live cell calcium imaging allows for both whole cell and temporal-spatial evaluation of calcium kinetics in the cell[81]. Using calcium sensitive fluorescent indicators, the relative contribution of each extrusion pathway can be calculated. This is achieved by experimentally evaluating the kinetics of calcium decay by selective inhibition of individual calcium removal pathways **(Figure 8A).** Total calcium removal is estimated as the decay rate constant of a field stimulated calcium transient (τ_{twitch}). Caffeine stimulated calcium transient allows for the estimation of SR calcium stores while the decay rate constant (τ_{Caff}) permits calculation of combined NCX and “slow” extrusion pathways. Stimulation with caffeine in the absence of sodium and calcium in the extracellular solution eliminates the contribution of NCX and SERCA allowing for measurement of “slow” pathways as per the decay rate constant ($\tau_{\text{Caff0Ca0Na}}$). Using the equations provided in **Figure 8B**, the contribution of each calcium removal pathway can be calculated. Further normalization of individual rate constants to total flux rate (K_{twitch}) provides the relative contribution of each calcium flux pathway to total calcium extrusion. **Figure 8C** illustrates SR and NCX predominance of calcium removal in both rabbit and mouse, however also highlighting the differences between species. Furthermore, pharmacological inhibition of the SR using ryanodine (removes RyR2 contribution) and thapsigargin (SERCA inhibitor) allows for the experimental assessment of the SR contribution to the whole cell calcium transient, thus dissecting the contribution of LTCC versus SR for calcium rise.

3) Activation of the contractile apparatus: Muscle fibers contain many elongated, cylindrical cells containing nuclei, mitochondria, and sarcomeres. Critical to force generation is

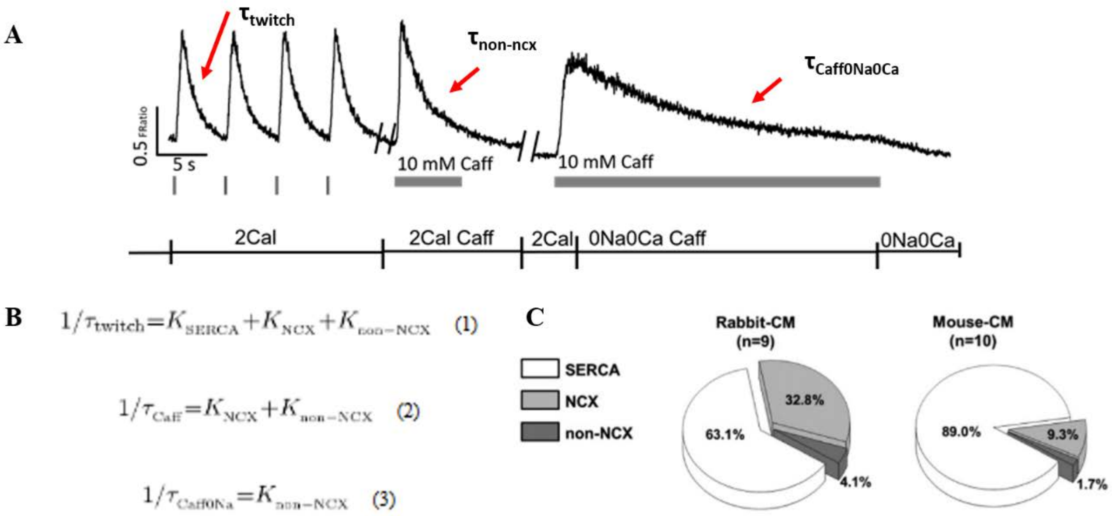

$$1/\tau_{twitch} = K_{SERCA} + K_{NCX} + K_{non-NCX} \quad (1)$$

$$1/\tau_{Caff} = K_{NCX} + K_{non-NCX} \quad (2)$$

$$1/\tau_{Caff0Na} = K_{non-NCX} \quad (3)$$

Figure 8: Evaluation of Calcium Extrusion. **A)** Example calcium transient for assessment of τ_{twitch}, $\tau_{non-nxc}$, and $\tau_{Caff0Ca0Na}$. **B)** Equations for determining relative contributions of respective calcium efflux pathways. **C)** Species differences in calcium removal between rabbit and mouse ventricular cardiomyocyte (adapted from[82]).

the activity and structural alignment of sarcomeres. Sarcomeres are composed of thick filaments and thin filaments. Thick filaments (myosin) interact with a binding site on actin which allow for cross bridge formation and subsequent sarcomere shortening. The thin filaments are composed of actin, tropomyosin, and the troponin complex. The troponin complex contains three subunits: troponin-T, troponin-I, and troponin-C. Tropomyosin prevents activation of the myofilament by inhibiting the interaction between myosin and actin. The regulatory troponin complex is tethered to the tropomyosin via troponin-T. The elevation in cytosolic calcium upon CICR allows for binding of calcium to troponin-C, causing a conformational shift in the troponin-I subunit. This enables an interaction between the myosin head and actin allowing for force generation.

In summary, ECC is a fundamental property required for converting electrical stimulation into force generation. The positioning of the LTCC in the t-tubules to the RyR2 on the SR is critical for efficient CICR and thus demonstrates the necessity of this structural arrangement. Furthermore, defects in ECC result in poor contractility and arrhythmogenesis[83].

1.7 Structural and Functional Characteristics of HiPSC-CM

Despite successful use of hiPSC-CM, current differentiation protocols produce cells with an immature phenotype. Structural and functional characteristics of these cells suggest that they are comparable to the early fetal-CM[84]. **Table 1** provides an overview of major structural and functional differences between adult ventricular CM and hiPSC-CM. Overall, hiPSC-CM demonstrate key characteristics of a human cardiomyocyte: they have contractile activity, respond to electrical stimuli, produce an action potential, and express important sarcomere and ECC proteins. Particularly, hiPSC-CM have ion currents for depolarization (I_{Na}, I_{CaL}), as well as those for repolarization (I_{kr}, I_{to}, and minimally I_{ks} and I_{k1}). They also express many of the components of the ECC system (LTCC and RyR2) as well as systems for cellular relaxation (NCX, SERCA2a, and PMCA). However, the presence of these alone have not been sufficient for replacing the human ventricular CM as evidenced by failures in disease modeling, arrhythmias after transplantation, and inaccurate drug response. Inefficient CICR, slow calcium handling and electrical immaturity of the hiPSC-CM are major limitations of hiPSC-CM that could be contributory.

CICR is the linking feature between electrophysiological stimulation and force generation. The speed of calcium release during this process relies on efficient and rapid opening of intracellular calcium stores. Although hiPSC-CM demonstrate calcium transients, the rise and fall of calcium is considerably slower than that of the adult human-like CM[82]. As the rise time is linked to the rate of calcium influx via the LTCC and its ability to induce CICR, slow rise times can suggest **1**. diminished LTCC function, **2**. inefficient CICR, and/or **3**. immature SR. HiPSC-CM demonstrate comparable expression of the LTCC to that of the adult human ventricular CM[85] and patch clamp techniques show robust LTCC current, similar to that of the adult mouse CM[82]. In addition, pharmacological blockade of the LTCC using nifedifine and removal of extracellular calcium completely prevent SR calcium release suggesting a reliance of calcium from the LTCC[86]. Conversely, hiPSC-CM show diffuse RyR2 immunostaining with mostly puncate perinuclear localization[87]. In addition, expression of RyR2 and other key SR regulatory proteins calsequestrin (Casq2) and triadin (Trdn) are considerably lower in the hiPSC-CM compared to the adult human heart[85, 87]. Despite reduced expression of RyR2, caffeine produced calcium transients of similar amplitude to that of both rabbit and mouse adult CM demonstrating the presence of relatively developed SR[82]. Despite comparable LTCC currents and fairly developed SR, the kinetics of intracellular calcium rise remain considerably slower in hiPSC-CM at ~500 ms compared to less

		Adult-CM	**hPSC-CM**
Structure	Structure	Rod-shaped	Round or polygonal
	Alignment	Longitudinally aligned	Chaotically organised
	Nucleation	~ 30% cells bi- or poly-nuclear	Very limited bi-nucleation
	Sarcomere organisation	Highly organised	Disorganised
	Aspect ratio	5–9.5:1	2–3:1
	Banding	Z-discs, I-, H-, A- and M-bands	Mainly Z-discs and I-bands
	Sarcomere length	2.2 µm	1.6 µm
SR	Sarcoplasmic reticulum	Well developed	Mixed response: caffeine, Thapsigargin & ryanodine
	SR proteins	e.g. CSQ, PLN, RYR2, SERCA/ATP2A2	Expression lower than adult
	T-Tubules	Yes	No
Expr.	Gene expression	MYH7 (β-MHC) > MYH6 (αMHC)	MYH6 (αMHC) > MYH7 (βMHC)
		TNNI3 (cTnI) > TNNI1 (foetal ssTnI)	TNNI1 (foetal ssTnI) > TNNI3 (cTnI)
		MYL2 (MLC2v) > MYL7 (MLC2a)	MYL2:MYL7 ratio not determined
		Titin isoform N2B predominates	Titin isoform N2BA predominates
		ADRA1A (α-adrenoceptor) expressed	ADRA1A (α-adrenoceptor) not expressed
Energy & force	Metabolism	Mainly fatty acids	Glucose and lactate but can use fatty acids
	Energy production	Mainly oxidative phosphorylation	Mainly oxidative phosphorylation
	Mitochondria	Throughout cell; occupies 20–40% of cell volume	Near nuclei; numbers increase during differentiation
	Beating	Quiescent	Many cells spontaneous
	Force	40 to 80 mN/mm2 (muscle strips)	0.08–4 mN/mm2 (3D constructs)
		~ µN range (single cells)	~ 200 nN (single cells)
Conductn	Capacitance	150 pF	20–50 pF
	Resting mem potential	− 80 to − 90 mV	− 20 to − 60 mV
	Upstroke velocity	150–350 V/s	10–50 V/s
	Conduction velocity	60 cm/s	10–20 cm/s
	Location of gap junctions	Intercalated discs	Circumference of cells
Ion channel density (pA/pF)	INa	− 196	− 100 to − 244
	ICaL	− 4.3 to − 10.2	− 2.2 to − 10
	Ito	2.3 to 10.6	2.5 to 13.7
	IKs	0.18 to 0.58	Most publications 0.3 to 0.7
	IKr	0.5	0.4 to 0.8
	IK1	− 12	0 to − 3.4
	INCX	2.5 to 3	3.6 to 7.9 (inward mode)
	APD90	260 ms	300–700 ms
Ca2 + kinetics	T-rise	2.5 ms	3.5-10 ms

Table 1: Comparison of structural and functional properties between adult CM and hPSC-CM. Table provides evidence for lack of structural and functional maturation of hPSC-CM. Table adapted from [88].

than ~200 ms in rabbit adult CM[82].

Using confocal microscopy, transverse line scan at the mid-plane of electrically paced CM is often used for assessing the spatial-temporal features of calcium releases. Using this method, the time course of calcium fluorescence across the width of the cell showed an asynchronous calcium release in hPSC-CM visualized as a U-shaped waveform[89]. Specifically, when comparing the calcium kinetics of the cell periphery to the cell center, hPSC-CM demonstrate a delayed rate of calcium release at the center versus periphery whereas adult mouse-CM show uniform rates of calcium release throughout the width of the cell[89, 90]. Consistent with this finding is the poor juxtaposition of LTCC and RyR2 in hPSC-CM[85, 91]. Efficient CICR is dependent on sufficient expression and organization of RyR2 (clustering and appropriate localization to the z-line) as well as juxtaposition of the LTCC to the RyR2, all of which are poorly developed in the hiPSC-CM.

Calcium removal was also found to be substantially slower in hiPSC-CM, estimated at rates half of rabbit adult CM[82]. Likewise, SERCA2a, the predominant cardiac isoform of SERCA, shows significantly lower expression in hiPSC-CM compared to the adult human heart[85]. The other dominant calcium extrusion pathway NCX[85], shows similar expression to that of the adult human heart, however absolute values of calcium removal remain considerably less than the adult rabbit CM. Despite an overall reduction in the calcium extrusion rates, the relative contribution of SERCA and the NCX remain similar to that of the adult rabbit CM[82].

Electrically, hiPSC-CM are considered immature as they demonstrate automaticity and adult ventricular CM do not. This has been attributed to the high expression of the pacemaker current, I_f, which is normally predominantly expressed in the cells of the cardiac conduction system, such as cells in the sinoatrial node. In addition, most studies show that hiPSC-CM have very low to absent expression of I_{K1}, which is the potassium current that stabilizes the resting membrane potential (phase 4). HiPSC-CM also have minimal I_{Ks}, which when combined with the deficient I_{K1} leave only one major repolarization source, I_{Kr}. Lastly, hiPSC-CM AP exhibit slow upstroke velocity, which could be responsible for the slow conduction velocity in hiPSC-CM syncytia compared to the adult human ventricular myocardium[88].

Inefficient CICR, slow calcium kinetics, and electrical immaturity are all properties which could be explained by the lack of adult-like myocyte structure in the hiPSC-CM. Specifically, inadequate localization of RyR2 at the z-line and/or lack of t-tubules are major structural determinants of the functional deficiencies observed in the hiPSC-CM.

1.8 T- tubules and hiPSC-CM

T-tubules are membrane invaginations found at regular intervals along the Z-line of the adult cardiac sarcomere. Although the majority of the t-tubules are transverse projections towards the cell interior, the organization of t-tubules is complexly branched, with ~40% found not to be transverse in rodents (although less branched in human CM)[92, 93]. Rather, as t-tubules project towards the cell center at the Z-line, they penetrate the cell for a short distance and then converge with neighboring transverse t-tubules in a diagonal or longitudinal fashion[94]. This allows for maximal intra-cellular coverage of the extracellular interface. This structural arrangement facilitates transmission of membrane potential changes towards the interior of the cell such that the excitation is synchronous throughout the cell. Specifically, the high concentration of LTCC on the t-tubules closely juxtaposed to

RyR2 at the dyad (area of junctional SR and t-tubule) enables efficient CICR.

The functional significance of t-tubules is well evidenced in findings from de-tubulated adult CM. De-tubulation of adult rat ventricular CM results in a significant reduction in cellular capacitance with an overall reduction in calcium transient amplitude[95]. Transverse line scan across the width of the cell showed an asynchronous calcium release in detubulated cells versus controls visualized as a U-shaped waveform- similar to hPSC-CM[96]. When comparing the calcium kinetics of the cell periphery to the cell center, detubulated cells demonstrated a delayed rate of calcium release at the center versus periphery whereas control cells showed uniform rates of calcium release throughout the width of the cell[96]. In addition, a correlative comparison of loss of membrane currents after loss of t-tubules shows a reduction in I_{K1} (in addition to I_{NCX} and I_{CaL}) highlighting the importance of the t-tubule in the subcellular distribution of key membrane currents[97-100].

HiPSC-CM demonstrate similar functional deficits as de-tubulated adult rat CM. hiPSC-CM exhibit a non-uniform calcium release across the width of the cell with faster kinetics at the periphery and slow release in the center, similar to the U-shaped waveform observed in de-tubulated CM[89]. Aside from the functional similarities in inefficient calcium release between de-tubulated adult CM and hiPSC-CM, imaging studies have verified the absence of t-tubules in hiPSC-CM[89, 91]. Furthermore, factors associated with the genesis of t-tubules (bridging-integrator 1 and caveolin-3) were also absent[89]. Lastly, hiPSC-CM showed a lack of co-localization of LTCC and RyR2, where LTCC were diffusely scattered throughout the cell and RyR2 was mostly perinuclear, consistent with the lack of dyad formation. Also consistent with the absence of t-tubules is the minimal I_{K1}, which is likely contributing to the higher resting membrane potential observed in hiPSC-CM and potentially contributing to automaticity[101]. Current techniques for hiPSC-CM differentiation have failed to promote t-tubule development and result in inefficient CICR. Thus, t-tubule-genesis in hiPSC-CM remains a major limitation, which if solved will be a major advancement in the maturation of hiPSC-CM with improved ECC and reduced automaticity[89, 102, 103]. A caveat to the limitations of hiPSC-CM presented herein is that the discussion excludes developments from engineered heart tissues (EHT), and focuses on single cell or monolayer use of hiPSC-CM. Briefly, EHT are strips of force-generated heart tissue with aligned sarcomeres that show similar physiological and pharmacological response as human heart tissue[104]. The development of EHT is very promising as recent studies has shown human-CM like t-tubule development and associated functional properties[105, 106]. However, EHTs are not yet amenable for widespread use due the large number of cells required and technical challenges associated with their production.

1.9 Dilated Cardiomyopathy

Heart failure is a complex and debilitating clinical syndrome with a multifactorial etiology estimated to affect over 8 million persons in the United States alone[1]. Dilated cardiomyopathy (DCM), a leading cause of heart failure worldwide, manifests with structural thinning and expansion of cardiac chambers with a progressive decline in cardiac function. Clinically, DCM is defined by impaired cardiac function (low ejection fraction <45%) and left ventricular enlargement[107]. Importantly, DCM is often associated with an increased risk of severe arrhythmia, which may be disproportionate to the degree of left ventricular dysfunction and highlights the risk for sudden cardiac death[108]. Clinical management of DCM is focused on preserving cardiac function and size, monitoring and preventing arrhythmia, and reducing symptoms secondary to heart failure. Due to the lack of curative therapies available, the need to preserve cardiac structure and function is critical to delay heart transplant, thus demonstrating the need for early diagnosis and aggressive clinical management.

DCM can be caused by genetic or non-genetic factors. Examples for the latter are ischemic heart disease, hypertension, valvular disease, inflammatory causes, and environmental toxins. Non-genetic forms of cardiomyopathy can also be influenced by an individual's genetic background such that heterogeneous pathogeneses are likely contributory to disease progression[109, 110]. DCM is clinically subdivided into non-ischemic and ischemic, where ischemic DCM includes those with prior history of myocardial infarction. Non-ischemic DCM is comprised of all other causes of DCM including toxins, pharmacological, metabolic, endocrine, inflammatory, and predominantly unknown etiology or idiopathic[108]. Idiopathic DCM is a diagnosis of exclusion such that all determinable causes of cardiomyopathy should be assessed prior to diagnosis, making for a costly and difficult clinical endeavor for afflicted patients. Essentially, a diagnosis of idiopathic DCM is meaningless and indicates the current inability to identify the underlying cause.

Substantial family history was identified in numerous phenotyping studies of patients diagnosed with idiopathic DCM[111, 112]. Familial dilated cardiomyopathy (FDC) is defined as DCM meeting the criteria for idiopathic DCM in at least two closely related family members of the proband, providing rationale for a genetic basis of disease[112]. Unfortunately, despite diagnosis of FDC, the genetic cause can only be identified in a subset of these patients[108]. Although a general consensus has emerged that genetic variation is the underlying cause of FDC, many still question the significance of genetics in idiopathic DCM patients lacking family history. However, as resequencing studies have identified potentially disease-causing mutations (not found in healthy controls) in many patients previously diagnosed with idiopathic DCM, it has been suggested that a significant proportion of what has previously been characterized as idiopathic may in fact have a rare-variant genetic basis[113]. Indeed, based on the increase of similar findings, a recent DCM precision medicine study has been funded to assess the hypothesis that all cases of idiopathic DCM have a genetic basis[114].

Substantial advances in the genetics of DCM have been made through linkage analysis and targeted candidate gene sequencing such that the clinically utilized gene panels for dilated cardiomyopathy assess exonic regions of up to ~111 genes[108]. The rationale for genetic testing in DCM is to identify the disease -causing mutation in at-risk family members who at time of testing do not show evidence of disease. They can then undergo specialized clinical surveillance to delay progression of disease as well as inform reproductive decision making. However, enthusiasm for genetic testing remains low such that it is not widely implemented as the testing sensitivity is not ideal and the issue of rare variants being established as disease causing remains problematic. As the genetic contribution to DCM is very diverse with new variants being identified at a high rate, the combined advancement in gene editing and progress in modeling DCM with hiPSC-CM [115-123] provides a useful framework to assess pathogenicity and identify mechanisms of DCM in a cell specific and temporal fashion.

OBJECTIVES

HiPSC-CM, although yet another tool, have great potential and are being increasingly used in academia and industry. With the potential to revolutionize biomedical research by providing an unlimited source of human CM for studying cardiac disease and cardiac toxicity, it has also generated hope for repairing the injured heart. Due to the projected value of this tool, research and development of hiPSC-CM has skyrocketed. However, the relative immaturity of hiPSC-CM currently limits their implementation for modeling disease, screening drug toxicity, and in regenerating the heart. Furthermore, as DCM remains a major clinical problem, the development of validated human cellular models of DCM are necessary for understanding mechanisms of disease pathogenesis. Hence, the objective of my thesis was two-fold: **1.** To assess the utility of hiPSC-CM for modeling DCM, and **2.** Improve the maturation status of hiPSC-CM.

In **Chapter 2**, I study a DCM causing gene variant in *LMNA* using hiPSC-CM combined with CRISPR/Cas9 gene editing. Using both single cell and monolayer approaches, I provide evidence for molecular and contractile deficits, which are rescued after gene editing. Furthermore, I demonstrate the utility of a high-throughput method for evaluating contractile parameters of hiPSC-CM in monolayer. Through these analyses, I recognized the limitations posed by hiPSC-CM immaturities and sought to advance their development.

Central to making advances in maturation of hiPSC-CM is a thorough understanding of the calcium handling and electrophysiological properties that govern adult-like excitation-contraction coupling. In **Chapter 3**, I identify an additive effect of T3 + Dexamethasone in combination with a substrate of physiological stiffness (Matrigel mattress) for enhancing both structural and functional maturation of hiPSC-CM[124]. Through induction of early t-tubule development and SR maturation, I was able to greatly improve the excitation-contraction coupling efficiency of hiPSC-CM while providing insight on pathways required for t-tubule development, which remains a critical unmet need. In addition, I then utilize a high-throughput system to evaluate the impact of T3 + Dexamethasone maturation on hiPSC-CM in monolayer.

In sum, this work resulted in the generation of hiPSC-CMs with more adult-like excitation-contraction coupling while providing insight on mechanisms responsible for this maturation. In addition, this work demonstrates the utility of high-throughput functional assessment of academically generated hiPSC-CM for disease modeling. These findings will facilitate the use of hiPSC-CM for disease modeling and help the field's efforts to generate more mature hiPSC-CM.

CHAPTER 2

INVESTIGATION OF PATIENT-SPECIFIC HUMAN INDUCED PLURIPOTENT STEM CELL DERIVED CARDIOMYOCYTES FOR MODELING LAMIN A/C CARDIOMYOPATHY

ABSTRACT

Rationale: Dilated cardiomyopathy (DCM) is a leading cause of heart failure with significant genetic etiology. It is estimated that up to ~10% of DCM cases result from mutations in lamin A/C (*LMNA*). Despite the autosomal-dominant inheritance of LMNA DCM, gene-targeted mouse models of LMNA DCM show minimal human-like disease progression unless generated in a homozygous fashion. The combination of poor *LMNA* cross-species sequence conservation and limited disease manifestation in mice necessitates a more human-like cellular model. The combined advancements in gene editing and development of human induced pluripotent stem cell derived cardiomyocytes (hiPSC-CM) provides a unique opportunity to assess mutation pathogenicity and study mechanisms of LMNA DCM in a cell-specific fashion.

Objective: Here, I test the hypothesis that hiPSC cardiomyocytes (CM) derived from a laminopathy patient will exhibit a cellular DCM phenotype when matured on a substrate of physiological stiffness.

Methods and Results: Patients carrying a *LMNA* gene variants and diagnosed with DCM were recruited for clinical testing. Peripheral blood mononuclear cells were isolated and reprogrammed

into hiPSCs. CMs were generated using a chemical differentiation method and subjected to molecular and functional assessment. For single cell assessment of contractility, day 30 cells were re-plated on flexible Matrigel substrate and allowed to mature for five additional days prior to edge detection assessment of Fura2-AM loaded cells using the IonOptix instrument. Single cell experiments were complemented by impedance (contractility correlate) measurements of hiPSC-CM monolayers in a 96-well format. We identified a multigenerational pedigree in which individuals afflicted with DCM co-segregated with a pathogenic *LMNA* mutation (c.1526dupC). Patient specific hiPSC-CM showed a reduction in both lamin mRNA and protein. Single CM were matured using substrate of physiological stiffness (Matrigel mattress exhibited alterations in nuclear shape and defective excitation-contraction coupling. CRISPR/Cas9 mediated gene correction restored lamin A/C expression and rescued contractile deficits observed in patient derived hiPSC-CM in monolayer.

Conclusion: Our results are the first to provide evidence for contractile dysfunction in a hiPSC-CM model of cardiac laminopathy. Overall, these findings provide a framework for assessing patient specific mutations. As such, use of this tool will enhance assessment of *LMNA* mutations of unknown pathogenicity for improved clinical management of mutation carriers. This work highlights the utility of impedance-based assessment of contractility as a robust measurement that can be applied to high-throughput evaluation of therapeutic interventions in this disease model.

INTRODUCTION

Heart failure (HF) is a progressive and debilitating syndrome that is a leading contributor to death worldwide[1]. Dilated cardiomyopathy (DCM), a primary cause of HF, has significant genetic etiology. Mutations in lamin A/C (*LMNA*) are common contributors to genetic cases of DCM[125]. Although mutations in *LMNA* result in non-cardiac diseases including early aging (progeria), neuropathy, and muscular dystrophy, many patients with mutations in *LMNA* show predominant cardiac involvement, indicating a critical function of lamin A/C in cardiomyocytes (CM)[126].

Patients with *LMNA* mutations show variable disease presentation including the development of atrioventricular block, supraventricular and ventricular arrhythmia, and highly penetrant DCM[127]. Typical progression of the disease often starts with conduction system disease and supraventricular arrhythmias followed by cardiac dilation leading to HF, however features can present in other orders and combinations[44, 127, 128]. Sudden cardiac death due to ventricular arrhythmia can occur, often preceding cardiac structural or functional deterioration, thus highlighting the need for early diagnosis and management.

Lamin undergoes alternative splicing of a single mRNA transcript for the generation of four products termed nuclear lamins (A, C, C2, and AΔ10). In the normal CM, lamin A and C are the predominant lamins, and are critical structural components of the inner nuclear membrane. Lamins interact with chromatin and proteins of the inner nuclear membrane suggesting both a structural and gene regulatory function[129]. Specifically, lamins are implicated in regulation of DNA replication, cell-cycle regulation, chromatin organization, cellular differentiation, nuclear stability, nuclear pore positioning, gene expression and signal transduction[130]. As lamins play a diverse role in the cell, the main mechanisms by which lamin mutations cause cardiac dysfunction is not established. Current hypotheses indicate the mechanisms are multifactorial focusing on two areas: structural instability and altered gene expression[130]. As lamins form a scaffold beneath the nuclear membrane and extend into the nucleoplasm, they act to maintain the integrity of the nucleus while mediating signaling events between the cytoplasm and the nucleus[131]. Nuclear lamins are also coupled to components of the cytoskeleton, thereby connecting the nuclear lamina to the extracellular matrix. The mechanical hypothesis suggests that the disruption of the mechano-transduction pathways can render the cell susceptible to mechanical stress (e.g. during each heart beat). In addition, there is substantial crosstalk between the impaired mechano-transduction and the gene expression hypothesis. Alterations in nuclear structure resulting from dysfunctional lamins disrupts signal transduction from outside of the nucleus, but also alters chromatin organization which has been shown to directly alter gene expression[131, 132].

In addition to the highly diverse function of lamins, there is not a clear relationship between location of the mutation on the *LMNA* gene and disease phenotype[126]. Furthermore, increased genetic testing of patients with familial DCM has resulted in the detection of numerous variants of unknown significance (VUS) in *LMNA* (and other DCM-causing genes)[133]. The growing number of unique *LMNA* mutations and difficulties faced in predicting mutation pathogenicity limits the clinical utility of genetic testing, leaving many patients in a state described as genetic purgatory[134]. The lack of consensus on the causality of these mutations and undefined mechanisms of pathogenesis renders genetic test results less clinically useful as there is poor rationale for genetic counseling of family members and clinical management. Thus, developing a robust human cellular model with phenotypes specific to LMNA cardiomyopathy is a critical step for advancing investigation and therapeutic intervention of patients with uncharacterized *LMNA* variants[134].

Recent advances in hiPSC-CM technology and development of devices for high-throughput contractile assessment provide can be combined to develop a screening platform to study disease causing *LMNA* mutations. Here, we identified a multigenerational family carrying a pathogenic DCM-causing mutation in *LMNA* (c.1526dupC). Using patient derived hiPSC-CM we characterized contractile parameters in single cells and in monolayer. Patient specific hiPSC-CM demonstrated reduced lamin A/C expression, contractile deficits in single cell and monolayer, impaired calcium handling, and abnormal nuclear shape. Correction of the *LMNA* mutation with CRISPR/Cas9 gene restored *LMNA* gene expression and rescued contractile deficits observed in monolayer. Overall, my findings combine hiPSC-CM and gene editing technology to study a disease-causing *LMNA* mutation (c.1526dupC) and establish a framework for establishing pathogenicity of *LMNA* mutations.

MATERIALS AND METHODS

HiPSC Culture and Maintenance: Human induced pluripotent stem cells (hiPSC) were generated using peripheral blood mononuclear cells from consenting, *LMNA* mutation carrying patient. Healthy population control hiPSC lines have been validated and previously published[39, 124]. The peripheral blood mononuclear cells were reprogrammed to hiPSC using a non-integrating episomal based reprogramming approach as described previously in accordance with Vanderbilt Institutional Review Board (Nashville, TN) [39]. HiPSCs were subjected to a battery of analyses for verification of stemness and genomic stability including karyotyping[39]. HiPSCs were maintained on growth factor reduced Matrigel (Corning) coated plates in mTeSR1 medium[51, 52]. Plates were coated with 1:200 Matrigel diluted in DMEM/F12 for at least 1 hour at 37 °C prior to use. HiPSC were passaged every four days. Cells were washed with 1xPBS without $CaCl_2$ or $MgCl_2$ and dissociated with 0.5 mmol/L EDTA in PBS without calcium or magnesium for ~7 minutes at room temperature (RT) followed by resuspension in mTeSR1 medium with 10 µmol/L RHO kinase inhibitor Y-27632 (Calbiochem) and immediately seeded on Matrigel coated plates. Cells received fresh mTeSR1 media daily and were maintained at 37 °C at 5% CO_2.

Differentiation and Maturation of hiPSC into Cardiomyocytes: HiPSC-cardiomyocytes (hiPSC-CM) were generated using a small molecule cardiac differentiation protocol. HiPSCs were cultured until they reached ~65-85% confluence (cell line specific), at which point chemical differentiation was initiated (day 0). Differentiation medium are defined as M1 (RPMI 1640 with glucose with B27 minus insulin), M2 (RPMI 1640 with glucose with B27 minus insulin), and M3 (RPMI 1640 with glucose with B27). At day 0 the hiPSC transition from mTeSR1 medium to M1 supplemented with 6 µmol/L GSK3 inhibitor CHIR99021 (Selleck Chemicals). On day 2, the media was changed to fresh M1. On day 3, the media was changed to M1 with 5 µmol/L IWR-1 (Sigma). On days 5 to 9 the media was changed every other day with M1. Metabolic selection was started with M2 media on day 10 and cells received fresh M2 media on days 12 and 14. On day 16, cells were transitioned to 3 mL M3 media changed every other day until further use.

Immunoblotting: Day 40 hiPSC-CM were lysed in NP-40 homogenization buffer supplemented with protease (Sigma 8349) and phosphatase (Sigma P0044) inhibitor. Cells were first rinsed with 1x PBS and incubated in 1x lysis buffer on ice for 5 minutes. Using a cell scrapper, cells were mechanically dislodged and transferred into a 1.5mL Eppendorf tube for centrifugation at 4°C for 15 minutes at 16000xg. Protein was then quantified using the Bio-Rad DC protein Assay. Protein lysates was resolved on a 4-20% Tris gel (BioRad) and transferred onto PVDF for immunoblotting. Membranes were incubated with primary antibody targeting lamin A/C (1:1000 CS-4777, 1:1000 CS-2032, and 1:200 SC-6215) and GAPDH (1:10000 AM4300) overnight at 4°C on a rocker. After washing and incubation with appropriate secondary IgG-peroxidase antibody, blots were reacted with ECL Prime Chemiluminescence reagent (Amersham Bioscience) and exposed to auto-radiographic film for visualization.

Quantitative RT^2-PCR: Total RNA was isolated from hiPSC-CM using the RNeasy Isolation kit (Qiagen) and reverse transcribed using the iScript™ cDNA Synthesis kit (BioRad). Quantitative reverse transcriptase polymerase chain reaction (qRT^{2}PCR) was performed using TaqMan Fast Advanced Master Mix on the CFX96 Real-Time PCR Detection System (BioRad). Fold change in gene expression was determined using the comparative Ct method (ΔΔCt) with normalization to the reference gene 18sRNA. Validated TaqMan primer/probe sets for LMNA (Hs00153462_m1) and Eukaryotic 18s RNA (4319413E) were utilized for target amplification.

hiPSC-CM Dissociation and Plating on Matrigel Mattress: At day 30 of the chemical differentiation process, hiPSC-CM were dissociated and plated as previously described[59, 82]. Freshly differentiated hiPSC-CM were washed with 1x DPBS without calcium and magnesium and then incubated in 1 mL of TrypLE Express (Life Technologies) for 10 minutes at 37 ºC. A 10 mL serological pipet was then used to add equal volumes of M3 to neutralize TrypLE and for resuspension. Cells were centrifuged at 200 x g for 5 minutes, re-suspended in 1-3 mL of M3, and filtered through a 40 µM filter (Falcon). The filtered cells were counted and seeded on Matrigel mattress as previously described[59, 124, 135]. HiPSC-CM were seeded 10-15,000 cells on Matrigel mattress on Delta TPG Culture Dish (Fisher). See **Figure 9** for illustrative methods for seeding cells on Matrigel mattress. Cells were allowed to attach for at least 10 minutes at room temperature (RT) before adding an additional 1 mL of normal M3 media and returned to the incubator for experimental use at days 4-6. M3 media was refreshed on a daily basis until experimentation. The Matrigel mattress method generates single, elongated CM located in a glass bottom culture dish that can be used for imaging and measurement of calcium fluorescence[59]. Since not all hiPSC-CM achieve a rod shape on mattress, hiPSC-CM were selected for experimental studies using the same morphological and functional selection criteria that are widely used in studies of CM acutely-isolated from adult hearts: (1) rod-shape, (2) no contact with other cells, and (3) contractile response to field stimulation.

Measurement of Intracellular Calcium and Contractility: After acclimation on Matrigel mattress with daily M3 media changes, cells were loaded with Fura-2 AM (Molecular Probes Inc, Eugene, OR) as previously described[59, 82]. Fura-2 AM was reconstituted in DMSO at 2 mmol/L in a light-protected vessel. HiPSC-CM were incubated at a final concentration of 2 µmol/L Fura-2 AM in M3 medium for 8 minutes at RT and then washed twice with 1.2 mmol/L calcium containing Tyrode's solution with 250 µmol/L probenecid. Measurements were made with a 40x LUCPlanFLN Ph2 (WD 2.7-4 mm) objective using an Olympus microscope fitted with an IonOptix video microscopy system (Ionoptix, Milton, MA). Tyrode's solution contained in mmol/L: 2mM $CaCl_{2,}$ NaCl 134, KCl 5.4, MgCl2 1, glucose 10, and HEPES 10, with the pH adjusted to 7.4 with NaOH. The protocol used for interrogation of calcium handling is shown in **Figure 10**.

Immunocytochemistry: hiPSCs were cultured on Matrigel-coated coverslips (Warner #67-0702) and fixed with 4% paraformaldehyde (Thermo #28906) for 15 minutes at room temperature. Cells were washed three times with 1x PBS and permeabilized with .4% TritonX-100 in PBS for 1 hour, following which they were blocked for 2 hours (1% BSA, .4% TritonX-100 in 1xPBS). Cells were incubated with primary antibodies including cardiac troponin-T (Abcam #45932 1:200) and LMNA (SC-6215 1:200) overnight at 4°C. Cells were washed 3x with wash solution and incubated with secondary antibody for 4 hours. Finally, after washing cells with 1x PBS, the cells were counterstained with DAPI and mounted on a cover slide for imaging on the Zeiss LSM-710 confocal microscope. Using ImageJ, immunostaining images were adjusted equally and all images were cropped and scaled equally.

hiPSC-CM Dissociation and Monolayer Generation: CardioExycte96 (Nanion) sensor plates

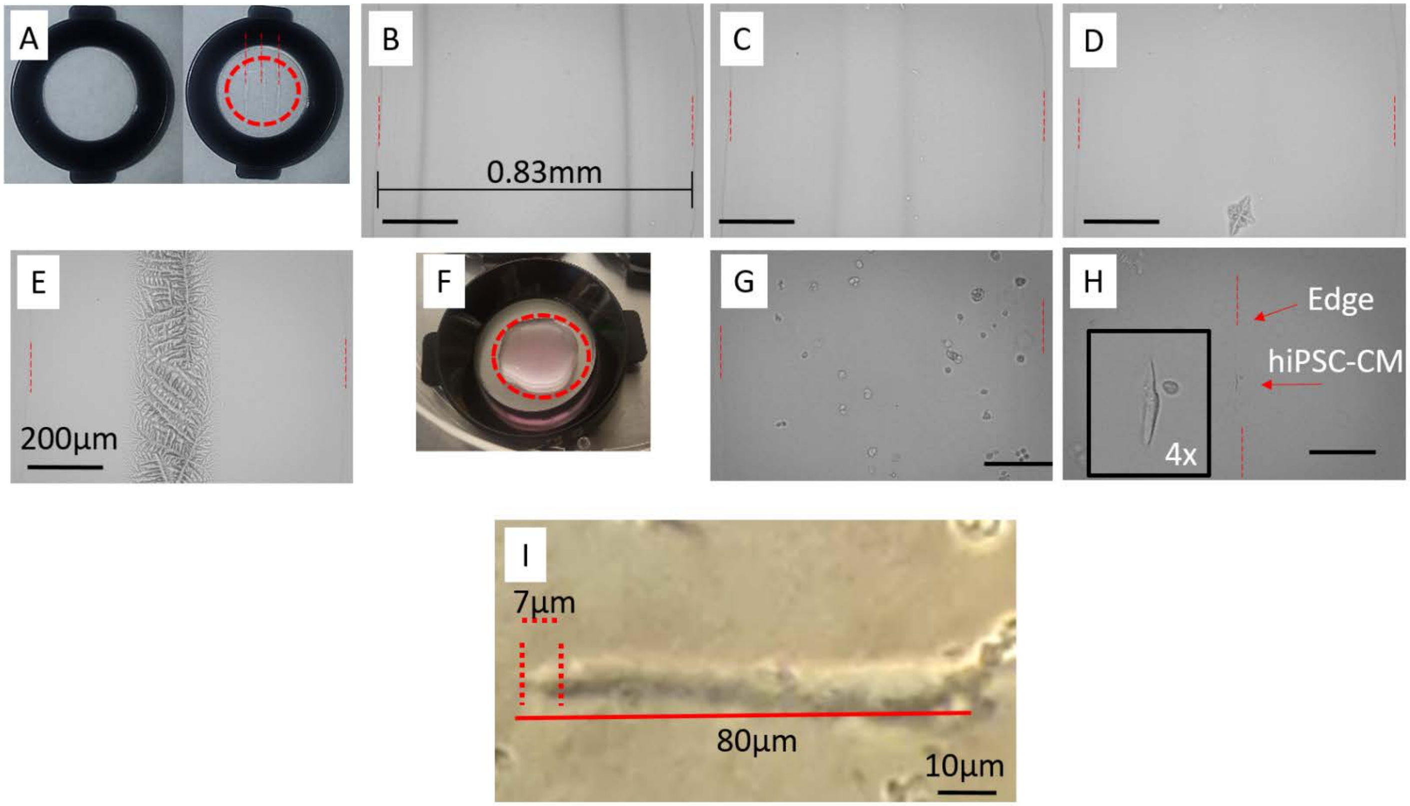

Figure 9: **Seeding of cells on Matrigel mattress**. **A)** Delta TPG dish with three lines of Matrigel mattress. **B)** Representative bright field image of freshly drawn Matrigel Mattress after 1 minute (note dark vertical line interior to the red dashes lines, this is the Matrigel beginning to dry). **C)** Mattress after 2 minutes. **D)** Matrigel mattress after 7 minutes (note initiation of Matrigel polymerization). **E)** Matrigel mattress after 8 to 10 minutes of drying (note line of polymerized Matrigel extending throughout mattress). **F)** Representative image of Delta TPG dish with cell containing media confined over Mattress. Red lines denote vertical position of Matrigel mattress, dashed circle denotes area in which Matrigel is drawn. **G)** hiPSC-CM immediately after seeding cells onto Matrigel mattress. **H)** Image of cell beginning to spread on Matrigel mattress after 12 hours of seeding. All images are at 20x with scale bar representing 200 µm. Inset depicts 4x magnified view of the hiPSC-CM. **I)** Representative image of a hiPSC-CM at 5 days post plating on Matrigel mattress. Dashed vertical red lines represents estimated distance of cell shortening. Scale bar represents 10 µm.

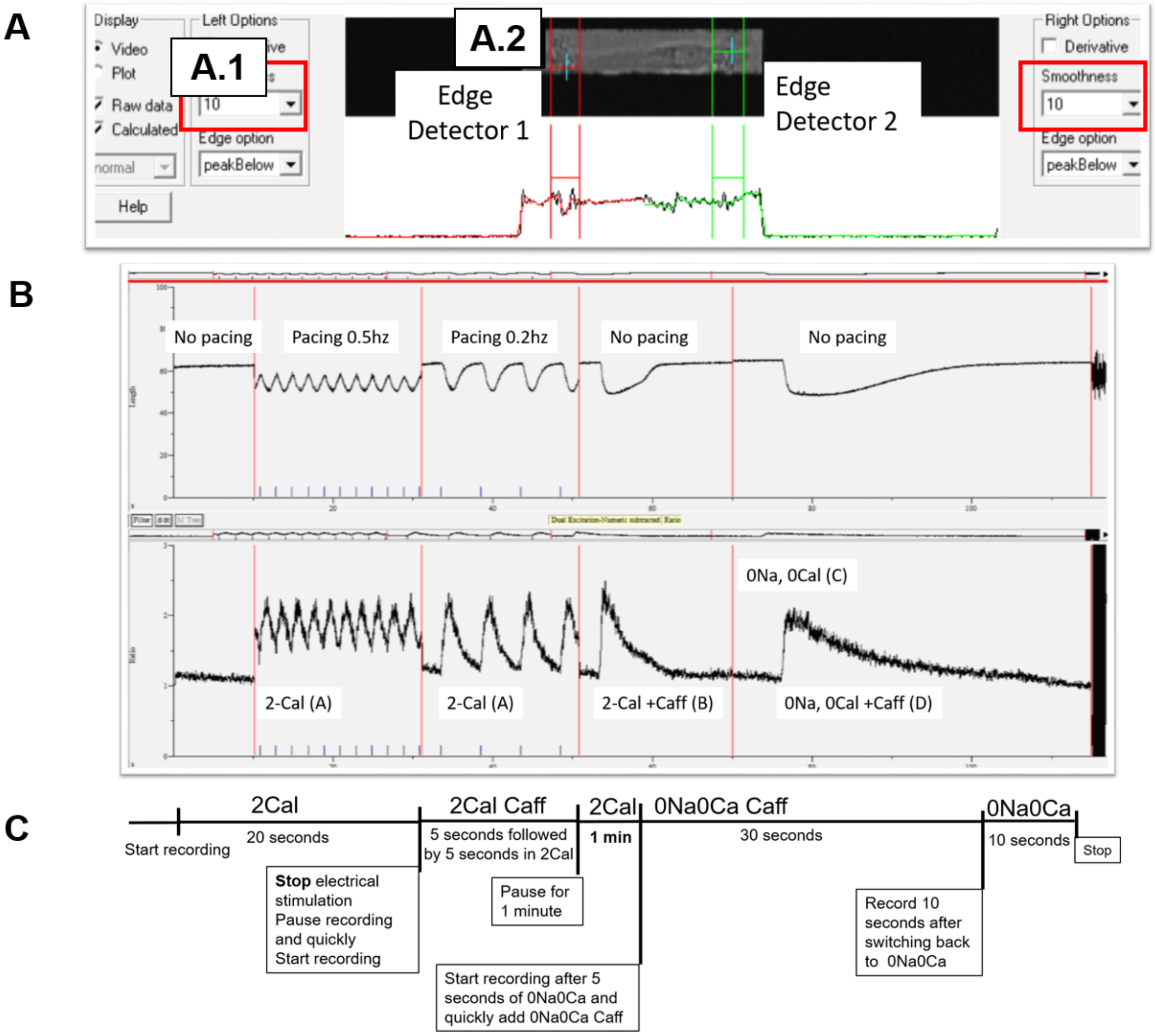

Figure 10: **IonOptix protocol for measurement of intracellular calcium and contractility**. **A)** Example of hiPSC-CM in IonOptix viewing aperture on IonWizard software prior to data collection. Note “Smoothness” of 10 **(A.1)** and placement of edge detectors **(A.2)**. **B)** Example calcium transient of single hiPSC-CM during conditions described in **C)** including 2 mM calcium containing Tyrode’s (2Cal), 10 mM caffeine in 2 mM calcium containing Tyrode’s (2Cal caff), 10 mM caff in 0 sodium, 0 calcium containing Tyrode’s (0Na0Ca caff), and 0 sodium, 0 calcium containing Tyrode’s (0Na0Ca).

(0.6 µm single electrode) were coated with 50 µl of 1:100 Matrigel diluted in DMEM/F12 and stored at least 1 hour at 37 °C prior to use. At day 25-30 of the chemical differentiation process, hiPSC-CM were dissociated and seeded into the Matrigel coated wells. Freshly differentiated hiPSC-CM were washed with 1x DPBS without calcium and magnesium and incubated in 1 mL of TrypLE Express (Life Technologies) for 10 minutes at 37 ºC. A 10 mL serological pipet was then used to add equal volumes of M3 to neutralize TrypLE and for resuspension. Gentle spraying of M3 with the 10mL serological pipet was performed for enhanced cell removal. Cells were centrifuged at 200 x g for 5 minutes, re-suspended in 3 mL of M3, and filtered through a 40 µM filter (Falcon). 65,000 hiPSC-CMs in a final volume of 200 µl per well were added to CE96 sensor plates using an 8-channel multichannel pipet. Cell mixture was added to a sterile reagent reservoir. HiPSC-CM were mixed by gently pipetting up and down in the sterile reagent reservoir between additions of hiPSC-CM to each new column of the 96 well plate. This was done to ensure equal seeding of cells. Following addition of hiPSC-CM, sensor plate was left undisturbed at room temperature for 30 minutes prior to returning plate to incubator. M3 media was refreshed on a daily basis using two 100 µl media changes for 3 days following plating. For the remaining days, a full 200 µl media change was performed daily practicing caution to not touch the pipet tip to the bottom of the well.

Evaluation of Impedance of hiPSC-CM in Monolayer: Contractility parameters of hiPSC-CM in monolayer were measured using the CardioExyte96 as previously described[39]. Electrical stimulation set at 1 Hz with 25% burst amplitude was first used for CM activation. Briefly, a complete media change with M3 was performed at least 1 hour prior to experimental recording session. A test recording (sweep) was performed at day 5 to ensure viability of monolayer followed by experimental protocol at day 10. Measurements were acquired at 37 degrees C, 80% humidity, and 5% CO_2 at an acquisition rate of 0.1 ms for extracellular field potential (EFP) and 1 ms for impedance (IMP). Combined EFP and IMP measurements were collected, however due to frequency dependent variability of EFP, only IMP at 1 Hz were analyzed for contractility.

Data Processing: Data files generated by the instrument were saved to a shared storage space accessible by a PHP web application interface as well as a backend processing script written for the BASH shell. Files ready to be analyzed were selected in the web interface using a dropdown list of folder names and matrix of checkboxes representing the wells of the sample plate. After entering a name for the output and submitting the form, the web interface launches the backend script with the user-provided parameters executing the following steps: 1) A list of the selected data files (one per well) was ordered column-first. 2) The “time” data column of the first file was extracted, converted to seconds, and is saved to the output file. 3) Finally, the script looped over the ordered list of selected data files, extracted the study data column, and appended it to the output file. Operations in the script were performed using the “awk”, “sed” and “paste” command line utilities. The resulting output was then opened and analyzed using LabChart 7.0 (ADInstruments). Impedance amplitude values were multiplied by (-1) for accurate peak detection on LabChart. Data conversion tools were designed by Christian Shaffer of the Roden laboratory.

Impedance Data Analysis: Impedance analyses were performed using “Peak Analysis” tools subsequent to data importation in LabChart. The peak analysis tool was configured for analysis of a general-unstimulated waveform tuned for sinusoidal shape detection. Adjustment of detection threshold is manipulated to allow for individual peak detection. Whole channel analyses provided waveform measurements for all individual peaks within 20 seconds of recorded activity. Baseline was set as the minimum value between peaks where “Tstart” lies within 5% of the height away from baseline and “Tend” was set to 0% of height away from baseline. Using these settings, key features of the impedance waveform assessed included peak height, time to , Time rise (10% to 90%), time fall (90% to 10%), and waveform pulse width (at 30, 50 and 90% of peak height). Period is also identified for each well to facilitate data quality control. Individual data points were comprised of average data from 20 seconds of recordings from a single well of a single sweep.

CRISPR/Cas9 Gene Editing of Patient-Derived hiPSC: Gene editing of patient hiPSC was carried out in three steps: 1) gRNA and repair template design and construction, 2) delivery, and 3) confirmation of gene editing largely adapted from[35].

Guide RNAs (gRNA) were designed using freely available online software from the Zhang lab (crispr.mit.edu). User specified target DNA sequence (*LMNA* exon 9 sequence) was submitted for optimal gRNA selection (20 nucleotides followed by the NGG PAM amenable to genome cutting with the *S. pyogenes* Cas9) with limited off-target homology. A 26-mer oligonucleotide containing the gRNA targeting exon 9 of *LMNA* and Bbsl compatible 5’ overhangs was synthesized: forward sequence 5’-CACCGgagttgatgagagccgtacgc-3’ and reverse sequence 5’-AAACgcgtacggctctcatcaactcC-3’ (Sigma). Note additional “G” preceding 20nt gRNA is inserted to optimized efficiency of the U6 promoter as recommended by the Zhang lab. Optimal gRNA was then ligated into a pSpCas9(BB)-2A-Puro (Addgene #Px459v2) expression system utilizing the Bbsl restriction site. The Px459 plasmid is an expression system containing a U6 promoter driving the sgRNA expression with a CMV promoter driving the human codon optimized *S. pyogenes* Cas9. E. coli (DH5α) were then transformed with the plasmid, bacteria expanded, and plasmid isolated prior to sequence verification using Sanger sequencing.

Repair template for facilitating homology directed repair (HDR) included alteration of the PAM site and addition of a restriction enzyme site HpyCH4IV (underlined) using silent mutations (bolded) to preserve amino acid sequence 5’-TTTCTCCTCTCCAGATCTGGGCTGCAGGAGCTGGGGCCACCCACAGCCCCCCTACCGACCTGGTGTGGAAGGCACAGAACAC**g**TGGGGCTGCGGGAACAG**t**CTGCGTACGGCTCTCATCAACTCCACTGGGGAAGTAAGTAGGCCTGGGCCTGGCTGCTTGCTGGACGAGGCTCCCCCTGA-3’. Repair template was synthesized and page purified prior to resuspension at 10µm.

For delivery of plasmid and repair template into hiPSCs, cells were first dissociated using 0.5mM EDTA in 1x PBS without $CaCl_2$ or $MgCl_2$ and singularized by filtration using a 30µm filter. HiPSCs were re-suspended in electroporation buffer with 10µmol repair template and 10µg of gRNA containing plasmid allowing for reagent delivery via electroporation (Neon System, ThermoFisher). Electroporated hiPSCs were seeded on 1:200 growth factor reduced Matrigel coated 10-cm culture dishes for expansion. Following puromycin selection, single expanded colonies were manually transferred and expanded in 24-well culture dishes. DNA was isolated (EpiCentre) for PCR amplification of exon 9 of *LMNA* followed by restriction digest using HpyCH4IV. Clones which showed selective cutting at the engineered HpyCH4IV restriction enzyme site were considered “positive hits” and Sanger sequenced for confirmation of successful gene editing.

Clones showing successful gene editing defined by insertion of the PAM mutation, insertion of the restriction enzyme site, and removal of duplicated cytosine nucleotide were further assessed for off-target cutting. Predicted off-target sites are regions of the genome in which the engineered gRNA has partial homology thus allowing for the possibility of unwanted genomic insertions and/or deletions. To ensure the absence of unwanted genomic changes, the Zhang CRISPR design tool was used to predict off-target sites targeted by the gRNA. Predicted exonic regions were PCR amplified and evaluated using Sanger sequencing (*PHTF1*, *HDAC4*, *KLC4* and *LARS2*).

Statistics: GraphPad Prism v7 was utilized for testing statistical differences with Student's t-tests or, when applicable, ANOVA followed by post hoc analysis. P-values of < 0.05 were considered statistically significant. All data are presented as mean ± SEM.

RESULTS

Clinical Evaluation

A seven-member multigenerational family was recruited for the study **(Figure 11A)**. The proband was a Caucasian male diagnosed with DCM at the age of 30. He subsequently received a pacemaker to manage his high grade atrioventricular block and bradycardia at the age of 31. His cardiac function deteriorated substantially from an ejection fraction (EF) of 35% at the age of 33 to an EF of 10% by the age of 35 when he ultimately received a heart transplant. Due to the proband's family history of conduction system disease and severe heart failure a comprehensive cardiomyopathy panel (GeneDx) was completed. Next-Generation sequencing of coding regions of 91 genes was used to probe for the causative mutation. Genetic analyses identified a single nucleotide duplication within exon 9 of *LMNA* (c.1526dupC) resulting in the change of Threonine to Tyrosine at amino acid position 510 with a subsequent downstream premature termination codon (PTC) at position 42 of the new reading frame (T510YfsX42). The mutation is predicted to cause a truncation and/or loss of function of the protein product. Although the mutation is classified as pathogenic based on co-segregation studies, cellular models to study this mutation are lacking[136-138]. Similarly, the c.1526dupC mutation was not found in ~140,000 individuals in the Genome Aggregation Database (http://gnomad.broadinstitute.org) suggesting it is not a common benign variant in the population[139]. Evaluation of the proband's family revealed that the T510YfsX42 mutation co-segregated with the cardiac phenotype in three of the four relatives. The youngest carrier did not demonstrate cardiac structural or functional abnormalities, however early rhythm abnormalities (atrial fibrillation) were detected **(Figure 11B)**. The three relatives with DCM demonstrated a similar clinical history with early detection of conduction system

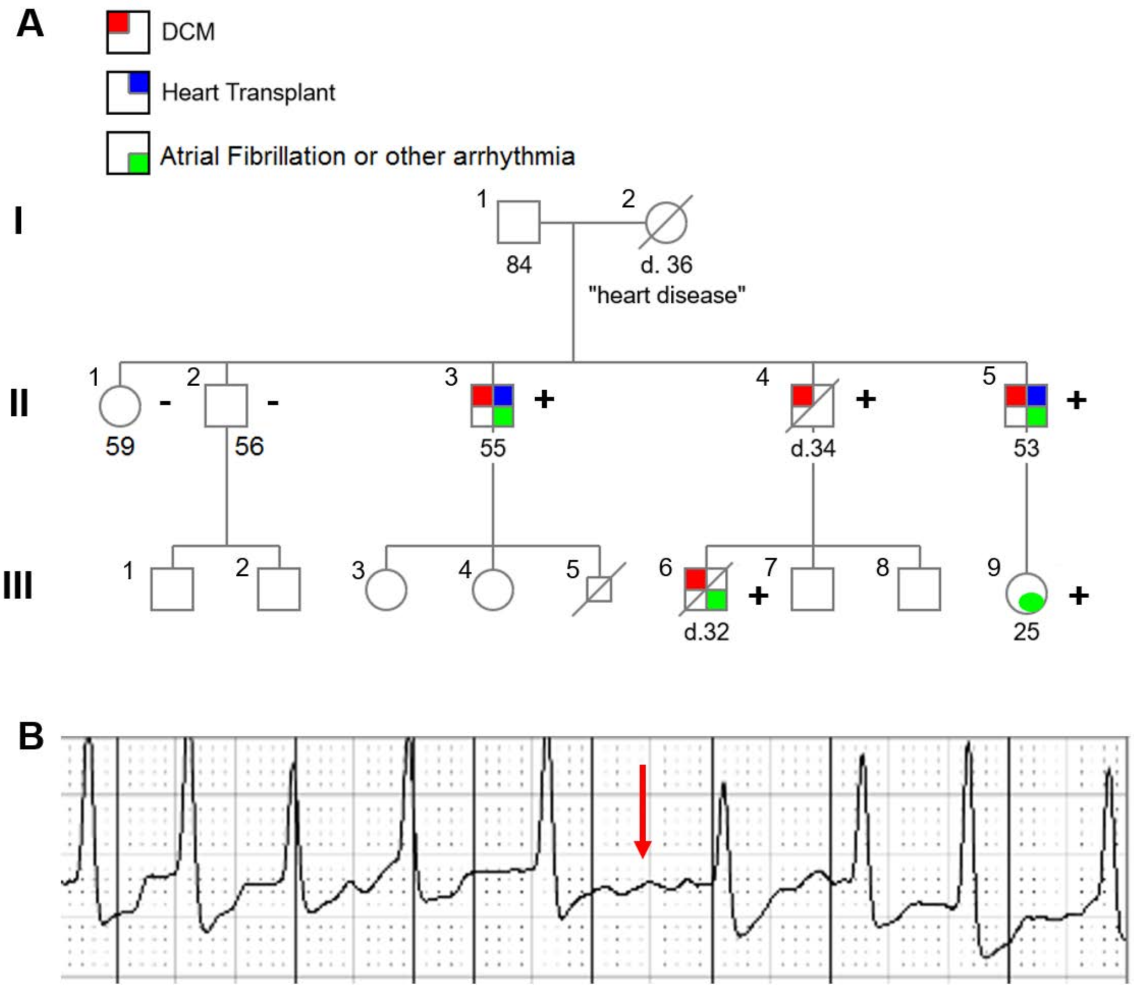

Figure 11: **Pedigree of family with DCM and *LMNA* mutation. A)** Tri-generational pedigree of a family with severe dilated cardiomyopathy (DCM) and conduction abnormalities. Red indicates diagnosis of DCM, blue indicates that the patient received a heart transplant, and green indicates the identification of rhythm disturbances including atrial fibrillation and atrioventricular block. Family members who participated in genetic evaluation are indicated as (+) or (-) for the presence or absence of the c.1526dupC *LMNA* mutation respectively. **B)** Electrocardiogram of III.9 taken at 25 years of age demonstrates atrial fibrillation. Note patient is genotype positive, but young without presence of cardiac structural of functional impairments. Clinical evaluation conducted by Quinn Wells, MD with genetic counseling by Andrea Murad, MS LGGC.

disease with subsequent rapid deterioration of cardiac function. Skeletal muscle disease was not found in any of the disease mutation carrying individuals in agreement with previous reports[138]. No genotype-negative family members exhibited cardiac abnormalities upon examination.

Generation of Patient-Specific HiPSC

Blood samples were obtained from the proband for generation of patient-specific hiPSC using non-integrating episomal based approaches (**Figure 12A**). Three independent clones were generated and found to display normal pluripotent cell characteristics including self-renewal and high nuclear/cytoplasmic ratios with prominent nucleoli. Karyotype analysis revealed a normal karyotype 46, XY, devoid of any gross chromosomal abnormalities (**Figure 12B**). Sanger sequencing of all three independent clones showed presence of the c.1526dupC versus normal sequence in the population control **(Figure 12C)**. Previously validated hiPSC derived from healthy unrelated donors were used for experimental comparison[124, 140], termed population controls.

Lamin A/C Expression in LMNA DCM HiPSC-CM is Reduced

The c.1526dupC mutation within *LMNA* on exon 9 generates a PTC at position 42 of the new reading frame. The pathogenicity of mutations resulting in a PTC in the *LMNA* gene has been attributed to both dominant negative effects as well as haploinsufficiency. Whether the c.1526dupC mutation results in loss of function of the protein due to nonsense mediated decay or if a fragment is generated remains undetermined. Western blot analysis of day 40 hiPSC-CM generated using chemical differentiation methods was used to examine both lamin A and lamin C protein expression[51]. LMNA DCM hiPSC-CM showed a significant reduction in both

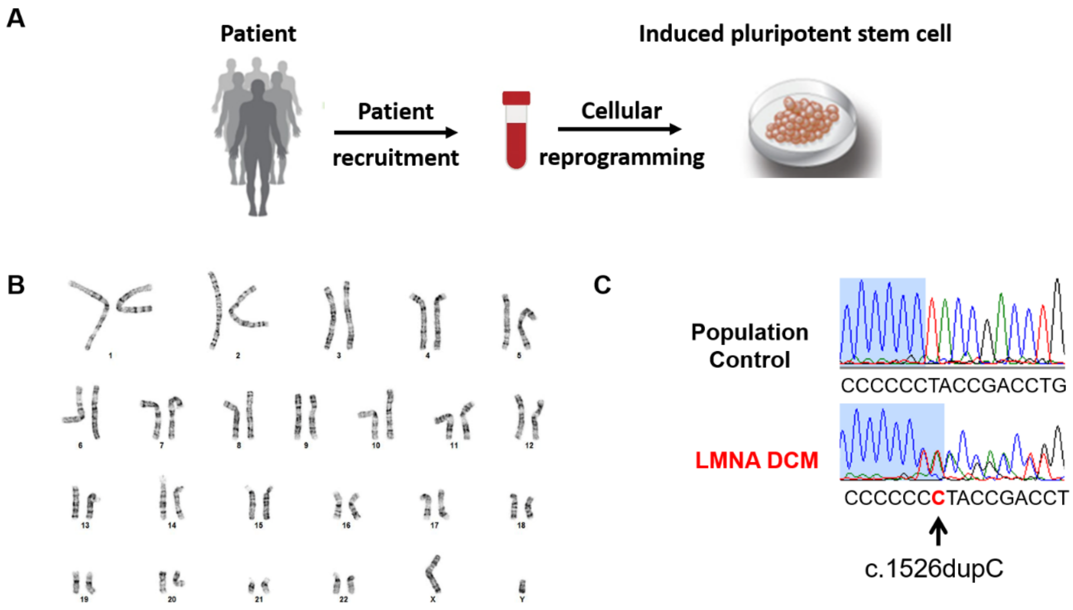

Figure 12: Generation and Validation of Patient-Specific HiPSC-CM. A) Schematic for generation of hiPSCs from patient cells. Cells were isolated (in this case peripheral blood mononuclear cells) and electroporated with non-integrating episomal plasmids containing reprogramming factors. **B)** hiPSCs were then karyotyped for evaluation of genomic stability such that no gross chromosomal aberrations are present. Karyotype for 1 of 3 independently generated hiPSC lines is shown. **C)** Representative chromatogram of Sanger sequencing of exon 9 from population control versus patient derived cell line. Note presence of cytosine at c.1526 such that subsequent nucleotides are out of frame. Karyotyping courtesy of Maria Blair, MS.

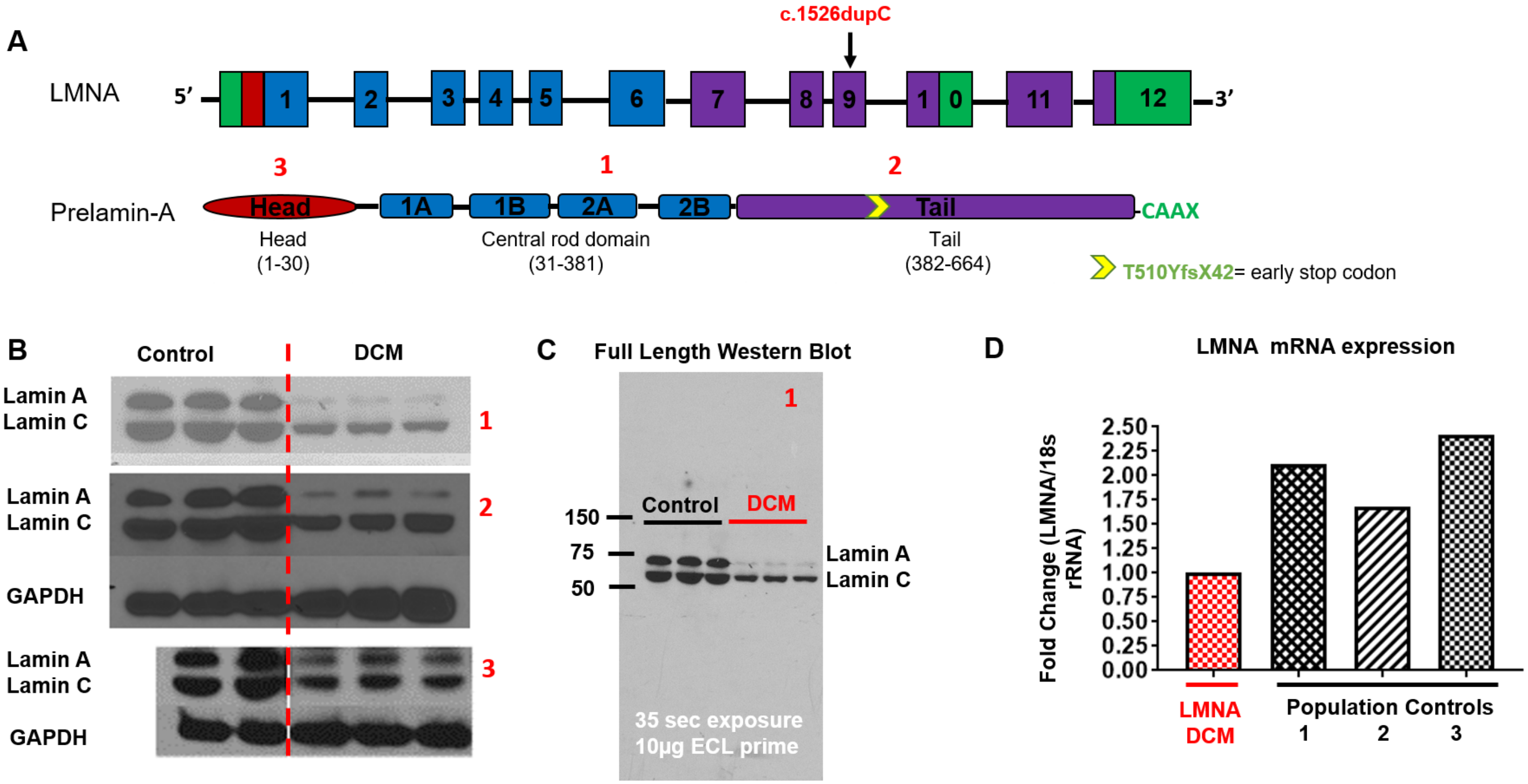

Figure 13: Lamin A/C Expression in LMNA DCM HiPSC-CM is Reduced. A) Illustration of *LMNA* gene and prelamin-A protein showing head region, central rod domain, and tail domain. Lamin A and C are identical for the first 566 aa but have distinct tail domains. Lamin A includes part of exon 10 and the entirety of exons 11 and 12, whereas lamin C includes exon 10 but lacks exon 11 and 12. Numbers 1-3 signifies approximate region of antibody recognition. In yellow is the position of the early stop codon in the patient line. **B)** Western blot of population control hiPSC-CM and LMNA DCM line using three distinct antibodies. **C)** Full length western blot shows absence of lamin fragment in DCM hiPSC-CM. **D)** Representative qRT^{2}PCR based fold change of LMNA/18sRNA mRNA expression between population controls and LMNA DCM line generated from the proband. Data shown as fold change relative to expression found in the DCM line from 2 independent inductions from multiple population controls and proband. Data collected and analyzed by Shan Parikh (Unpublished).

lamin A and C compared to the population control when using any of three antibodies targeting distinct regions of the protein (both the N-termini and towards the C-termini) **(Figure 13A-B)**. Compared to the relatively equal amounts of both lamin A and C in controls, LMNA DCM hiPSC-CM show a preferential reduction in lamin A versus lamin C. No truncated form of lamin A or C was detected in full length western blot regardless of region of protein targeted **(Figure 13C)**. Taqman based probes targeting an exon-exon border in the 5’ region of the lamin transcript identified a reduction in lamin mRNA compared to three population controls **(Figure 13D).** Similar reductions in mRNA were found when compared against another independently generated proband line (data not shown). Taken together, the reduction in lamin mRNA, the lack of fragment detection, and severe reduction in both lamin A/C protein suggests non-sense mediated decay of the protein. However, the disproportionate reduction in lamin A compared to lamin C protein could also indicate a more complex regulation of lamin A/C expression.

Single LMNA DCM hiPSC-CM Cultured on Matrigel Show Abnormal Nuclear Shape

LMNA mutations cause severe alterations in nuclear morphology including nuclear blebbing, elongation, loss of nuclear membrane, and micronuclei formation[119]. Ultrastructural investigation of human heart samples (although potentially confounded due to presence of heart failure) from patients harboring the c.1526dupC mutation have shown misshapen nuclei as evidenced by the irregular contour nuclear membrane, elongation, and “cauliflower” appearance[136]. Prior studies of *LMNA* mutation carrying hiPSC-CM cultured on stiff culture dishes did NOT demonstrate baseline nuclear defects, however; electrical field stimulation was sufficient to uncover nuclear blebbing and shape abnormalities[119]. However, C2C12 cells and neonatal rat ventricular CM overexpressing mutant lamin[141, 142], show significant alteration in nuclear shape

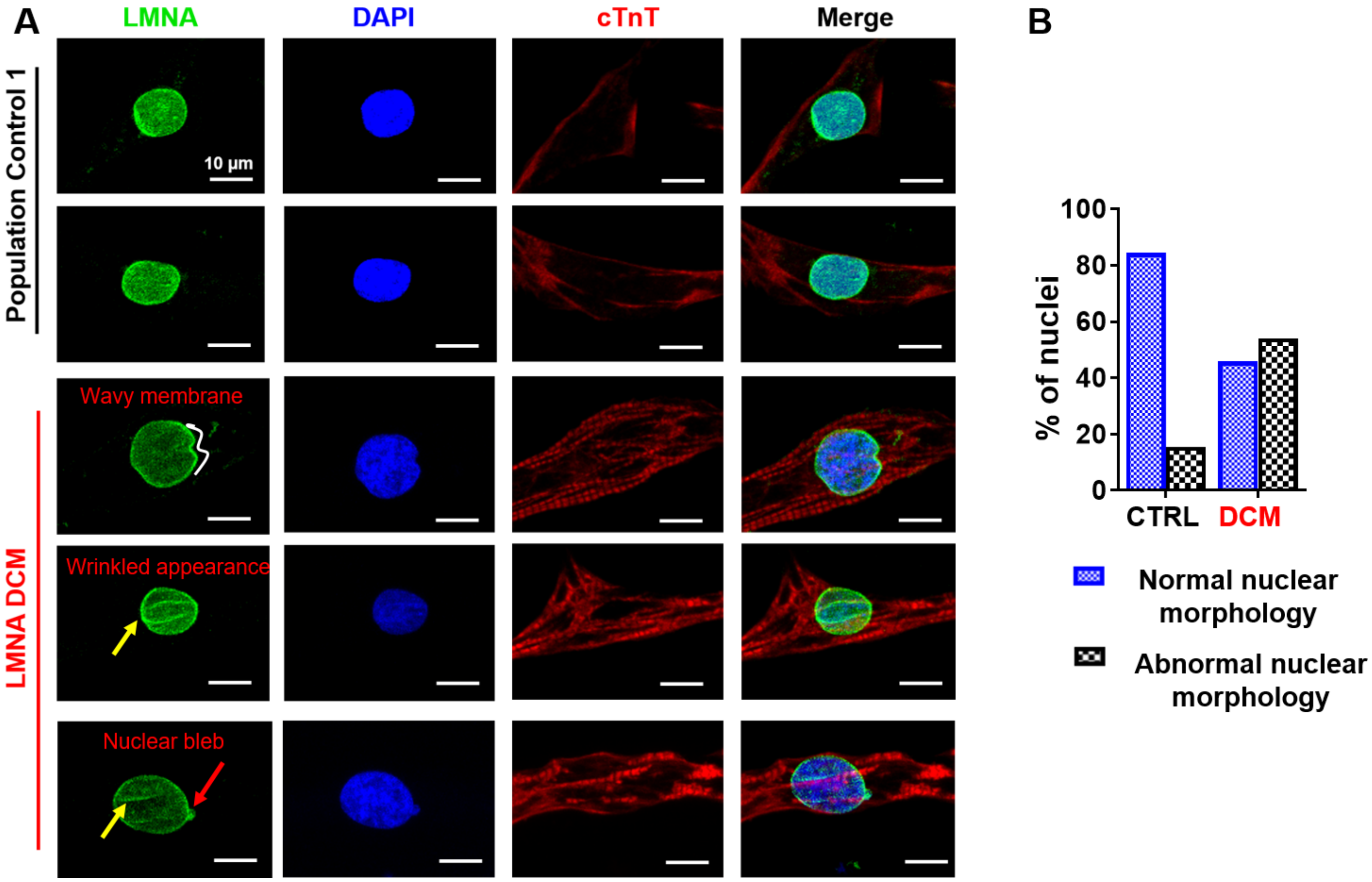

Figure 14: Single LMNA DCM HiPSC-CM Cultured on Matrigel Show Abnormal Nuclear Shape. A) Confocal images of hiPSC-CM cultured on Matrigel mattress and stained with lamin A/C (green), DAPI (blue), and cardiac troponin-T (red). Scale bar is 10 µm. White wavy line indicates abnormal nuclear shape, yellow appear indicates nuclear wrinkles, and red arrow indicates nuclear bleb. **B)** LMNA DCM hiPSC-CM demonstrate a greater % of nuclei with abnormalities (nuclear bleb, wavy membrane, and/or wrinkled appearance) compared to control. Data indicate percentage of nuclei of total per cell line (n = 103 ctrl, and 96 LMNA DCM from 21 frames each, 1 cardiac differentiation).

(e.g.: elongation, blebbing, and reduced circularity at baseline). As such, to investigate whether nuclear abnormalities are present in LMNA DCM hiPSC-CM at baseline, cells were matured on Matrigel mattress (where they spontaneously exhibit up to 10% cellular shortening) and lamin A/C visualized using confocal microscopy **(Figure 14)**. Lamin appropriately localized at the nuclear membrane as expected in both healthy control and LMNA DCM hiPSC-CM. Consistent with the absence of lamin A/C fragment detection on full length western blot, no abnormal accumulation or cytosolic localization of lamin was identified. Although reductions in lamin A/C intensity were not readily observed, LMNA DCM hiPSC-CM did display abnormalities in nuclear shape **(Figure 14A, B).** LMNA DCM hiPSC-CM showed blebbing of the nuclear membrane and abnormal shape including wrinkling and abnormal contour of the membrane. Further investigation of nuclear abnormalities is warranted, specifically to investigate whether prolonged culture or enhanced maturation techniques further provoke nuclear abnormalities. While these results are encouraging, evaluation of multiple differentiations and comparison with isogenic control will allow for more accurate assessment of nuclear abnormalities.

Single LMNA DCM hiPSC-CM reveal alterations in calcium handling and contractility

Patients with LMNA cardiomyopathy demonstrate a severe, progressive deterioration of contractile function during the course of their disease. Using hiPSC-CM for modeling this disease may provide insight on the cell-intrinsic mechanisms underlying this contractile dysfunction in patients with LMNA cardiomyopathy. However, previous studies using hiPSC-CM for modeling LMNA DCM do not report contractile dysfunction and/or pro-arrhythmic features [119, 120]. Despite the severe contractile dysfunction observed in humans and in mouse models of lamin cardiomyopathy[143, 144], a recent evaluation of excitation-contraction coupling of single hiPSC-CM did not identify deficits in calcium kinetic or contractile parameters[120]. As hiPSC-CM plated on plastic or glass culture dish do not exhibit sufficient cell shortening for accurate assessment[88], the Matrigel mattress method developed in our lab[59] was used here for measurement of contractility and calcium handing in single hiPSC-CM.

Edge detection based evaluation of cellular shortening of day 35 LMNA DCM hiPSC-CM electrically stimulated at 0.2 Hz did not show significant deficits in cellular shortening compared to population control **(Figure 15A).** However, contractile kinetics revealed impairments in time to peak contraction and in return to baseline in LMNA DCM hiPSC-CM compared to population control **(Figure 15B-D and Table 2)**.

Calcium kinetics were assessed using the ratiometric calcium indicator Fura-2 AM in electrically stimulated hiPSC-CMs at 0.2 HZ **(Figure 16)**[59]. Although diastolic and peak Fura-2 fluorescence of the calcium transient were not significantly different between groups, both time to peak and calcium decay rates were significantly prolonged in LMNA DCM hiPSC-CM compared to population control (**Figure 16A-E and Table 3).** To determine mechanisms responsible for the impaired calcium removal, the relative contribution of each calcium extrusion pathway was calculated using the flux balance method **(see Chapter 1, Figure 8 for more detail)**. Calcium decay rates were significantly prolonged in LMNA DCM hiPSC-CM compared to control **(Figure 16D, E)**. In addition to the overall delay in total calcium removal, the slow extrusion pathway (mitochondrial and other non-SERCA/NCX pathways) was significantly impaired **(Figure 16E and Table 3).** LMNA DCM hiPSC-CM exhibit deficits in both cellular contraction and relaxation consistent with impairments in calcium handling observed. Although maximal cell shortening was not affected in the LMNA DCM hiPSC-CM, the impairments in contractile kinetics and relaxation and the underlying calcium handing provide evidence for early signs of contractile dysfunction.

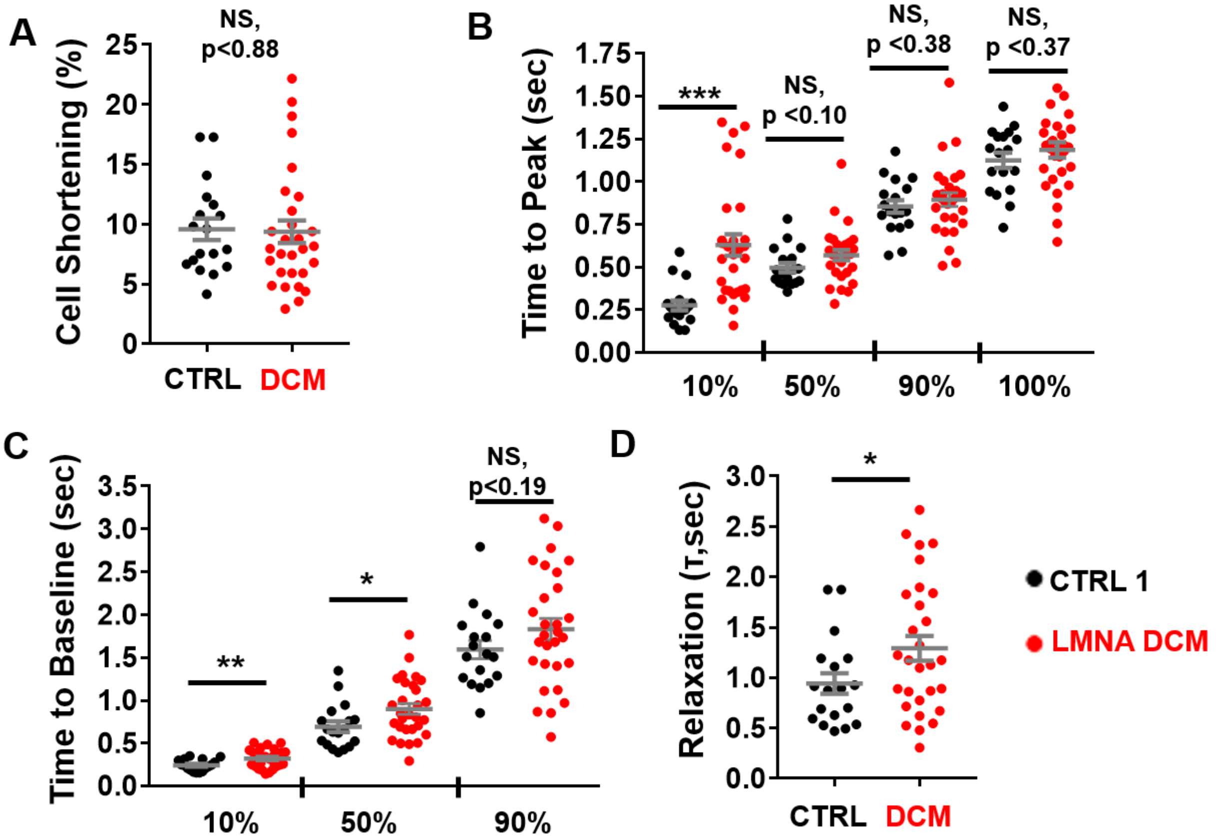

Figure 15: Single LMNA DCM HiPSC-CM Show Alterations in Contractility. Ionoptix assessment of single hiPSC-CM electrically paced at 0.2 Hz at RT do not show deficits in **A)** cellular shortening, however display significant delays in **B)** time to peak parameters, and in **C-D)** cellular relaxation kinetics. Data are mean ± SEM; n = 18 for population control and 29 for LMNA DCM lines. Unpaired, two tailed Student's t-test, $*p < 0.05$, $**p < 0.01$, and $***p < 0.001$ vs population control Data collected and analyzed by Shan Parikh.

Table 2: Contractile Kinetics Single LMNA DCM hiPSC-CM

Parameter	CTRL 1	LMNA DCM	p-value
Cell shortening (% of resting length)	9.60 ± 0.89	9.39 ± 0.94	0.88
Time to peak (s)	1.13 ± 0.044	1.89± 0.045	0.37
Time to peak 10% (s)	0.28 ± 0.028	0.63± 0.063	**0.001***
Time to peak 50% (s)	0.50 ± 0.026	0.57 ± 0.030	0.10
Time to peak 90% (s)	0.86 ± 0.037	0.90 ± 0.040	0.38
Time to baseline 10% (s)	0.24 ± 0.016	0.32 ± 0.020	**0.0082***
Time to baseline 50% (s)	0.69 ± 0.061	0.90 ± 0.063	**0.031***
Time to baseline 90% (s)	1.59 ± 0.11	1.83 ± 0.13	0.19
Tau (s)	0.94 ± 0.10	1.29 ± 0.12	**0.048***

Table 2: Contractile kinetics of LMNA DCM line vs population control hiPSC-CM paced at 0.2 Hz at RT**.** Data presented are mean ± SEM (n = 18 for CTRL and 29 for DCM). Unpaired, two tailed Student's t-test, *p < 0.05, **p < 0.01, and ***p < 0.001 vs population control. Data collected and analyzed by Shan Parikh.

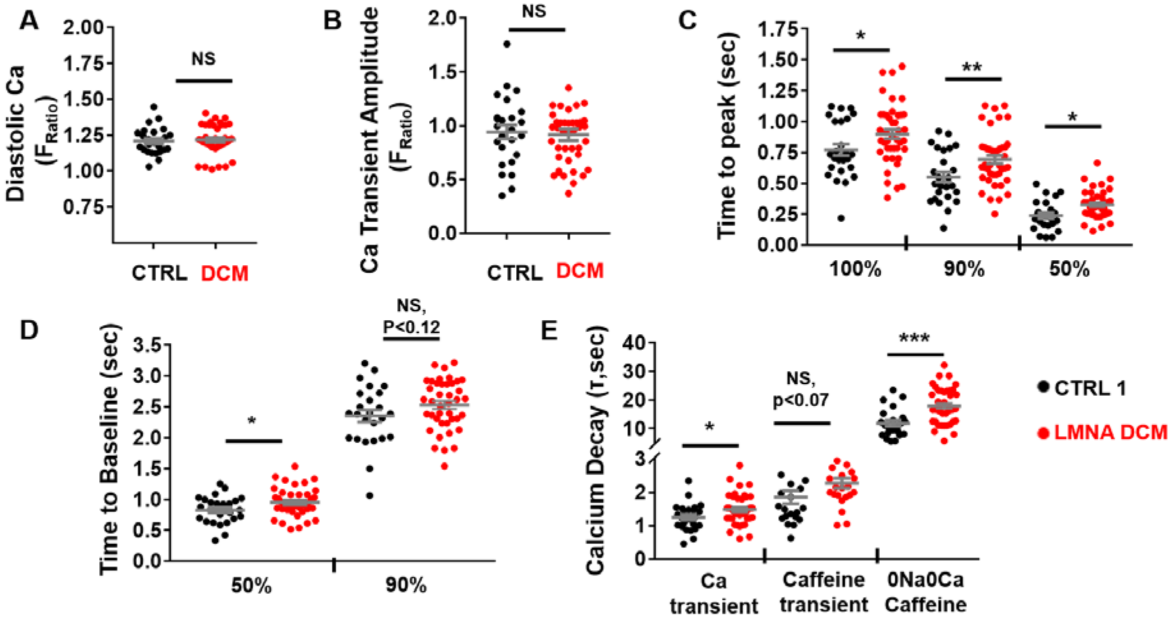

Figure 16: Single LMNA DCM HiPSC-CM Reveal Alterations in Calcium Handling. Ionoptix assessment of single hiPSC-CM electrically paced at 0.2 Hz at RT do not show differences in **A)** diastolic calcium or **B** peak transient amplitude. LMNA DCM hiPSC-CM show significant slowing of **C)** time to peak parameters as well as a **D)** delay in return to baseline. Consistent with the delay in time to baseline, multiple aspects of **E)** calcium extrusion are impaired in the LMNA DCM hiPSC-CM compared to population controls. Data are mean ± SEM; n = 21 for population control and 41 for LMNA DCM lines. Unpaired, two tailed Student's t-test, *$p < 0.05$, **$p < 0.01$, and ***$p < 0.001$ vs population control. Data collected and analyzed by Shan Parikh.

Table 3: Calcium Kinetics of Single LMNA DCM HiPSC-CM

Parameter	CTRL 1	LMNA DCM	p-value
Diastolic Ca^{2+} (F_{Ratio})	1.21 ± 0.019	1.23 ± 0.018	0.52
Ca^{2+} transient amplitude (F_{Ratio})	0.94 ± 0.064	0.92 ± 0.15	0.77
Time to peak (s)	0.77 ± 0.047	0.89 ± 0.038	**0.04***
Time to peak 50% (s)	0.24 ± 0.023	0.34 ± 0.018	**0.004***
Time to peak 90% (s)	0.55 ± 0.042	0.69 ± 0.033	**0.010***
Time to baseline 50% (s)	0.83 ± 0.045	0.95 ± 0.035	**0.037***
Time to baseline 90% (s)	2.35 ± 0.10	2.53 ± 0.064	0.12
SR Ca^{2+} content (F_{Ratio})	1.10 ± 0.061	0.98 ± 0.052	0.13
Ca^{2+} transient decay (t_{twitch}, s)	1.25 ± 0.081	1.48 ± 0.072	**0.04***
Caff decay (t_{caff}, s)	1.86± 0.19	2.28 ± 0.13	0.07
0Na0Ca Caff decay ($t_{Caff0Na}$, s)	11.84 ± 1.07	17.98 ± 1.10	**0.0002***

Table 3: Calcium kinetic measurements of LMNA DCM vs population control hiPSC-CM paced at 0.2 Hz at RT. Data presented are mean ± SEM (n = 21 for control and 41 for DCM). Unpaired, two tailed Student's t-test, *p < 0.05, **p < 0.01, and ***p < 0.001 vs population control. Data collected and analyzed by Shan Parikh.

As LMNA DCM patients generally do not display severe cardiomyopathy and/or structural abnormalities at birth, the progressive nature of this disease may require longer culture times or advanced maturation to further uncover the phenotype in hiPSC-CM.

High-throughput Contractile Phenotyping of LMNA DCM HiPSC-CM Monolayers

The Cardioexcyte96 (Nanion), a high-throughput platform allowing for impedance measurements at physiologic conditions (37°C and 60 beats/min), was used to investigate the contractile properties of hiPSC-CM monolayers. Impedance measurements of hiPSC-CM monolayers provide a correlate of cellular contractility. The impedance waveform can be parameterized into time based parameters including time to peak and time to baseline **(Figure 17A-C)** [61]. Furthermore, impedance measurements are label-free and non-invasive and can be carried out continuously over many weeks. HiPSC-CM from three independent population control lines (Ctrl 1, Ctrl 2, and Ctrl 3) and two LMNA DCM proband lines (LMNA DCM 1, LMNA DCM 2) were generated. After 30 days of differentiation, hiPSC-CM were seeded into CE96 sensor plates to form a monolayer. HiPSC-CM were allowed 10 days to form an electrically coupled monolayer before measuring impedance waveforms **(flowchart for CE96 shown in Figure 17A)**. Day 40 LMNA DCM hiPSC-CM demonstrated significant widening of the impedance waveform with slow upstroke and delayed relaxation compared to population controls **(Figure 18A).** Time based parameters such as pulse width 30, 50, and 90 were significantly prolonged in LMNA DCM lines vs population controls **(Figure 18B, Table 4)**. In addition, time-rise and time-fall between 10-90% of the peak height were significantly prolonged in the LMNA DCM lines compared to 10-90% of the peak height were significantly prolonged in the LMNA DCM lines compared to population controls **(Table 4).** Consistent with single cell data,

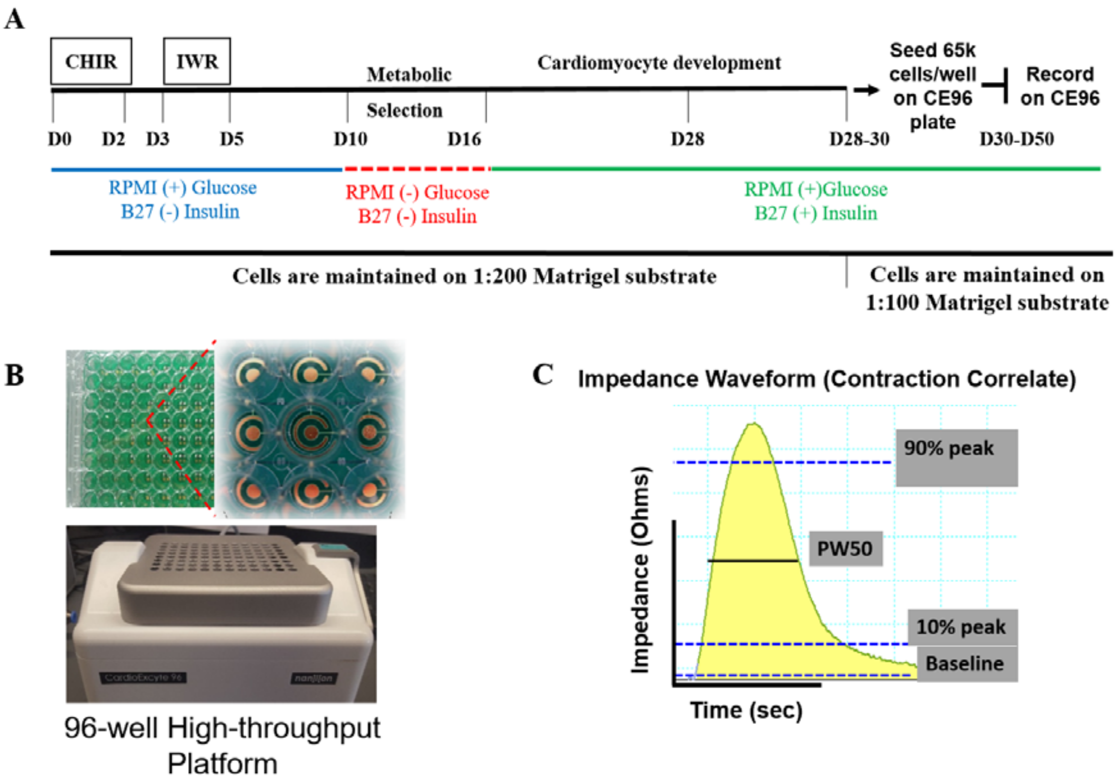

Figure 17: High-throughput Contractile Phenotyping of LMNA DCM HiPSC-CM Monolayers A) Diagram of hiPSC-CM production and implementation on the CardioExcyte96 platform, **B)** 96-well sensor plate with magnified inset of single well illustrates the central electrode surrounded by a reference electrode on which hiPSC-CM are cultured. Note benchtop Cardioexcyte96 instrument with temperature controlled chamber (lower panel). **C)** Illustrative impedance waveform visualized using LabChart software depicts aspects of contractile properties (PW50 refers to the width in seconds of the waveform at 50% of maximal peak). Figure generated by Shan Parikh.

LMNA DCM hiPSC-CM in monolayer demonstrated contractile impairment compared to three population controls. However, of the two independent clones, LMNA DCM 2 demonstrated a more severe impairment at day 40 compared to population controls, whereas LMNA DCM 1 was not significantly prolonged for all parameters **(Table 4).** As cardiac function progressively worsens over time in DCM, impedance waveforms of hiPSC-CM in monolayer were measured serially at days 30, 40, and 50 on the CE96. Although minimal differences were observed for LMNA DCM line 1 at d40, by day 50, both LMNA DCM lines were significantly prolonged compared to population control hiPSC-CM **(Figure 19A-F)**.

Using CRISPR/Cas9 to Correct c.1526dupC Mutation in LMNA DCM line

The comparison of patient derived hiPSC lines to population controls is confounded by differences in genetic backgrounds which introduce epigenetic and transcriptional variation[145]. Despite the contractile abnormalities observed in the LMNA DCM lines vs population controls, genome editing is required to establish whether findings are specific to the c.1526dupC mutation **(Figure 20A)**. For CRISPR/Cas9 mediated genome editing, gRNAs targeting exon 9 of *LMNA* were designed and validated using the T7 endonuclease assay to ensure Cas9 mediated DNA cutting **(Figure 20B-C).** Proband-derived hiPSC were co-transfected with the repair template and CRISPR/Cas9 reagents. Of 192 clones assessed, 47 contained the engineered restriction enzyme site, suggesting successful homology directed repair. These 47 lines were then expanded and the correction of the mutation was assessed through Sanger sequencing of exon 9 of *LMNA.* However, Sanger sequencing showed additional insertions/deletions surrounding the mutation site for 45 lines. The two successfully edited lines designated “Isogenic Ctrl 1” and “Isogenic ctrl 2” were used for subsequent analyses **(Figure 21A)**. Predicted off-target cutting sites were PCR amplified

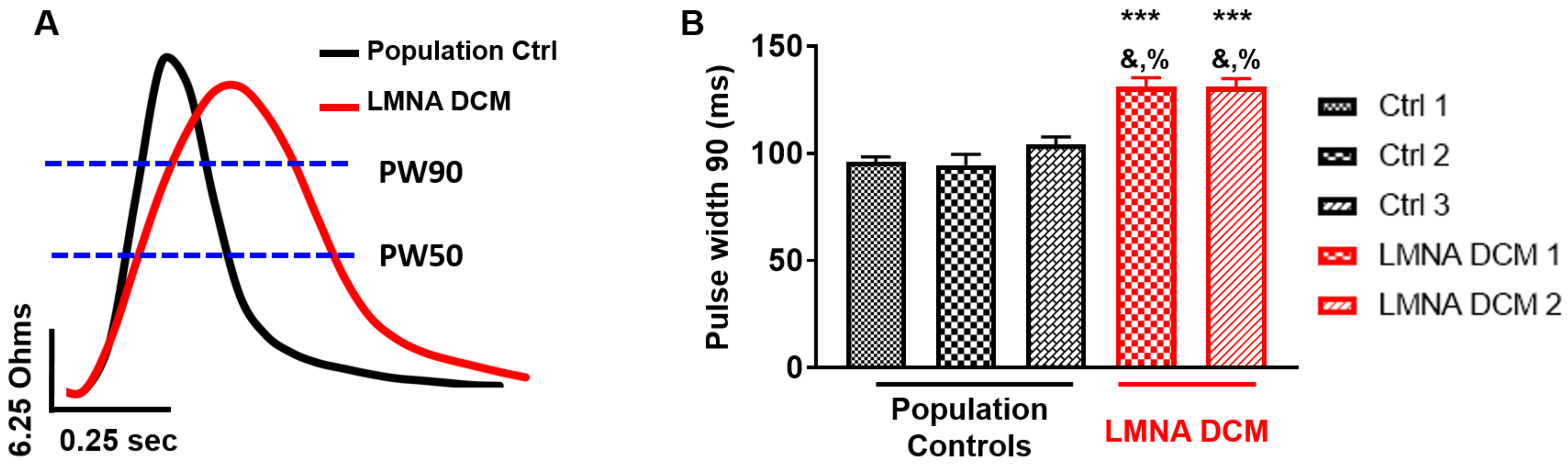

Figure 18: LMNA DCM HiPSC-CM Monolayers Show Contractile Defects. A) Representative impedance waveform of 40 day old LMNA DCM vs population control line hiPSC-CM in monolayer (PW90 indicates width at 90% of impedance waveform). **B)** Width of population controls vs LMNA DCM lines at 90% of impedance waveform. Data presented are mean ± SEM; One-way ANOVA with Tukey's post hoc test; ***p < 0.001 vs control 1, $p < 0.05 vs control 2, &&p < 0.1 vs control 3. Data collected and analyzed by Shan Parikh.

Table 4: Impedance Measurements LMNA DCM vs Population Control hiPSC-CM in Monolayer

Parameter	Control 1 (*)	Control 2 ($)	Control 3 (&)	LMNA DCM 1	LMNA DCM 2
Time to peak (s)	213.6 ± 4.7	217.9 ± 6.5	207.4 ± 5.3	228.6 ± 5.1	257.8 ± 7.7 ***, &
Time to rise 10%-90% (s)	156.5 ± 4.0	159.3 ± 4.6	144.4 ± 3.9	158.1 ± 3.9	182.4 ± 5.8 **, &
Time to fall 10%-90% (s)	225.5 ± 4.6	220.8 ±12.2	262.5 ± 4.5	251.4 ± 5.2**	249.3+ 4.0***
Pulse width 30 (s)	332.5 ± 6.4	320.2 ± 6.3	352.3 ± 4.6	384.7 ± 7.1 ***	417.4 ± 8.5 ***,&,$
Pulse width 50 (s)	259.9 ± 5.0	248.6 ± 3.1	273.2 ± 4.2	306.8 ± 6.3***	337.2 ± 7.4***,&,$
Pulse wide 90 (s)	96.2 ± 2.2	94.59 ± 4.9	104.2 ± 3.5	131.0 ± 4.3***,&&,$	131.0 ± 3.9***,&&,$
n (# of wells)	70	5	16	29	68

Table 4: Impedance waveform derived measurements of 40 day old LMNA DCM vs healthy population control hiPSC-CM in monolayer electrically paced 1 Hz at 37°C. Data presented are mean ± SEM (replicates are as indicated and pooled from at least 3 independent differentiations). One-way ANOVA with Tukey's post hoc test; **p < 0.01 and ***p < 0.001 vs control 1, $ p< 0.05 vs control 2, and &p < 0.5 and &&p < 0.1 vs control 3. Data collected and analyzed by Shan Parikh.

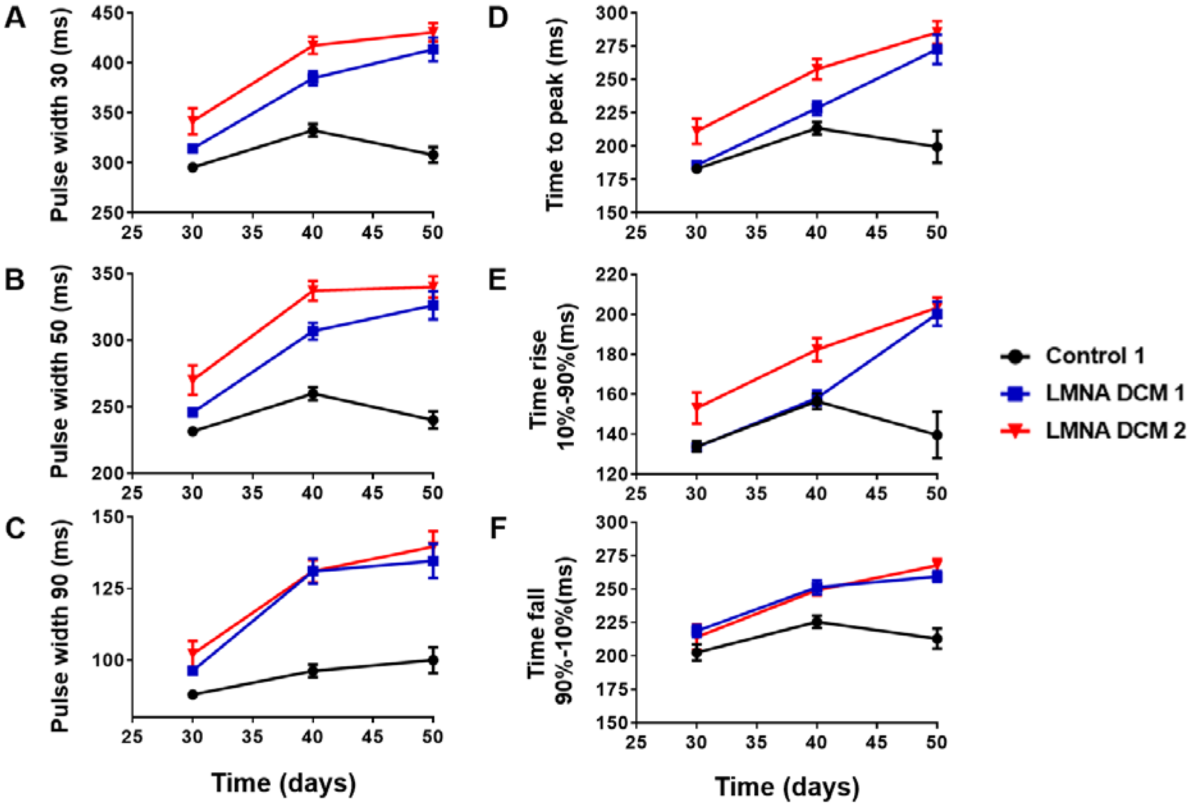

Figure 19: Temporal Impedance Measurements of LMNA DCM HiPSC-CM. Temporal changes in impedance waveform parameters show a significant prolongation in LMNA DCM lines vs minimal change in population control hiPSC-CM in monolayer. Note increased delay in pulse width of LMNA DCM line **A)** at 30% of maximal peak, **B)** 50% of maximal peak, and **C)** 90% of maximal peak vs population control line. Whereas pulse width parameters show early disparity by day 40, time to peak **(D),** time rise **(E)** and time fall **(F)** show minimal difference at day 40 but significant separation by day 50. Data presented are mean ± SEM (n = 20-70 for population control and 11-68 for LMNA DCM lines). Data collected and analyzed by Shan Parikh.

and sequenced to verify specificity of gRNA mediating cutting (data not shown). Corrected hiPSC were differentiated into CM and assessed. The CRISPR-corrected isogenic control hiPSC-CM demonstrated increased lamin mRNA and western blot analyses of lamin A/ C protein confirmed restoration of lamin A/C **(Figure 21B, C)**. As CRISPR mediated off-target mutagenesis is still a possibility, whole exome sequencing would further support accuracy of genome manipulation. Overall, these findings provide evidence for successful genome editing of the LMNA DCM hiPSC.

Impedance based assessment of CRISPR corrected hiPSC-CM in monolayer

CE96 impedance waveform parameters were analyzed to determine whether the genetic correction of the LMNA DCM line resulted in rescue of contractile abnormalities observed. Impedance waveform measurements comparing two isogenic control lines and population control show significant functional improvement compared to LMNA DCM line for majority of time based parameters **(Figure 22A-F and Table 5)**. Although CRISPR correction successfully rescued functional impairments observed in the LMNA DCM lines, not all parameters were restored. However, as CE96 impedance based measurements may not always reflect contractile parameters, single cell studies are required to further verify extent of phenotypic rescue of contractile dysfunction.

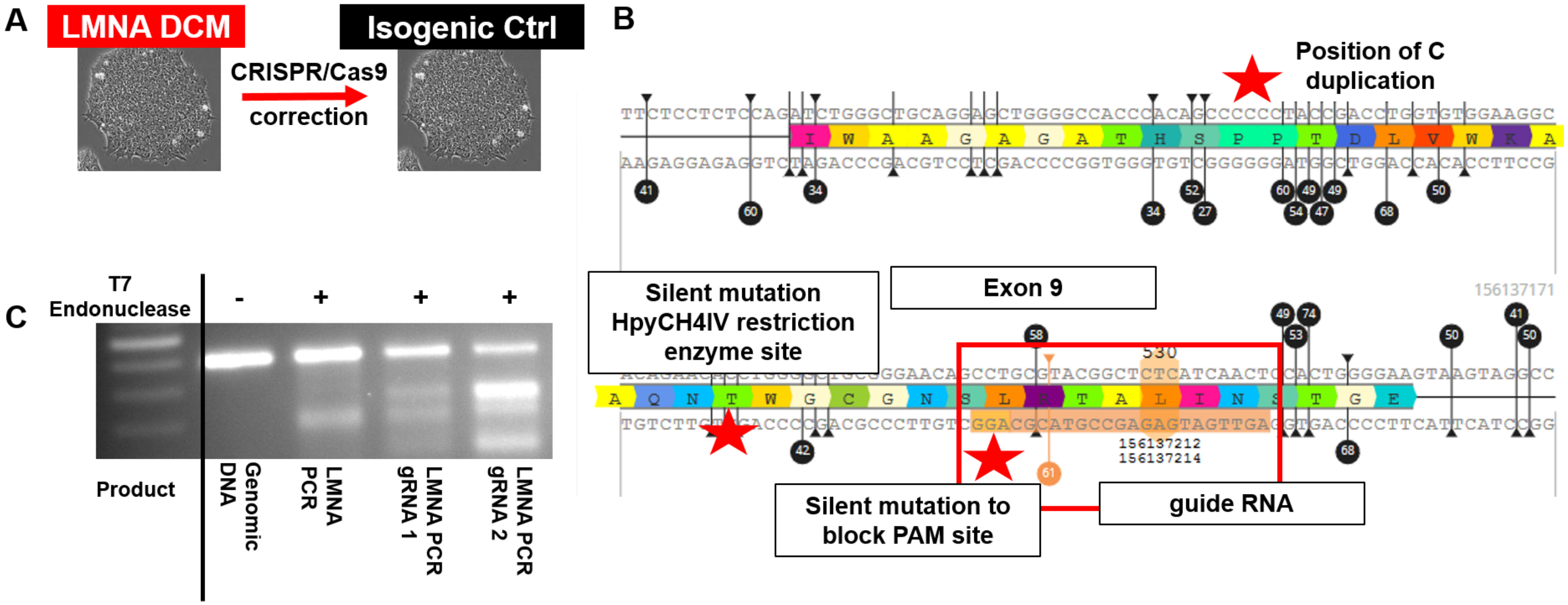

Figure 20: CRISPR/Cas9 Genome Editing of LMNA DCM HiPSC A) Schematic representing indicating genome editing of hiPSC. **B)** Sequence of exon 9 of *LMNA* indicated position of mutation, site of silent mutations for introduction of restriction enzyme site and PAM site alteration, and gRNA sequence and target. **C)** T7 endonuclease assay for verification of gRNA cutting at exon 9. Data collected and analyzed by Shan Parikh.

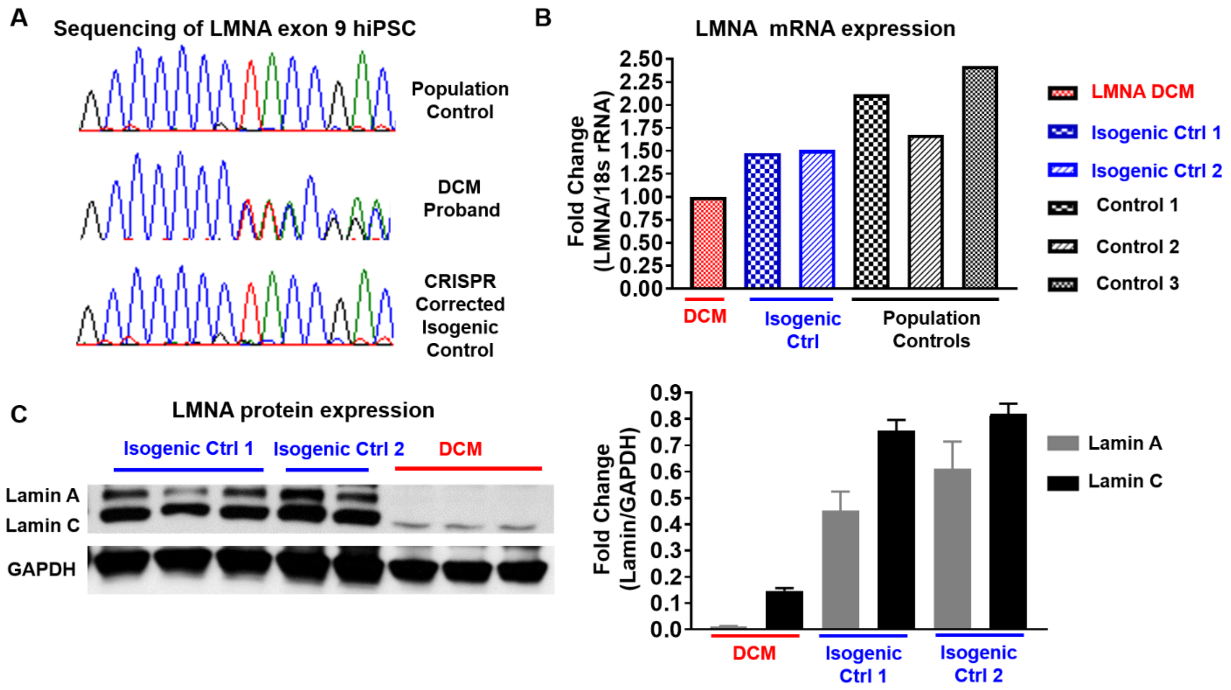

Figure 21: Genome Editing Restores LMNA mRNA and Protein A) Representative Sanger sequencing demonstrating removal of cytosine duplication in DCM proband. **B)** Representative qRT^{2}PCR fold change of LMNA/18sRNA mRNA expression between controls and LMNA DCM line show restoration of lamin in isogenic controls. Data shown as fold change relative to expression found in the DCM line from 2 independent inductions, each an average of 3 technical replicates. **C)** Western blot and quantitation of intensity of isogenic control and LMNA DCM line shows successful restoration of lamin A and C protein. Each replicate indicates independent differentiation. Data collected and analyzed by Shan Parikh.

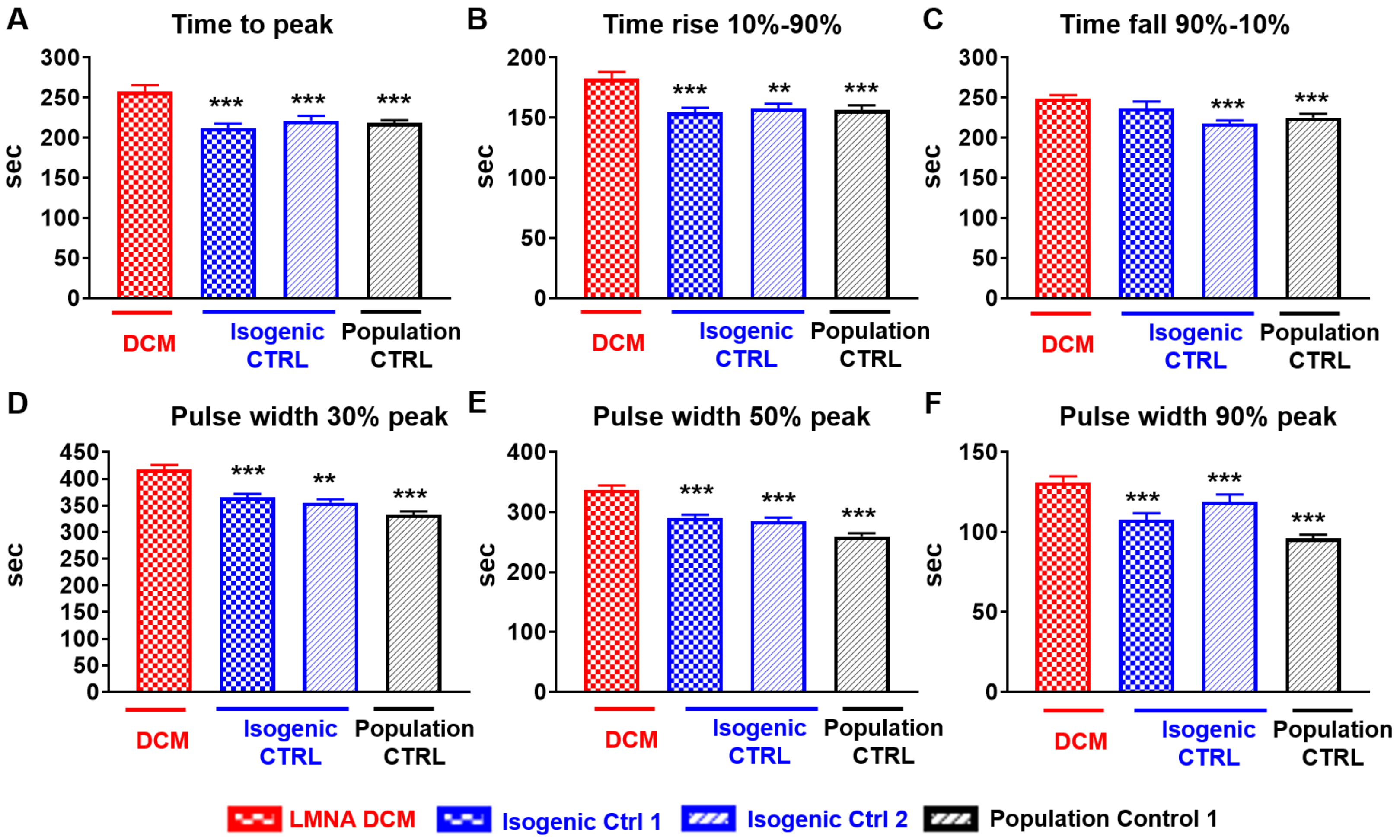

Figure 22: Gene Correction Rescues Contractile Defects. Isogenic control hiPSC-CM show rescue of impedance waveform parameters akin to population control. Note improvement in time to peak **(A),** time rise **(B)** and time fall **(C)** as well as pulse width at **D)** at 30% of maximal peak, **E)** 50% of maximal peak, and **F)** 90% of maximal peak.. Data presented are mean ± SEM (n = 68 for LMNA DCM, 61 for isogenic ctrl 1, 46 for isogenic ctrl 2, and 70 for population ctrl). One-way ANOVA with Tukey's post hoc test; ***$p < 0.01$ vs DCM. Data collected and analyzed by Shan Parikh.

Table 5: Impedance Measurements LMNA DCM vs Isogenic Control HiPSC-CM Monolayer

Parameter	LMNA DCM	Isogenic CTRL 1	Isogenic CTRL 2	Population Control 1
Time to peak (s)	257.8 ± 7.5	212.3 ± 6.1***	221.4 ± 5.7***	213.6 ± 4.7***
Time to rise 10%-90% (s)	182.4 ± 3.9	182.4 ± 5.8***	154.4 ± 4.1**	156.5 ± 3.9***
Time to fall 10%-90% (s)	249.3 ± 4.0	237.2 ± 8.1	218.2± 3.7**	225.5 ± 4.6**
Pulse width 30 (s)	417.4 ± 8.5	365.4 ± 6.5***	355.4 ±6.3**	332.5 ± 6.4***
Pulse width 50 (s)	337.2 ± 7.4	290.1 ± 5.5***	285.2 ± 5.7***	259.9 ± 4.9***
Pulse wide 90 (s)	131.0 ± 3.9	107.8 ±4.04***	118.9 ±4.67***	96.2 ± 2.2***
n (# of wells)	68	61	46	70

Table 5: Impedance waveform measurements of 40 day old LMNA DCM vs isogenic and healthy population control hiPSC-CM monolayers electrically paced 1 Hz at 37°C. Data presented are mean±SEM (replicates are as indicated and pooled from 3+ independent differentiations). One-way ANOVA with Tukey's post hoc test; **p<0.01 and ***p <0.001 vs LMNA DCM. Data collected and analyzed by Shan Parikh (Unpublished).

DISCUSSION

Here, we describe a multigenerational pedigree in which individuals afflicted with familial DCM co-segregate with a frameshift mutation in exon 9 of *LMNA*. The proband and genotype positive family members show highly penetrant disease progression as evidenced by early death or heart transplant by the third decade of life. The initially phenotype negative mutation carrier later displayed atrial fibrillation in the absence of gross structural abnormalities on echocardiogram and absent fibrosis indicated by cardiovascular magnetic resonance, consistent with disease progression in the literature[127, 146]. Compared to males, female carriers of the c1526.dupA mutation resulting in the same frameshift mutation (T510Y) reportedly have a higher incidence of SCD death, however, the mechanism requires further investigation[137]. Furthermore, as the median age of conduction system disease and heart failure detection are 44 and 48 respectively[146], the early and rapid disease progression in patients with this mutation[136, 137] suggests a high degree of pathogenicity for this mutation. Overall, my findings are consistent with reported pathogenicity in previously described families and verify the pathogenicity of this variant[136, 137].

The increased genetic testing of patients with familial DCM and the subsequent detection of variants of unknown significance (VUS) in disease causing genes has created a newfound difficulty: is this variant pathogenic and how does this impact patient care? Development of a robust and fast method for assessing variant pathogenicity is lacking. The combination of gene editing and hiPSC-CM technology provides a unique opportunity to assess pathogenicity and identify mechanisms of disease. The increasing development of high-throughput tools for functional assessment could help fill the unmet need for an *in-vitro* platform for assessing variant pathogenicity. To develop a framework for in-vitro assessment of mutation pathogenicity we generated hiPSC-CM from patients with a pathogenic mutation in *LMNA* and applied molecular and functional assays to identify reliable experimental outcomes.

Using patient cells we generated hiPSC for differentiation into CM from both healthy population controls and a LMNA DCM patient. Molecular evaluation demonstrated significant reduction in lamin evidenced by reduced mRNA and protein expression. As the mutation found in the patient is on exon 9 of *LMNA*, both mutant forms of lamin A and C will contain an early stop codon and thus should result in equal reductions in expression of both lamins. Interestingly, the disproportionate reduction in lamin A compared to lamin C protein suggests a more complex regulation of lamin A/C expression. Is it possible that some degree of mutant lamin is produced and this preferentially results in an overall decrease in lamin A stability and subsequent proteosomal degradation? While this question remains unanswered, the hypothesis that some mutant protein is being generated can be further investigated using proteasome inhibitors[147]. Should proteasome inhibition uncover detection of mutant lamin, it could suggest a dominant-negative effect of the mutant lamin protein in a scenario in which it accumulates, as could occur during increased cardiac stress due mitochondrial impairment[148]. However, consistent with a reduction in lamin mRNA and protein in the absence of fragment detection on full length western blot, nonsense mediated decay of lamin A/C is likely the dominant mechanism observed.

Nuclear abnormalities were observed in patient heart samples (also observed in human hearts with the *LMNA* c.1526dupA mutation) as well as in heterologous expression systems of disease causing *LMNA* mutations[130, 142]. Prior investigation of nuclear morphology in *LMNA* mutation carrying hiPSC-CM cultured on stiff culture dish did not demonstrate baseline nuclear defects[119]. However, electrical field stimulation was sufficient to uncover severe nuclear blebbing and shape abnormalities in the presence of increased apoptosis[119]. Similarly, other cell types overexpressing mutant lamin[141, 142] show significant nuclear elongation and blebbing at baseline. Here, LMNA DCM hiPSC-CM were matured on Matrigel mattress for 5 days allowing for cellular shortening (likely increasing activation of mechanotransduction pathways). Using this method, patient derived hiPSC-CM show a higher percentage of hiPSC-CM nuclei with changes in nuclear shape compared to population control. Further detailed evaluation will be required to elucidate the temporal development of nuclear abnormalities and response to stress conditions.

Due to the severe contractile defects identified clinically, we assessed contractility of patient derived LMNA DCM hiPSC-CM. Although a prior study did not find contractile or calcium handling deficits in *LMNA* mutation carrying hiPSC-CMs, the studies were confounded by inadequate methodology (studies did not use hiPSC-CM which had cellular shortening capacity) [120]. With the advent of Matrigel mattress, hiPSC-CM can be cultured on substrate of physiological stiffness, which enables significant cellular maturation with cellular shortening (up to ~10%)[59]. Using this method in this work, LMNA DCM hiPSC-CM exhibited contractile dysfunction evidenced by impaired time to peak and baseline. Investigation of the underlying calcium handling showed delayed calcium-induced calcium release (delay in time to peak) in addition to delayed calcium extrusion. Interestingly, calcium extrusion via slow pathways (predominantly mitochondria) show reduced rates of calcium extrusion, which may be consistent with findings of mitochondrial dysfunction and ROS generation in *LMNA* mutation carrying cells[149, 150]. Although sarcomeric DCM is often characterized by reduced myofilament calcium sensitivity[151-153] associated with smaller peak calcium transients[115], LMNA DCM hiPSC-CM in this study exhibited peak calcium transients of similar amplitude suggesting that the impairments in contractility are mediated through other mechanisms[154]. Further studies assessing the impact of *LMNA* mutation on the myofilament are needed to answer the questions: do DCM-causing *LMNA* mutations cause early changes in myofilament calcium sensitivity, or is this secondary to other aspects of disease progression? Overall, the contractile and calcium handling deficits are evidence of early contractile dysfunction which provide proof of concept that LMNA cardiomyopathy related contractile dysfunction can be modeled using hiPSC-CM.

Due to the increasing burden of VUS there remains a need for robust screening platforms for evaluating variant pathogenicity[134]. Using the CardioExcyte96 platform, which uses impedance measurements of hiPSC-CM in monolayer as a correlate of cellular contractility[39], we compared LMNA DCM hiPSC-CM versus multiple population controls. LMNA DCM hiPSC-CM in monolayer also showed contractile deficits with progressive worsening as identified with serial measurements between days 30-50. As a major limitation to these studies include the use of population controls, CRISPR/Cas9 gene editing was utilized to correct the c.1526dupC mutation in the patient hiPSC. CRISPR/Cas9 corrected patient hiPSC (isogenic controls) showed restoration of mRNA and protein which was sufficient for rescue of the contractile deficits identified using the CardioExcyte96. However, not all measured parameters of the impedance waveform were successfully restored with the CRISPR/Cas9 gene editing highlighting the heterogeneity in the development of disease in hiPSC-CM monolayers. As serial measurements show a progressive worsening of impedance-based parameters at days 50, comparisons of isogenic controls at that time point may show greater differences between groups.

In summary, we demonstrate that hiPSC-CM generated from a patient with familial DCM and a *LMNA* mutation recapitulate cardiac contractile defects associated with LMNA DCM. Rescue of the cellular DCM phenotype by CRISPR/Cas9 correction of the *LMNA* mutation confirms its pathogenicity. Furthermore, the validation of a hiPSC disease line with isogenic controls creates a useful model for investigating mechanisms of LMNA cardiomyopathy pathogenesis. Lastly, we provide proof of principle for high-throughput investigation of contractile dysfunction for determining pathogenicity of DCM causing mutations in *LMNA* **(see graphical abstract Figure 23).**

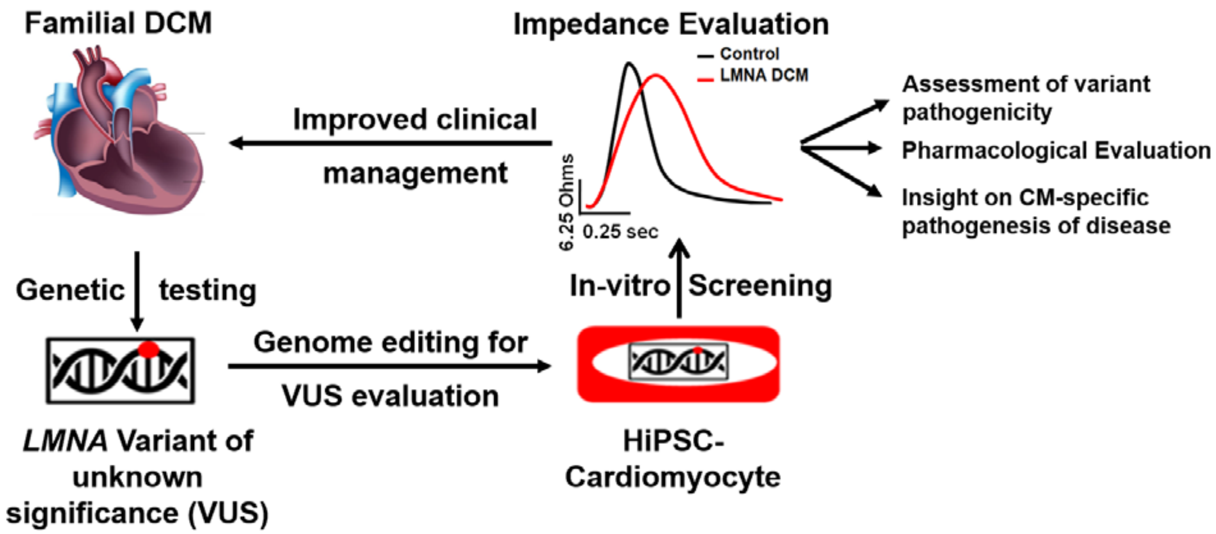

Figure 23: Graphical abstract depicting framework for functional evaluation of variants of unknown significance in *LMNA*. Patients identified to have familial DCM undergo clinical genetic testing. Identification of a disease causing mutation is ideal, however, the detection of a variant of unknown significance (VUS) remains problematic and limits clinical management of affected patient's relatives. Patient derived hiPSCs can be generated, or CRISPR/Cas9 can be employed for insertion of mutation into healthy control. HiPSC can be differentiated into hiPSC-CM and assessed *in-vitro* for contractile dysfunction using impedance based approaches. Variant pathogenicity can then be evaluated, pathogenesis of disease studied, and personalized pharmacological interrogation completed. Findings from *in-vitro* analyses can then be applied for improved clinical management of those afflicted with cardiac laminopathy.

CHAPTER 3

THYROID AND GLUCOCORTICOID HORMONES PROMOTE FUNCTIONAL T-TUBULE DEVELOPMENT IN HUMAN INDUCED PLURIPOTENT STEM CELL DERIVED CARDIOMYOCYTES

ABSTRACT

Rationale: Human induced pluripotent stem cell derived cardiomyocytes (hiPSC-CM) are increasingly being used for modeling heart disease and are under development for regeneration of the injured heart. However, incomplete structural and functional maturation of hiPSC-CM including lack of t-tubules, immature excitation-contraction (EC) coupling, and inefficient Ca^{2+}-induced Ca^{2+} release (CICR) remain major limitations.

Objective: Thyroid and glucocorticoid hormones are critical for heart maturation. We *hypothesized* that their addition to standard protocols would promote t-tubule development and mature EC coupling of hiPSC-CM when cultured on extracellular matrix with physiological stiffness (Matrigel mattress).

Methods and Results: HiPSC-CM were generated using the chemical differentiation method supplemented with triiodo-L-thyronine (T3) and/or dexamethasone (Dex) during days 16-30 followed by maturation for 5 days on Matrigel mattress. HiPSC-CM treated with T3+Dex, but not with either T3 or Dex alone initiated the development of a t-tubule network. Notably, Matrigel mattress was necessary for t-tubule formation. Compared to adult human ventricular CM, t-tubules in T3+Dex-treated hiPSC-CM were less organized and had more longitudinal elements. Confocal line scans demonstrated spatially and temporally uniform calcium release that is characteristic of ventricular-like EC coupling. T3+Dex enhanced elementary calcium release measured by calcium sparks as well as promoted ryanodine receptor (RyR2) structural organization. Simultaneous measurements of L-type calcium current and intracellular calcium release confirmed enhanced functional coupling between L-type calcium channels and RyR2 in T3+Dex cells.

Conclusions: Our results suggest a permissive role of combined thyroid and glucocorticoid hormones during the cardiac differentiation process which, when coupled with further maturation on Matrigel mattress, is sufficient for t-tubule development, enhanced CICR, and more ventricular-like EC coupling. This new hormone maturation method could advance the utility of hiPSC-CM for disease modeling and cell-based therapy.

INTRODUCTION

Human induced pluripotent stem cell derived cardiomyocytes (hiPSC-CM) are increasingly being used in biomedical research for cardiac disease modeling, cardiotoxicity screening, and regeneration of injured myocardium[17, 155]. Although considerable advances have been made in the maturation of hiPSC-CM[155], the lack of t-tubule formation and respective functional consequences remain a major limitation for their use[89, 103, 156, 157]. T-tubules are organized invaginations in the cardiomyocyte sarcolemma and are critical for the synchronous calcium induced calcium release (CICR) that underlies efficient excitation-contraction (EC) coupling in human ventricular myocardium. Reduced t-tubule formation contributes to abnormal EC coupling in heart failure and may be responsible for the ventricular arrhythmias observed after cardiac transplantation of hiPSC-CM[77]. Early t-tubule development in hiPSC-CM may be possible using complex techniques such as nano-patterning or tissue engineering, however, the extent of t-tubule formation and its functional contribution to EC coupling has not been well demonstrated[158, 159]. Due to the lagging advancement in this area, it is important to understand current maturation attempts and identify new avenues for further development of hiPSC-CM.

Most protocols for generating hiPSC-CM use 2-D culture systems in which cells are cultured on a stiff plastic substrate coated with diluted extracellular matrix. Conversely, the developing human CM is in a 3-D environment with constantly changing biophysical and chemical cues generated by a multitude of cell types. Transplantation of hiPSC-CM into the working myocardium of rodents has enabled structural and functional maturation of the hiPSC-CM, and although not feasible for generation of hiPSC-CM for other uses, it does provides proof of principle that hiPSC-CM can undergo maturation with appropriate environmental cues[76]. As such, recent efforts to enhance maturation have attempted to provide a more in-vivo like environment by recapitulating key biophysical and signaling cues present in the developing heart, with some success in hiPSC-CM maturation[88, 155, 160].

The stiffness of a substrate can be defined by a numerical constant known as Young's modulus. Rigid tissue culture polystyrene is estimated to be at a Young's modulus of ~1 gPA, whereas cells in the developing heart range from 5-40 kPA[88]. Studies using neonatal rat ventricular cardiomyocytes (NRVM) cultured on collagen coated polyacrylamide gels with an elastic modulus of 10 kPa, show significantly enhanced sarcomere alignment, greater force generation, and improved calcium kinetics, compared to cells cultured on substrates of higher stiffness (100 kPa), thus providing clear rationale for modulation of the culture substrate stiffness[161]. Similarly, investigators have manipulated the topography of the substrate by micro-printing synthetic substrates of physiological stiffness into various shapes such as squares or rectangles, showing that hiPSC-CM matured best on shapes with an aspect ratio of 7:1[158]. Another study found that hiPSC-CM matured optimally on microgrooves that were 8-30 µm in width and 850-1000 nm deep as evidenced by significant sarcomere alignment and sarcomere length of 1.8µm[162]. Additionally, the combined use of extracellular matrix (ECM) with a patterned underlying substrate further improves hiPSC-CM maturation, which was suggested to be dependent on the integrin and focal adhesion signaling resulting from the ECM-cell interaction[163]. As patterning is a difficult process requiring specialized materials and technical input, its widespread use and thus reproducibility is limited. Simpler methods have been developed which harness the maturation power of optimal substrate stiffness. The Matrigel mattress is one such simpler approach which relies on the use of Matrigel (composed of extracellular matrix proteins), which when partly polymerized, provides a substrate of physiological stiffness and results in hiPSC-CM with shortening capacity and electrophysiological maturation[59]. Although hiPSC-CM on Matrigel mattress demonstrated rod like morphology with shortening capacity and improved electrophysiological characteristics, the efficiency of CICR was not significantly improved using this approach. Based on these examples, substrate stiffness and topography are critical for maturation of the hiPSC-CM and should be considered for generation of more mature cells.

Addition of relevant signaling factors present during the development of the heart also help promote maturation. As such, multiple custom CM differentiation media have been developed ranging from addition of relevant hormones to alteration of the metabolic substrate. Two critical factors present in high levels during cardiac maturation in the developing heart include, although not limited to, Tri-ido-L-thryonine (T3) and glucocorticoids[164, 165].

The active form of the thyroid hormone, T3, is essential for development and when low/absent during gestation results in fetal cardiac malformations. Hypothyroidism in the human adult can result in significant cardiac dysfunction including both electrophysiological abnormalities and heart failure[166]. The actions of the thyroid hormone have been characterized as genomic (require gene expression) and non-genomic (direct action, e.g. on integrin signaling and membrane pumps)[164]. T3 canonically enters the cell and binds to a nuclear thyroid receptor (TR) which dimerizes with the retinoic acid receptor. This complex binds to the T3 response elements on the genome to modify gene expression. There are two TR, α and β, each of which have 2 isoforms. These are regulated in a tissue specific and developmental fashion. During development, there is a transition from TRα to TRβ in the human heart where TRα2 is the dominant isoform throughout development and the TRβ1 isoform predominates shortly have the T3 surge at brith[167]. In mice, the TRα receptor has been implicated as a molecular switch for cardiac maturation between fetal and postnatal life based on the hypothesis that the TRα isoform in the absence of T3 inhibits gene expression, and after the T3 surge at birth activate the TRα[168]. These findings suggest that this switch acts as a major determinant in the developmental process of the heart. Although TR receptors have not been thoroughly characterized in the hiPSC-CM, the rationale for adding T3 for maturation of the developing hiPSC-CM is well supported. As expected, supplementation of T3 to hiPSC-CM enhanced maturation as evidenced by improved calcium handling and electrophysiological characteristics[169]. Furthermore, commercial hiPSC-CM maturation media from Pluriomics now includes T3 and some protocols now recommend inclusion of T3 in differentiation media starting at day 21 of the differentiation protocol[52].

Glucocorticoids are also critical for structural and functional maturation of the heart, and in the human fetus the surge in glucocorticoids before birth mediates proper development of the heart[165, 170]. When glucocorticoid hormones bind to the glucocorticoid receptor (GR), the complex translocates to the nucleus where it acts as a transcriptional regulator. Current studies have focused on the role of the GR in the rodent heart using either NRVMs treated with glucocorticoids in *in-vitro,* or by using genetically modified mice which lack GR in the cardiomyocyte. Tissue specific knockout of the GR in mice resulted in myofilament disarray with mice dying from heart failure at 7 months of age[171]. Single cell analyses from isolated CM showed impaired SR function evidenced by reduced response to caffeine suggesting alteration in SR calcium stores. Loss of GR in both conditional and global KO mice demonstrate deficient ECC with severe reductions in RyR2, NCX, and SERCA2a expression[165, 170, 171]. Lastly, administration of synthetic glucocorticoids such as corticosterone or dexamethasone to isolated mouse CM promotes sarcomeric organization, improves contractility, and induces ECC related gene expression including transcripts for LTCC, RyR2, SERCA2a, and NCX[170].

Combinatorial approaches for maturation of hiPSC-CM have not been widely tested in the literature. With the clear benefit of T3 and glucocorticoids as well as the importance of biophysical cues, combination of these cues is a feasible route for synergistic effects on maturation. To date only one such report exists and does demonstrate a clear benefit. Combination of T3, dexamethasone, and insulin growth factor-1 showed both electrophysiological, metabolic, and structural maturation of hiPSC-CM, however excitation-contraction coupling was not thoroughly evaluated[172, 173]. Despite the incorporation of various maturation methods, current hiPSC-CM developed for single cell studies show characteristics of late stage human fetal cardiomyocytes at best and lack t-tubules[173].

Without additional maturation, hiPSC-CM generated with commonly used protocols remain spherical, without shortening capacity, and show impaired electrophysiological and calcium handling properties. With the introduction of both physical (patterning) and certain chemical cues, hiPSC-CM can be more elongated with aligned sarcomeres, display cell shortening with force generation capacity, display more rapid calcium kinetics, and more adult like electrophysiological properties. Nevertheless, current hiPSC-CM (both commercially available and academic) still lack structural maturation such as development of t-tubules and RyR2 organization such that they continue to demonstrate functional deficiencies including inefficient CICR, poor repolarization reserve, and lack of positive force frequency response. While we have an understanding of the deficiencies in calcium handling and electrophysiological properties of hiPSC-CM, the remaining question is what parameters are important for maturation of hiPSC-CM and can these be efficiently adopted to current protocols? One major structural deficit is the lack of t-tubules. As mechanistic understanding of t-tubule biogenesis is limited, the development of t-tubules in hiPSC-CM will both improve utility of hiPSC-CM as well as provide a tool for investigation of the molecular mechanisms responsible for t-tubule development.

In summary, the absence of t-tubules has remained a major concern for the use of hiPSC-

CM. Although several methods have been reported that improve hiPSC-CM maturation (eg, culture on soft, patterned substrates, increased length of culture time, and hormone maturation), none of them produce functional t-tubules. We similarly observed that Matrigel mattress alone or treatment with hormone alone is not sufficient for development of t-tubules. Thyroid and glucocorticoid hormones are critical for cardiac maturation during development in-vivo[164, 170]. While hiPSC-CM induction media contains both factors, supplementing the culture media with higher concentrations of thyroid and/or glucocorticoid was found to enhance CM maturation[169, 170, 172]. Independently, we and others have shown improved contractility and electrophysiological maturation when culturing hiPSC-CM on extracellular matrix substrates of physiological stiffness[59, 158]. Thus, we hypothesized that a combination of the thyroid hormone tri-iodo-l-thyronine (T3) and the glucocorticoid dexamethasone (Dex) with the flexible Matrigel substrate method[59] would further enhance the structural and functional maturation of hiPSC-CM. As such, at days 16-30 of the chemical differentiation protocol, the maintenance medium was supplemented with a combination of T3 and Dex. Cells were dissociated after day 30 and further matured on Matrigel mattress for an additional 5 days before experimental analyses. Our findings provide compelling evidence that combined activation of pathways downstream the thyroid and glucocorticoid receptors is sufficient for the initiation of functional t-tubule development if hiPSC-CM are allowed to mature on a substrate of extracellular matrix with physiological stiffness. Furthermore, T3+Dex-treated cells demonstrated widespread cellular distribution of key t-tubule–related proteins and displayed improved RyR2 localization at the z-line. Hence, our discovery not only helps to overcome a major barrier in the field but also provides novel mechanistic insight into the genesis of t-tubules.

MATERIALS AND METHODS

HiPSC Culture and Maintenance: Human induced pluripotent stem cells (hiPSC) were generated using fibroblasts isolated from dermal punch biopsies. These cells were acquired from two consenting healthy individuals (one male, one female) and reprogrammed to hiPSC using a non-integrating episomal based reprogramming approach. In brief, Epi5™ episomal oriP/EBNA1 vectors (Thermo) containing 5 reprograming factors (Oct4, Sox2, Lin28, Klf4, and L-Myc) were electroporated into fibroblasts using the Thermo NEON® Transfection System as per manufacturer's guidelines. Single colonies were manually picked and clonally expanded. Clones were subjected to a battery of analyses for verification of stemness and genomic stability including karyotyping, embryoid body differentiation, and immunostaining (Tra1-60, SSEA4, SSEA5, and Oct4)[39]. HiPSCs were maintained on growth factor reduced Matrigel (Corning) coated plates in mTeSR1 medium (Stem Cell Technologies). Plates were coated with 1:200 Matrigel diluted in DMEM/F12 for at least 1 hour at 37 °C prior to use. HiPSC were passaged every four days. Cells were washed with 1xPBS without CaCl2 or MgCl2 and dissociated with 0.5 mmol/L EDTA in PBS without calcium or magnesium for 7 minutes at room temperature (RT) followed by resuspension in mTeSR1 with 10 μmol/L RHO kinase inhibitor Y-27632 (Calbiochem) and immediately seeded on Matrigel coated plates. Cells received fresh mTeSR1 daily and were maintained at 37 °C with 5% CO2. The male hiPSC line was used as the primary source of cardiomyocytes (CM) for imaging and functional studies. The female hiPSC line was used to confirm the concordant effect of the hormone treatment on CM morphology.

Differentiation and maturation of hiPSC to cardiomyocytes: HiPSC-cardiomyocytes (hiPSC-CM) were generated using a small molecule based cardiac differentiation protocol[51, 52, 174].

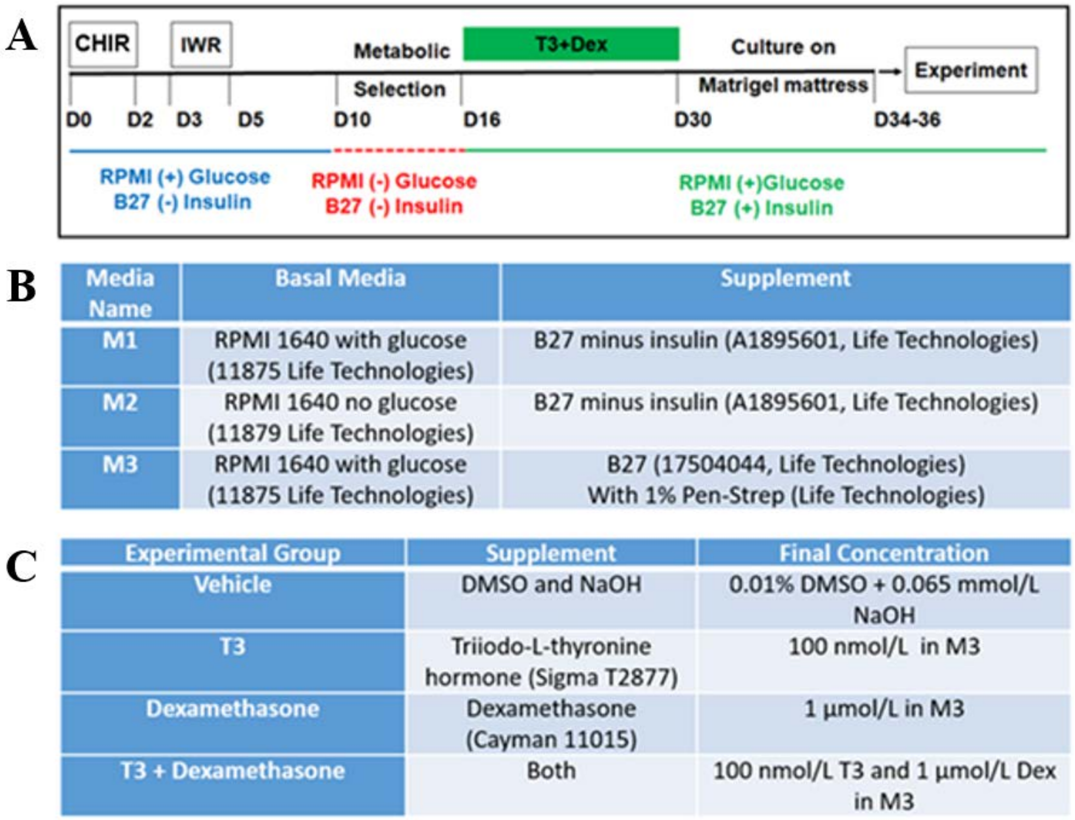

Media Name	Basal Media	Supplement
M1	RPMI 1640 with glucose (11875 Life Technologies)	B27 minus insulin (A1895601, Life Technologies)
M2	RPMI 1640 no glucose (11879 Life Technologies)	B27 minus insulin (A1895601, Life Technologies)
M3	RPMI 1640 with glucose (11875 Life Technologies)	B27 (17504044, Life Technologies) With 1% Pen-Strep (Life Technologies)

Experimental Group	Supplement	Final Concentration
Vehicle	DMSO and NaOH	0.01% DMSO + 0.065 mmol/L NaOH
T3	Triiodo-L-thyronine hormone (Sigma T2877)	100 nmol/L in M3
Dexamethasone	Dexamethasone (Cayman 11015)	1 µmol/L in M3
T3 + Dexamethasone	Both	100 nmol/L T3 and 1 µmol/L Dex in M3

Figure 24: **Flowchart for generation of hormone treated hiPSC-CM. A)** hiPSC begin the chemical differentiation method at D0 at which point with 6 µmol/L GSK3 inhibitor CHIR99021 is added in fresh mTeSR1. On day 2, the media was changed to fresh M1 media. On day 3, the media were changed to M1 with 5 µmol/L IWR-1. On days 5 to 9 the media were changed every other day with M1. Metabolic selection was started with M2 media on day 10 and cells received fresh M2 media on days 12 and 14. Starting at D16 cells receive M3 media with T3+Dex or vehicle supplementation every other day until D30 at which point they were cultured on the Matrigel mattress. After culturing cells on Matrigel mattress for 4-6 days, they underwent evaluation. **B)** Composition of media used during chemical differentiation. **C)** Composition of media supplementation for hormone treatment.

HiPSCs were cultured until they reached 65-85% confluence, at which point the chemical differentiation protocol was initiated (D0) as described in **Figure 24A**. At D0 the hiPSC transition from mTeSR1 to M1 was supplemented with 6 µmol/L GSK3 inhibitor CHIR99021 (Selleck Chemicals). On day 2, the media was changed to fresh M1. On day 3, the media were changed to M1 with 5 µmol/L IWR-1 (Sigma). On days 5 to 9 the media were changed every other day with M1. Metabolic selection was started with M2 media on day 10 and cells received fresh M2 media on days 12 and 14. On day 16, cells were transitioned to 3 mL M3 media. For generation of hormone treated cells, M3 was supplemented with the combination of hormones or their vehicles as listed in **Figure 24B**. All solutions were generated, stored at -20 °C, and used within 3 months of constitution. Media supplemented with the final concentrations of hormones was prepared fresh daily (**Figure 24C**).

hiPSC-CM Dissociation and Plating on Matrigel Mattress: At D30 of the chemical differentiation process, hiPSC-CM were dissociated and plated as previously described[59, 82]. Primarily, freshly differentiated cells were utilized for experiments. Freshly differentiated hiPSC-CM were washed with 1x DPBS without calcium and magnesium and then incubated in 1 mL of TrypLE Express (Life Technologies) for 10 minutes at 37 ºC. A 10 mL serological pipet was then used to add equal volumes of M3 to neutralize TrypLE and for resuspension. Cells were centrifuged at 200 x g for 5 minutes, re-suspended in 1-3 mL of M3, and filtered through a 40 µM filter (Falcon). The filtered cells were counted and seeded on Matrigel mattress as previously described[59, 124, 135]. Cells were allowed to attach for at least 10 minutes at RT before adding an additional 1 mL of normal M3 media and returned to the incubator for experimental use at days 4-6. M3 media was refreshed on a daily basis until experimentation.

Cell Selection for Imaging and Functional Measurements: The Matrigel mattress method generates single, elongated CM located in a glass bottom culture dish that can be used for imaging, calcium fluorescence, and patch-clamp studies without the need for cell transfer[59]. Since not all hiPSC-CM achieve a rod shape on mattress, hiPSC-CM were selected for experimental studies using the same morphological and functional selection criteria that are widely used in studies of CM acutely-isolated from adult hearts: (1) rod-shape, (2) no contact with other cells, and (3) robust contractile response to field stimulation (for calcium current and patch-clamp studies). In all cases, the experimenter that selected cells for studies was blinded to the treatment group.

T- Tubule Staining and Analysis: HiPSC-CM were seeded at a density of 10-15,000 cells on Delta TPG Culture Dish (Fisher) using the Matrigel-mattress. Cells were loaded (as per manufacture's recommendations) with CellMask Orange for 20 minutes followed by three 5 minute washes at RT in Tyrode's solution consisting of (mmol/L): 140 NaCl, 5 KCl, 1 $MgCl_2$, 1.8 $CaCl_2$, 10 glucose, and 10 HEPES (pH = 7.4). Images were collected as Z-stacks using a Zeiss LSM510 inverted laser scanning confocal microscope. Images were first deconvolved, and thresholded to the mean fluorescence intensity of the entire cell, and t-tubule density calculated by normalizing the supra-threshold signal within the cell interior to cross-sectional cell area[175]. Cross sectional area was determined using ImageJ. Presented t-tubule densities correspond to images taken within the central plane of the cell. 3D reconstruction of the t-tubular network was performed as described previously[175]. For rendering of the surface sarcolemma, the membrane was identified manually across entire Z-stacks using ImageJ, and smoothed by dilation and re-erosion. Sarcolemma Z-stacks were then merged with the t-tubule stacks and rendered in 3D.

T-tubule development in hiPSC-CMs was compared with t-tubule density and organization in the left ventricles and right atria of healthy individuals. This tissue was obtained using protocols approved by Norwegian South-Eastern Regional Committee for Medical Research Ethics (Permit numbers s-07482a and 2010/2226), in agreement with guidelines outlined in the Declaration of Helsinki. Tissue from the left ventricular free wall was obtained from non-diseased hearts considered for transplantation, but deemed unsuitable due to surgical reasons (n= 4). These hearts were kept in a cardioplegic solution at 4 °C for 1-4 hours prior to tissue collection and freezing. Cause of death in these patients was cerebrovascular accident, and none had a history of heart disease. Approval for study inclusion was obtained from next of kin.

Tissue from the right atrial appendage was obtained during open-heart surgery in patients undergoing coronary artery bypass surgery. Atrial tissue was rapidly excised and frozen in liquid nitrogen until further use[176]. All patients (n= 3) provided informed written consent.

Using a cryostat, human tissue was sliced into 10 µm thick sections at -20 °C, collected on Poly-prep Slides (Sigma-Aldrich, St. Louis, MO), and fixed in 4% paraformaldehyde. T-tubules were stained with wheat germ agglutinin (WGA) conjugated to Alexa Fluor 480 prepared in PBS. An LSM 710 (Zeiss, GmbH, Jena, Germany) confocal scanning system with a 40× objective was used to visualize t-tubules and cellular membranes. T-tubule density was analyzed as described above for hiPSC-CMs. Organization of t-tubules was compared by calculating the amount of transverse and longitudinal elements in the representative 3D cells.

Paced Calcium Transients: HiPSC-CM were incubated for 30 min at RT in 5 µM Fluo-4 AM (Invitrogen) with 0.02% pluronic (Invitrogen) followed by three 5-minute washes in Tyrode's solution consisting of (mmol/L): 140 NaCl, 5 KCl, 1 $MgCl_2$, 1.8 $CaCl_2$, 10 glucose, and 10 HEPES (pH = 7.4). Single-cell calcium transients were recorded at RT using a Zeiss LSM 510 inverted laser scanning confocal microscope in line scan mode (521 lines per second) with a 40X / 1.30 NA planar oil immersion objective. The pinhole settings corresponded to a measured optical slice of 0.85 µm. HiPSC-CM were stimulated by an electric field of 40 mV with a 5 ms bipolar pulse duration at 0.2 Hz using a MyoPacer (IonOptix). The focal plane was positioned in the middle of the Z-dimension from the top and bottom edges of the cell and transverse lines were drawn across the widest part of the cell, avoiding nuclei. Fluo-4 was excited at 488 nm with an argon laser and the emission was passed through a 505 nm long pass filter to photomultiplier tube detectors. Images were normalized to the intrinsic background fluorescence and ImageJ was used to measure the calcium transient amplitude and rate based parameters at the peripheral and central regions of the cell. Time-zero for time to peak measurements were defined as the point of calcium rise.

Immunostaining: HiPSC-CM were cultured on Matrigel mattress-coated cell culture chambers (Falcon 354104) and fixed with 4% paraformaldehyde (Thermo #28906) for 10 minutes at RT. Cells were washed three times with PBS for 10 minutes at RT and permeabilized with 0.4% Triton X-100 in PBS for 1 hour, after which they were blocked for 1 hour (5% Goat serum, 0.4% Triton X-100 in PBS). Cells were incubated with primary antibody overnight at 4 ºC as indicated in **Table 6**. Then cells were washed 3 x 5 minutes with 0.4% Triton X-100 in PBS and incubated with secondary antibody for 1 hour. After washing cells with 0.4% Triton X-100 in PBS 3 x 5 minutes followed by PBS another 3 x 5 minutes each, the cells were counterstained with ProLong Diamond Antifade with DAPI-containing Mountant (Invitrogen #P36962) and mounted on a cover slide for imaging. Imaging of t-tubule markers was completed using the Zeiss LSM 510 followed by calculation of percent stained area using ImageJ. For co-labeling of t-tubule markers and α-actinin, imaging was performed using the LSM 880 inverted laser scanning confocal microscope with a

63X / 1.40 Plan-APOCHROMAT oil immersion objective. Each channel was sequentially scanned using photomultiplier tube detectors. Alexa Fluor 488 was excited using a 488 nm Argon laser and the emitted light was collected from 499 – 570 nm; Alexa Fluor 568 was excited using a diode-pumped solid state 561-10 laser and collected from 570 – 712 nm; DAPI was excited using a 405-30 diode laser and collected from 409 – 497 nm. Using ImageJ, immunostaining images were background corrected by subtracting the mean value of background next to the cell and the contrast was linearly adjusted. Each image from a particular immunostain (e.g. BIN-1) was adjusted equally and all images were cropped and scaled equally. Regularity of RyR2, Cav3, BIN1, α-actinin and JP2 localization along z-lines was assessed using fast Fourier transforms (FFT), computed by the FFT tool in Matlab (MathWorks). The power spectrum was plotted as a function of 1 / axial spatial frequency, and the amplitude of the first peak measured. Co-localization analysis was then completed using the Manders split coefficients in ImageJ.

Table 6: Antibodies for Immunostaining

Antibody	Manufacturer	Host	Catalogue number	Concentration
Bin1	Abcam	Rabbit	Ab185950	1:100
Cav3	Abcam	Rabbit	Ab2912	1:100
Sarcomeric α- actinin	Sigma	Mouse	A7811	1:100
Sarcomeric α- actinin	Abcam	Rabbit	Ab137346	1:100
Junctophillin2	Abcam	Mouse	Ab180362	1:100
RyR2	Thermo	Mouse	MA3-916	1:50
anti-mouse 488	Invitrogen	Goat	A11029	1:250
anti-rabbit 568	Invitrogen	Donkey	A10042	1:250

Sparks Measurements in Permeabilized Myocytes: Isolated hiPSC-CM were permeabilized with saponin (20 µg/mL) for 30 seconds and then bathed for 5 minutes in a freshly-made internal solution (pH = 7.2) containing (mmol/L): K-aspartate (120), KCl (15), K_2HPO_4 (5), $MgCl_2$ (5.6), HEPES (10), dextran (4% w/v), MgATP (5), Phosphocreatine-Na_2 (10), creatine phosphokinase (10 U/mL), reduced L-glutathione (10), EGTA (0.5), $CaCl_2$ (0.12), and Fluo-4 pentapotassium salt (0.03). Free [calcium] was 100 nmol/L (calculated with MaxChelator). Confocal imaging was performed on a Zeiss LSM 510 inverted laser scanning confocal microscope equipped with a 40X / 1.30 NA planar oil immersion objective. Fluo-4 was excited by an argon laser line at 488 nm and the fluorescence emission was passed through a 505 nm long pass filter to PMT detectors. Cell sparks were imaged in line-scan mode in isolated cells that had no contact with other cells. Lines were positioned longitudinally near the center of the cell. SR calcium load was measured as the calcium transient amplitude induced by application of 10 mmol/L caffeine. Image analysis was performed in ImageJ with the SparkMaster plugin using a background setting of 5 and criteria of 3.8[177]. Spark mass was calculated from the equation: spark mass = 1.206 * Amplitude * FWHM^3.

Measurement of Intracellular Calcium and Contractility: HiPSC-CM were seeded 10-15,000 cells on Matrigel mattress on Delta TPG Culture Dish (Fisher). After 5 days on mattress with daily M3 media changes, cells were loaded with Fura-2 AM (Molecular Probes Inc, Eugene, OR) as previously described[59, 82]. Fura-2 AM was reconstituted in DMSO at 2 mmol/L in a light-protected vessel. HiPSC-CM were incubated at a final concentration of 2 µmol/L Fura-2 AM in M3 medium for 8 minutes at RT and then washed twice with 1.2 mmol/L calcium containing Tyrode's solution with 250 µmol/L probenecid. Measurements were made with a 40x LUCPlanFLN Ph2 (WD 2.7-4 mm) objective using a Olympus microscope fitted with an IonOptix video microscopy system (Ionoptix, Milton, MA). Tyrode's solution contained in mmol/L: $CaCl_2$ as indicated below, NaCl 134, KCl 5.4, $MgCl_2$ 1, glucose 10, and HEPES 10, with the pH adjusted to 7.4 with NaOH.

Calcium Kinetics: Calcium transients were recorded from cells which elicited a response during 0.2 Hz electrical field stimulation in Tyrode's solution with 2 mmol/L calcium (2Cal) for 20 seconds at RT. Stimulation was then stopped and immediate puffer based application of 10 mmol/L caffeine in 2Cal for 5 seconds was initiated followed by 5 seconds of recording with 2Cal alone to assess for sarcoplasmic reticulum (SR) calcium content and SERCA-independent calcium extrusion. The recording was then paused for 1 minute while cells were continuously perfused with 2Cal solution. Cells were then exposed to 0 mmol/L Na 0 mmol/L calcium solution (0Na0Ca) for 10 seconds followed by puffer-based application of 10 mmol/L caffeine containing 0Na0Ca solution for 30 seconds in addition to 10 seconds of recording in 0Na0Ca solution to estimate non-NCX mediated calcium extrusion. For examination of SR calcium contribution to the calcium flux, hiPSC-CM were pretreated for 5 minutes with 10 µmol/L thapsigargin (Sigma) and 50 µmol/L ryanodine (Sigma) in 2Cal after the last wash. For each cell, the following parameters were determined: baseline and peak amplitude of transient, time to peak and baseline, and tau (τ) of A) field stimulated calcium transients, B) 2Cal Caffeine transient, and C) 0Na0Ca Caffeine transient. Analyses of calcium transients and calculation of calcium flux balance was completed as previously[82]. Time zero for time to peak measurements were defined as the time of electrical stimulation.

Contractility: Video based edge detection was used to simultaneously assess cellular shortening of the hiPSC-CM during the first 20 seconds of field stimulation. In brief, during acquisition of calcium transients on single HiPSC-CM, edge detectors were placed to define the ends of the cells using IonWizard™ v6.5 acquisition software (Ionoptix, Milton, MA).

Analysis of traces was completed using the instrument packaged IonWizard™ v6.5 data analysis software. Cell selection was limited to cells which were amenable to 0.2 Hz field stimulation and captured by edge detection.

Morphometric Measurements: HiPSC-CM were seeded on Matrigel mattress. Cellular volume measurements were taken as previously described[59, 82]. Briefly, Z-stacks of single D35 hiPSC-CM were obtained using a Zeiss LSM 510 inverted laser scanning confocal (40x oil immersion 1.30 Plan-NEOFLUAR lens). HiPSC-CM were loaded with 5 µmol/L calcein AM (Molecular Probes, Eugene, OR) in Tyrode's solution for 30 minutes at RT followed by three five-minute washes at RT to remove any residual extracellular dye. Calcein AM was exited at 488 nm with an argon laser. Z-stack images were collected in 0.44 µm intervals and reconstructed using IMARIS (Bitplane, South Windsor, CT) to allow for the measurement of volume and surface area. Manual measurements for length and width were completed using ImageJ measurement tools. Image acquisition and analysis was completed with the user blinded to the treatment groups.

Measurement of excitation contraction coupling (ECC) gain and L-type calcium current inactivation: To measure ECC gain, hiPSC-CM from both groups (30 days after cardiac induction, 3-5 days after plating) were studied using patch clamp technique in whole-cell mode. External solution contained (in mmol/L): NaCl 134, CsCl 5, $MgCl_2$ 1, $CaCl_2$ 2, glucose 10, HEPES 10, adjusted to pH 7.4 with NaOH. The pipette solution contained (in mmol/L): CsCl 110, $MgCl_2$ 1, MgATP 5, cAMP 0.2; EGTA 1; HEPES 20; adjusted to pH = 7.25 with CsOH. For calcium fluorescence measurements, 100 µmol/L Fluo-4 pentapotassium salt was added to the pipette solution. Currents were elicited by 50 ms depolarizing steps ranging from -40 mV to +40 mV (in 10 mV increments), from the holding potential of -70 mV. A 10 ms conditioning pulse to -45 mV was applied prior to the test pulse in order to inactivate Na^+ currents. To assess inactivation kinetics of ICa^{2+}, a single 500 ms depolarizing step to 0 mV (from the holding potential of -70 mV, with 10 ms conditioning pulse to -45 mV) was applied. Inactivation of ICa^{2+} was fit with a double exponential curve. All experiments were carried out at room temperature (RT).

Statistics: GraphPad Prism v7 was utilized for testing statistical differences with Student’s t-tests or, when applicable, ANOVA followed by post hoc analysis. P-values of < 0.05 were considered statistically significant. All data are presented as mean ± SEM. Image acquisition and analyses were conducted in a blinded fashion.

RESULTS

T3+Dex promotes t-tubule formation

HiPSC-CM were stained using a lipophilic membrane dye and imaged using a confocal microscope. Images were deconvolved, and thresholded to the mean fluorescence intensity of the entire cell, and t-tubule density calculated by normalizing the supra-threshold signal within the cell interior to cross-sectional cell area[175]. Consistent with previous reports, vehicle treated cells essentially lacked t-tubules **(Figure 25A).** Treatment with either T3 or Dex alone did not significantly impact t-tubule density, whereas the combination of T3+Dex promoted t-tubule formation **(Figure 25B)**. Notably, maturation on Matrigel mattress was required for t-tubule formation, as T3+Dex treated cells plated without thick Matrigel mattress were not different from control cells **(Figure 25E)**.

We next compared t-tubule density of hiPSC-CM to that of adult human myocardium **(Figure 25C, D)**. Ventricular tissue was acquired from organ donors deemed unsuitable for transplantation due to surgical reasons, and right atrial tissue from patients undergoing open heart surgery. T-tubule density was calculated from confocal images of cell-membrane stained cryosections (**Figure 25E**). T-tubule density of T3+Dex hiPSC-CM significantly exceeded that of healthy human atrial CM ($p< 0.05$), but remained sparser and less organized than the t-tubule network of human ventricular CM ($p< 0.001$) **(Figure 25E)**.

Adult human ventricular CM exhibited a greater fraction of transversely-oriented tubules in comparison to longitudinal elements, while T3+Dex cells exhibited similar proportions of t-tubules in these two orientations (**Figure 26A, B ,C**). This less organized appearance of t-tubules is analogous to that previously reported for rat CM during the postnatal period of development[178].

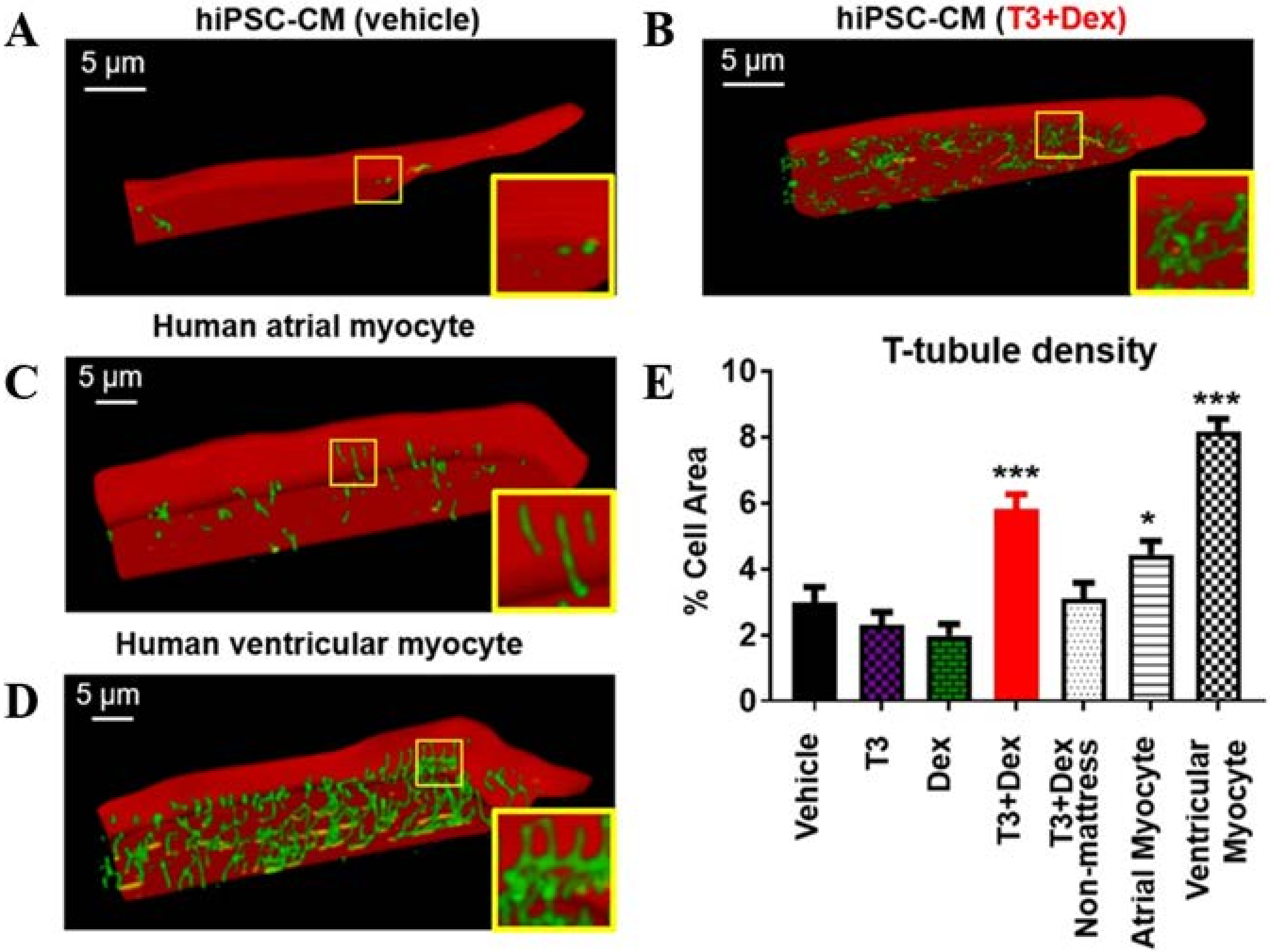

Figure 25: T3+Dex promotes t-tubule formation. Representative examples of t-tubule staining in hiPSC-CM (upper panels **A, B**) and human adult myocardium (lower panels **C, D**) with quantitation of t-tubule index (% cell area **E**) (n = 19-59 cells/group, *p < 0.05 and ***p < 0.001 vs vehicle). Images are planar projections of 3D reconstructions. All data are reported as mean ± SEM.

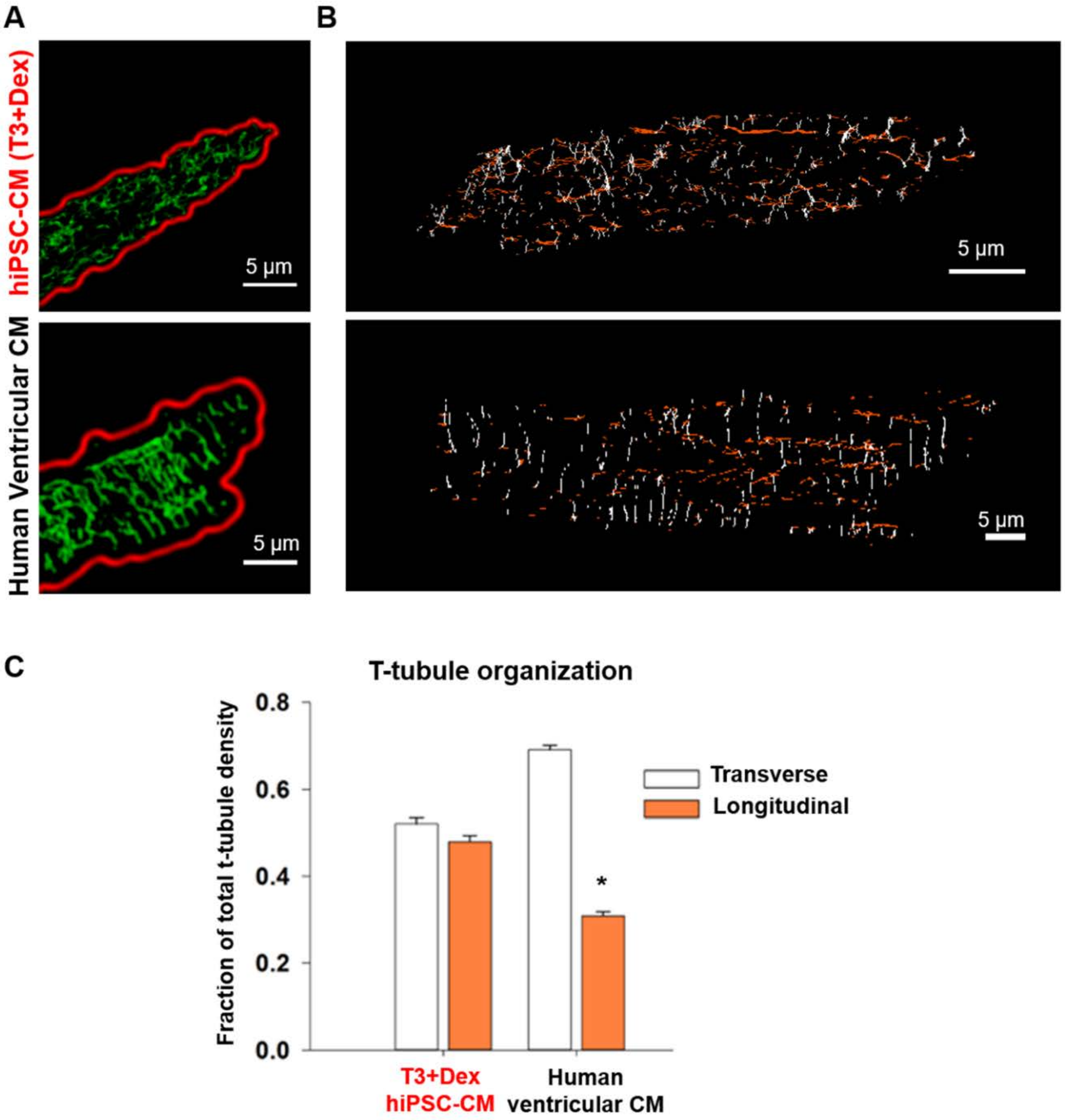

Figure 26: T-tubule organization: comparison of longitudinal vs transverse t-tubules. A) Representative examples of planar projection after 3D reconstruction of t-tubules in T3+Dex vs human ventricular myocardium demonstrate intracellular location of t-tubule membrane structures. **B)** Comparison of longitudinal vs transverse t-tubules in 3D reconstructed T3+Dex CM vs human ventricular CM, (white represents transverse t-tubules, red represents longitudinal t-tubules) **C)** Summary data showing the fraction of transverse vs longitudinal t-tubule of total t-tubule density. Data are mean ± SEM (n = 18-19 cells). Unpaired, two tailed Student's t-test: *p < 0.05 vs transverse. Data collected in collaboration with Dr. Michael Frisk and Dr. William Louch. Data adapted from[124].

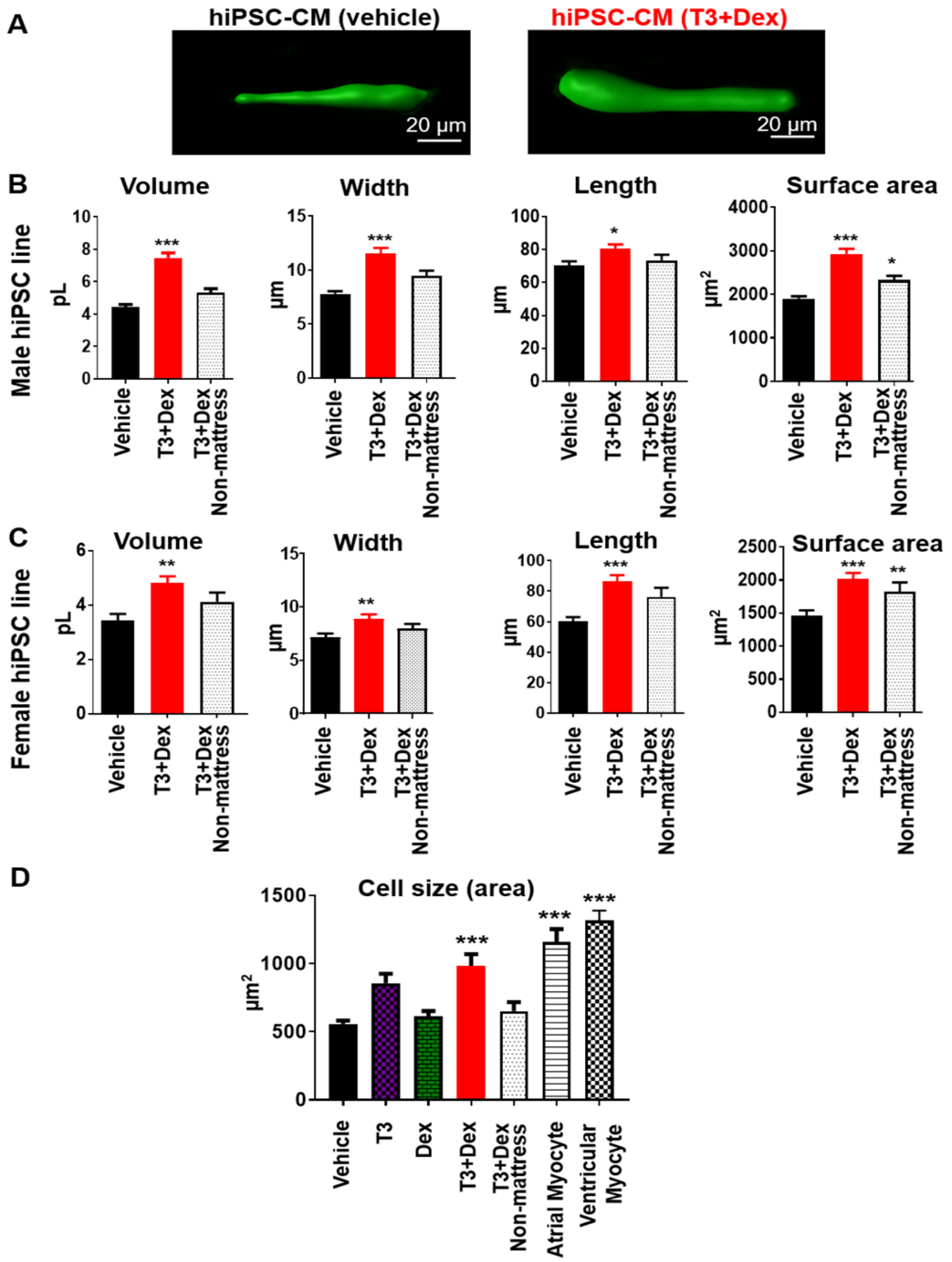

Figure 27: T3+Dex treated cells exhibit increased cell size. A) Representative examples T3+Dex vs control treated hiPSC-CM. Images are planar projections of 3D reconstructions using Calcein-AM. **B) and C)** Summary data: morphometric measurements obtained from hiPSC-CM derived from two independently-generated hiPSC lines (male and female). Data reported as mean ± SEM (n = 51-108 for male line from 4 independent differentiations and 24-35 for female line). **D**. Summary data for cross sectional cell area used for calculating t-tubule density for indicated groups. Note atrial and ventricular are of human origin (n = 19-59). One-way ANOVA with Tukey's post hoc test: *p < 0.05, **p < 0.01, and ***p < 0.001 vs vehicle. Data collected in collaboration with Dr. Daniel Blackwell. Adapted from[124].

T3+Dex treatment increases cellular size

In addition to promoting t-tubule development, T3+Dex also significantly increased the size of hiPSC-CM, primarily cell width and cell volume **(Figure 27A, B)**. Results were confirmed in a second, independently- generated hiPSC line (**Figure 27C)**. However, T3+Dex treated hiPSC-CM were still significantly smaller than adult human atrial or ventricular CM (**Figure 27D**).

T3+Dex treated cells exhibit increased subcellular distribution of t-tubule related proteins

Cellular staining for bridging-integrator 1 (BIN1), junctophilin-2 (JP2), and caveolin-3 (Cav3), three regulators of t-tubule genesis[94, 178], demonstrated striking changes in their subcellular localization. Whereas these t-tubule markers were located mostly perinuclear in vehicle-treated cells, after T3+Dex treatment staining was much more prominent throughout the whole cell **(Figure 28A)**. Note, hiPSC-CM not cultured on Matrigel mattress demonstrate minimal to no expression of Bin1 and Cav-3[89]. Importantly, co-immunostaining of sarcomeric α-actinin with JP2, which is required for anchoring and maturation of developing t-tubules[178], demonstrated increased accumulation of JP2 along Z-lines **(Figure 28B, C)**.

T3+Dex synchronizes intracellular calcium release

Are the newly formed t-tubules functional and do they contribute to EC coupling? The juxtaposition of the L-type calcium channel (LTCC) located in the t-tubule membrane with the ryanodine receptor (RyR2) located in the junctional sarcoplasmic reticulum (SR) would be expected to synchronize SR calcium release throughout the cell. Consistent with their lack of t-tubules[89], transverse confocal line-scans of Fluo-4 loaded vehicle treated hiPSC-CM

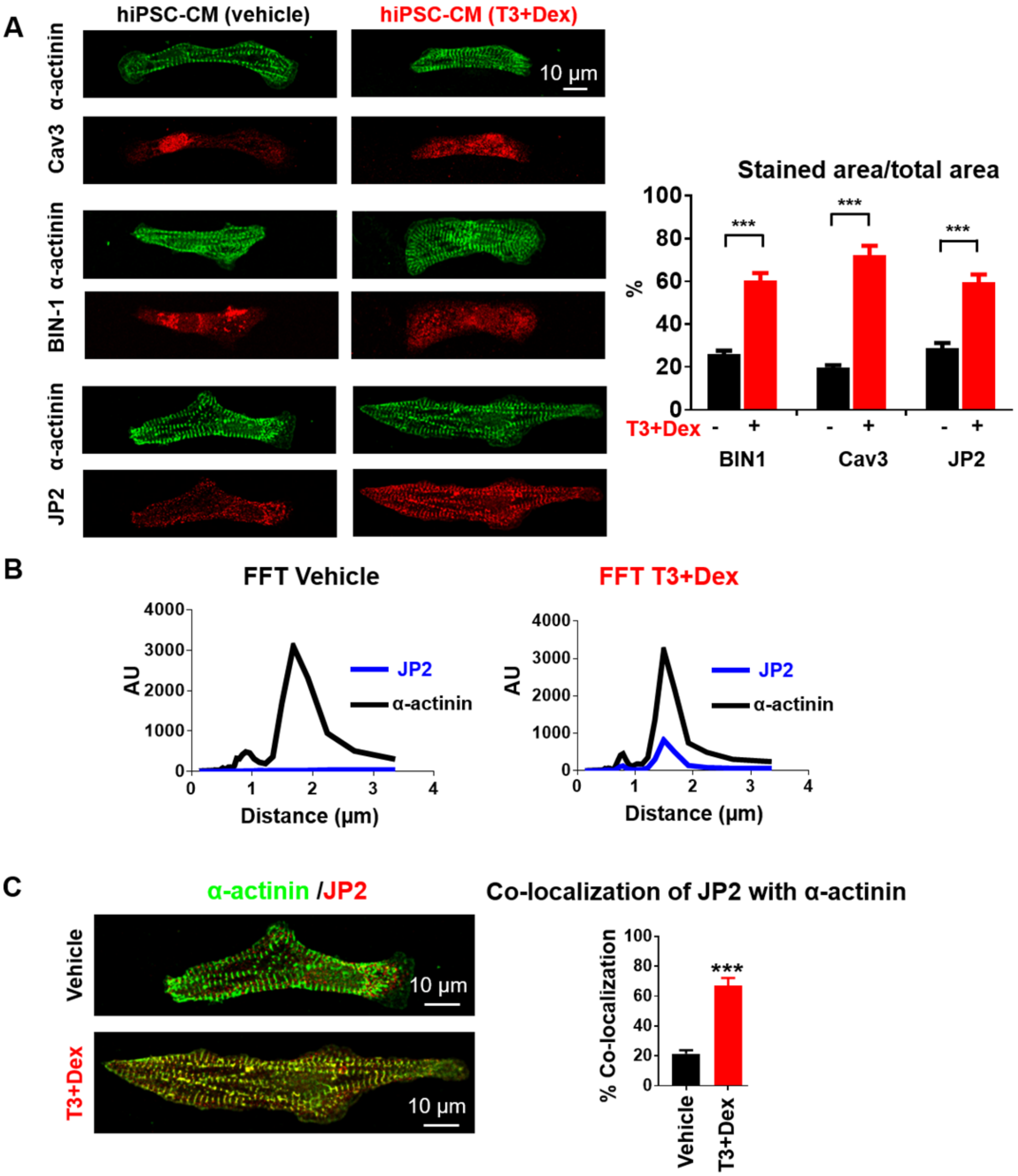

Figure 28: T3+Dex treated cells exhibit increased subcellular distribution of t-tubule related proteins. A) Representative cell images after co-labeling for α-actinin and the indicated t-tubule related proteins Cav3, BIN1, or JP2 in vehicle and T3+Dex treated cells (scale bar = 10 μm for all cells). Summary data show percent stained area of indicated protein of total cell area. Data reported as mean ± SEM (n = 17-23 cells). **B)** Fast Fourier transform for JP2 and α-actinin in vehicle and T3+Dex treated cells. **C)** Representative merge of α-actinin and JP2 with percent co-localization of JP2 with α-actinin (n = 5 cells/group). Unpaired, two tailed Student's t-test: ***p < 0.001. Data collected in collaboration with Dr. Daniel Blackwell, Dr. Nieves Gomez-Hurtado, Dr. Lili Wang and Dr. Michael Frisk, and Dr. William Louch. Adapted from[124].

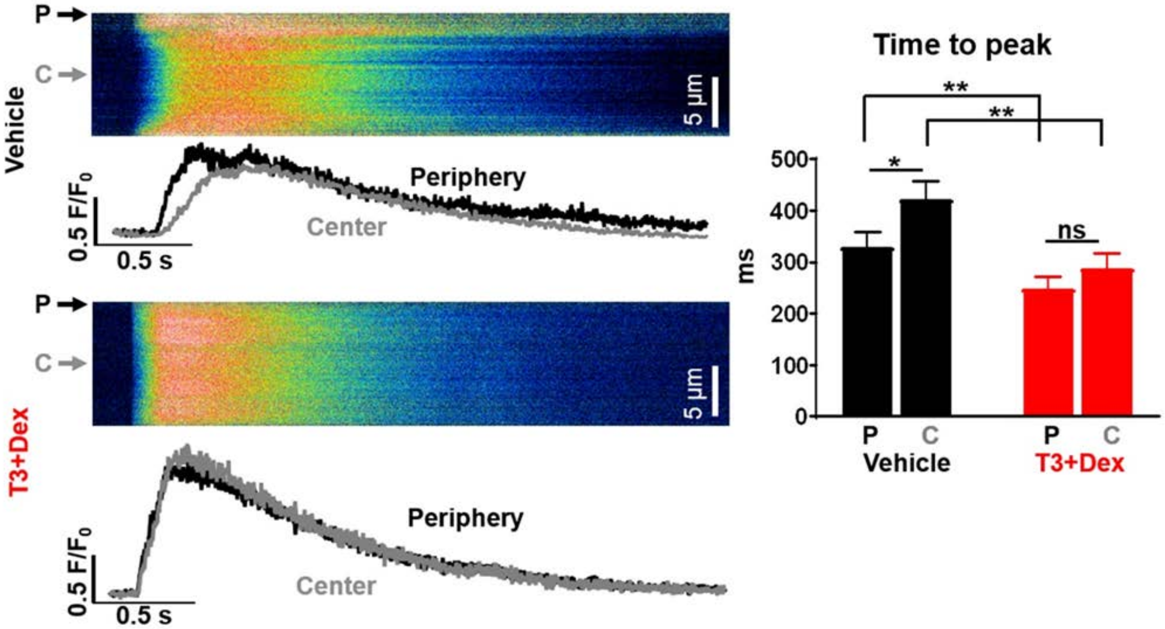

Figure 29: T3+Dex synchronizes intracellular calcium release. Representative transverse line scans of Fluo-4AM loaded hiPSC-CM electrically-stimulated at 0.2 Hz (**left panels**) and summary data (**right panel**) comparing calcium transient time to peak between periphery (P) and center (C) of cell. Scan line was positioned across the middle of each cell. N = 18-21 cells/group; *p < 0.05, **p < 0.01, ***p < 0.001, vs vehicle, ns – non significant. All data are reported as mean ± SEM. Data collected in collaboration with Dr. Daniel Blackwell. Adapted from[124].

demonstrated a U-shaped calcium release, with significantly faster calcium release at the cell periphery compared to the cell center (**Figure 29, Upper panel)**. In contrast, T3+Dex treated cells exhibited a uniform calcium release across the width of the cell, with a comparable amplitude and rate of calcium rise at both center and periphery of the cell **(Figure 29, lower panel)**. Together, our findings indicate functional t-tubule development in hiPSC-CM as evidenced by increased t-tubule staining, synchronization of calcium release, and improved subcellular distribution of t-tubule related proteins.

T3+Dex treated hiPSC-CM demonstrate greater dependence on SR calcium release for EC coupling

We next examined the effect of the hormone treatment on cellular calcium handling using the ratiometric Ca^{2+} indicator Fura-2 AM in electrically stimulated hiPSC-CMs **(Figure 30A)**[59]. Although diastolic and peak Fura-2 fluorescence were not significantly different between the groups, both time to peak and calcium decay rates were significantly accelerated by hormone treatment (**Figure 30B, C, D and Table 7).** To determine what was responsible for the accelerated calcium removal, we performed a calcium flux analysis[82] and calculated transport rate constants for SERCA, NCX, and non-NCX pathways **(Table 7)**. T3+Dex treated cells displayed faster Ca^{2+} efflux via SERCA2 and NCX, although no differences in SR content were found **(Table 7)**. Consistent with the improved Ca^{2+} handling, cell shortening and contractile kinetics measured by edge detection[59] were also significantly enhanced by T3+Dex **(Table 8)**.

To examine the contribution of SR calcium release on calcium handling, we repeated whole-cell calcium fluorescence recordings after blocking SR calcium release with thapsigargin and ryanodine (**Figure 31A**). T3+Dex treated cells displayed a greater reduction in calcium transient amplitude following SR blockade (**Figure 31B**). Both groups demonstrated a similar delay in time to peak following SR blockade (42% and 54% longer) **(Figure 31C)**. Furthermore, the calcium decay rate was significantly longer (i.e. increased τ) in the T3+Dex treated compared to vehicle-treated cells (**Figure 31D**). Taken together, T3+Dex produced cells with a greater contribution of SR calcium release to CICR and an overall improvement in EC coupling.

T3+Dex increases cell capacitance and EC-coupling gain.

We next quantified the efficiency of coupling between LTCC current and SR-mediated calcium release by measuring the EC coupling gain (ECC gain) in voltage-clamped hiPSC-CM. ECC gain was calculated as the ratio of the amplitude of the cytoplasmic calcium release to the corresponding amplitude of the LTCC current at each membrane voltage. T3+Dex treated cells exhibited a greater rise in intracellular calcium for the respective membrane calcium current at each membrane potential (**Figure 33A**). On average, T3+Dex treatment significantly increased calcium transient amplitude despite reduced LTCC current density (**Figure 32B**). As a result, ECC gain was increased at most membrane potentials **(Figure 32C)**. Equivalent SR calcium content was confirmed by rapid caffeine application following each voltage protocol **(Figure 33D)**. Cell capacitance, a measure of cell surface membranes that includes t-tubules[96], was significantly increased in the T3+Dex group **(Figure 32E)**. The increase in cell capacitance (93%) was proportionally greater than the increase in cell surface area measured by 3D reconstruction, which excludes any membrane invaginations (54%). This result provides further evidence that the t-tubules formed after T3+Dex treatment were electrically connected to the sarcolemma.

A characteristic consequence of greater spatial proximity of LTCC, located primarily in t-tubules, and RyR2, located in the junctional SR, is faster LTCC inactivation. To assess this, a

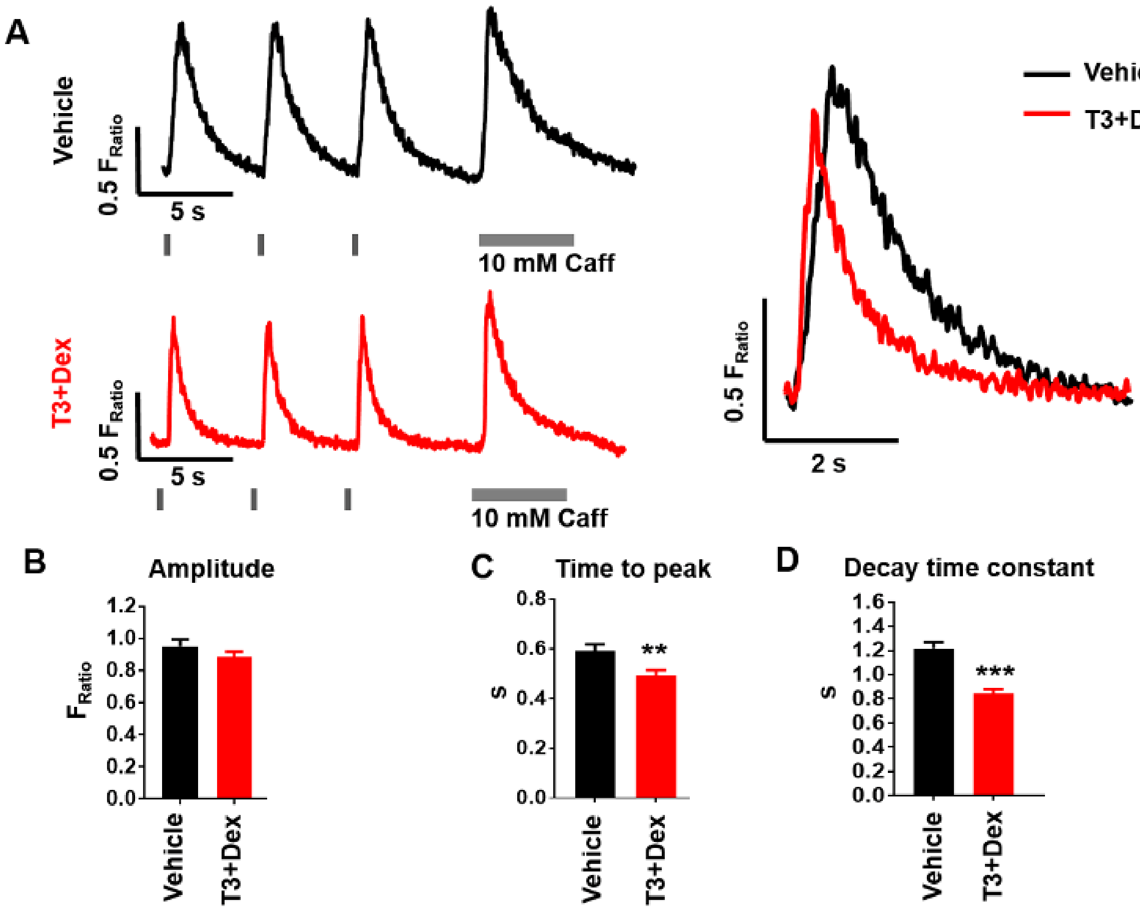

Figure 30: T3+Dex treated hiPSC-CM demonstrate greater dependence on SR calcium release for EC coupling. A) Representative examples of intracellular calcium transients recorded from Fura-2AM loaded hiPSC-CM with an overlay of the calcium transient from a T3+Dex treated cell **(red trace)** and a vehicle-treated cell **(black trace)**. Cells were paced at 0.2 Hz followed by rapid caffeine (Caff) application to measure SR calcium content. Note the significantly faster rate of calcium rise and rate of calcium decay in the T3+Dex treated cells. **B-D)** Summary data for calcium transient amplitude (**B**), time to peak (**C**), and transient decay tau (**D**); (n = 68-73 cells/group). Data reported as mean ± SEM (n = 16-21 cells/group); $^*p < 0.05$, $^{**}p < 0.01$, and $^{***}p < 0.001$ vs vehicle. Data collected in collaboration with Dr. Kyungsoo Kim. Adapted from[124].

Table 7: Calcium Handling

Parameter	Vehicle	T3+Dex	p-value
Diastolic Ca^{2+} (F_{Ratio})	1.3 ± 0.029	1.27 ± 0.027	0.22
Ca^{2+} transient amplitude (F_{Ratio})	0.94 ± 0.044	0.88 ± 0.034	0.23
Time to peak (s)	0.59 ± 0.025	0.49 ± 0.022	0.0036
Time to peak 50% (s)	0.21 ± 0.026	0.17 ± 0.023	0.036
Time to baseline 50% (s)	0.82 ± 0.03	0.60 ± 0.017	1.10E-09
SR Ca^{2+} content (F_{Ratio})	1.1 ± 0.054	0.97 ± 0.045	0.093
Ca^{2+} transient decay (t_{twitch}, s)	1.21 ± 0.053	0.84 ± 0.033	1.33E-08
Caff decay (t_{caff}, s)	2.46 ± 0.086	2.12 ± 0.098	0.011
0Na0Ca Caff decay ($t_{Caff0Na}$, s)	12.82 ± 0.77	10.67 ± 0.85	0.065
K_{SERCA}	0.43 ± 0.036	0.65 ± 0.057	0.02
K_{NCX}	0.36 ± 0.021	0.44 ± 0.03	0.03
$K_{non\text{-}NCX}$	0.089 ± 0.0054	0.10 ± 0.0062	0.089

Table 7: Calcium kinetic measurements of T3+Dex treated vs vehicle treated hiPSC-CM paced at 0.2 Hz. Data presented are mean ± SEM (n = 68 for control and 79 for T3+Dex). Unpaired, two tailed Student's t-test, p-value as listed. Data collected in collaboration with Dr. Kyungsoo Kim. Adapted from[124].

Table 8: Contractile Kinetics

Parameter	Vehicle	T3+Dex	p-value
Cell shortening (% of resting length)	5.55 ± 0.50	7.53 ± 0.70	0.02
Time to peak (s)	1.01 ± 0.04	0.71 ± 0.02	1.88E-07
Time to peak 50%	0.48 ± 0.03	0.37 ± 0.02	0.0028
Time to peak 90%	0.78 ± 0.03	0.56 ± 0.02	7.03E-06
Time to baseline 50%	0.58 ± 0.04	0.41 ± 0.09	2.07E-07
Time to baseline 90%	1.87 ± 0.02	1.20 ± 0.09	4.60E-06

Table 8: Contractile kinetic measurements of T3+Dex treated vs vehicle treated hiPSC-CM paced at 0.2 Hz. Data presented are mean±SEM (n = 68 for control and 79 for T3+Dex). Unpaired, two tailed Student's t-test, p-value as listed. Data collected in collaboration with Dr. Kyungsoo Kim. Adapted from[124].

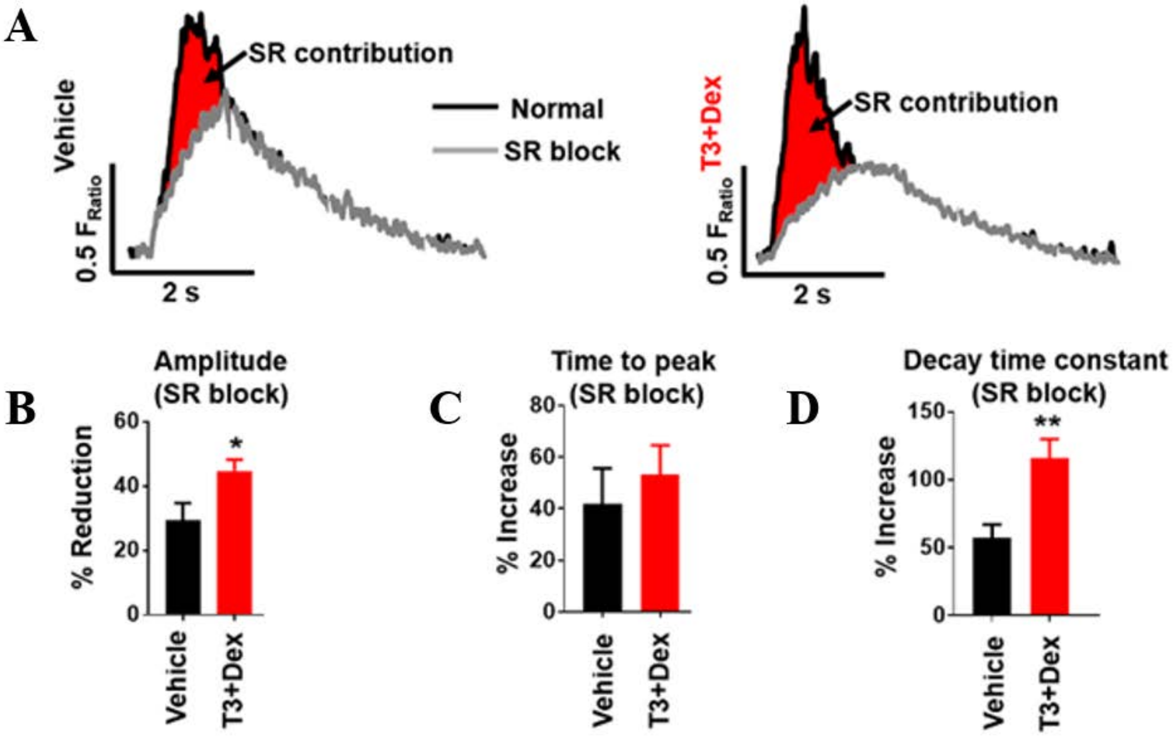

Figure 31: T3+Dex treated hiPSC-CM demonstrate greater dependence on SR calcium release for EC coupling. A) Representative paced calcium transients before (**black**) and after (**grey**) block of SR calcium release with thapsigargin and ryanodine. Note the larger contribution of SR calcium release to the calcium transient in T3+Dex treated cells. **B-D)** Summary data following SR blockade for calcium transient amplitude (**B**), time to peak **(C)**, and decay tau (**D).** Data are expressed as percent change from baseline before SR block. Data reported as mean ± SEM (n = 16-21 cells/group); $^*p < 0.05$, $^{**}p < 0.01$, and $^{***}p < 0.001$ vs vehicle. Data collected in collaboration with Dr. Kyungsoo Kim. Adapted from[124].

longer depolarization step was utilized to measure both voltage dependent inactivation ($\tau1$) and calcium dependent inactivation ($\tau2$) **(Figure 33A).** Results indicated an acceleration in $\tau1$ but not $\tau2$ **(Figure 33B, C)**, consistent with improved spatial organization of RyR2 and LTCC that occurs when t-tubules are present. Taken together, these results establish that T3+Dex enhances the efficiency of CICR in hiPSC-CM.

T3+Dex enhances elementary calcium release (calcium sparks) and RyR2 organization

In adult ventricular myocardium, t-tubules form dyads where sarcolemmal LTCCs are closely juxtaposed to clusters of SR RyR2 Ca-release channels. As such, dyad formation promotes RyR2 clustering and hence RyR2-mediated calcium release. The activity of RyR2 clusters but not that of single isolated RyR2 can be assessed by measuring calcium sparks[179]. To date, only a few reports exist on the presence of calcium sparks in hiPSC-CM[102, 180-182]. Representative longitudinal line scans of calcium sparks are shown in **Figure 34A**. T3+Dex treatment increased spark frequency, spark amplitude, and spark mass, with no significant differences in SR calcium content **(Figure 45B, C, D, E and Table 9).**

As RyR2 function was improved, we next assessed the structural organization of RyR2. Consistent with literature reports, vehicle treated cells showed diffuse RyR2 staining with predominant perinuclear localization[183]. In contrast, T3+Dex treated cells displayed reduced perinuclear RyR2 staining with striated organization and RyR2 clustering **(Figure 35)**. Taken together, these results provide evidence for enhanced organization and function of RyR2 in T3+Dex treated cells.

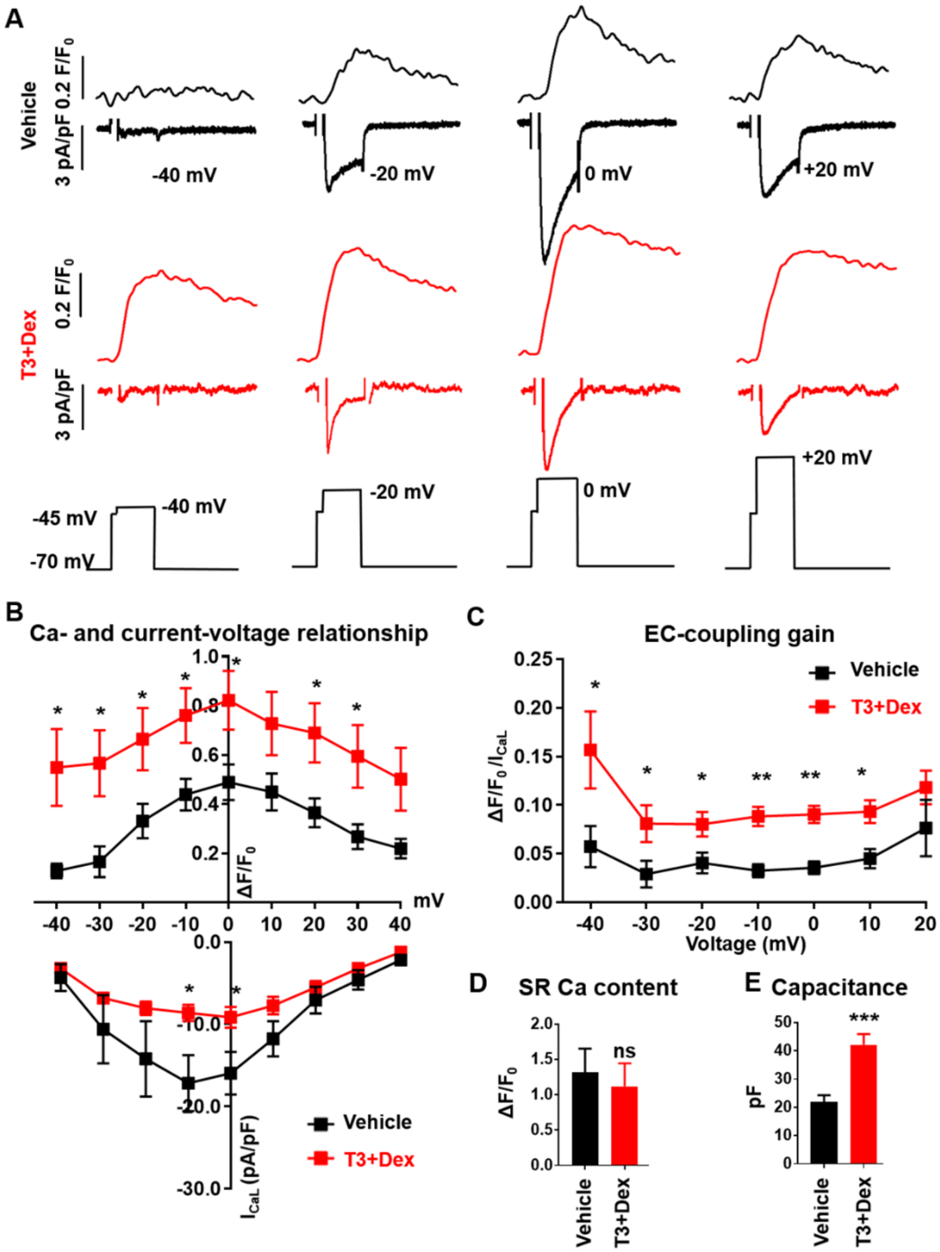

Figure 32: T3+Dex increases cell capacitance and EC-coupling gain. A) Representative examples of simultaneously-recorded intracellular calcium fluorescence traces (top) and L-type calcium currents (bottom) from vehicle-treated **(black)** and T3+Dex treated **(red)** hiPSC-CM. Records were obtained from voltage-clamped hiPSC-CM loaded with the fluorescent calcium indicator Fluo-4 and measured using the indicated voltage protocol. **B)** Average current-voltage relationship with associated intracellular calcium fluorescence at indicated membrane potentials in T3+Dex versus vehicle treated hiPSC-CM. **C)** EC coupling gain calculated as a ratio of normalized calcium fluorescence to normalized calcium current. **D)** SR calcium content. **E)** Cell capacitance. All data reported as mean ± SEM (n = 6-7); *$p < 0.05$, **$p < 0.01$, ***$p < 0.001$, vs vehicle, ns – non significant. Data collected in collaboration with Dr. Dmytro Kryshtal. Adapted from[124].

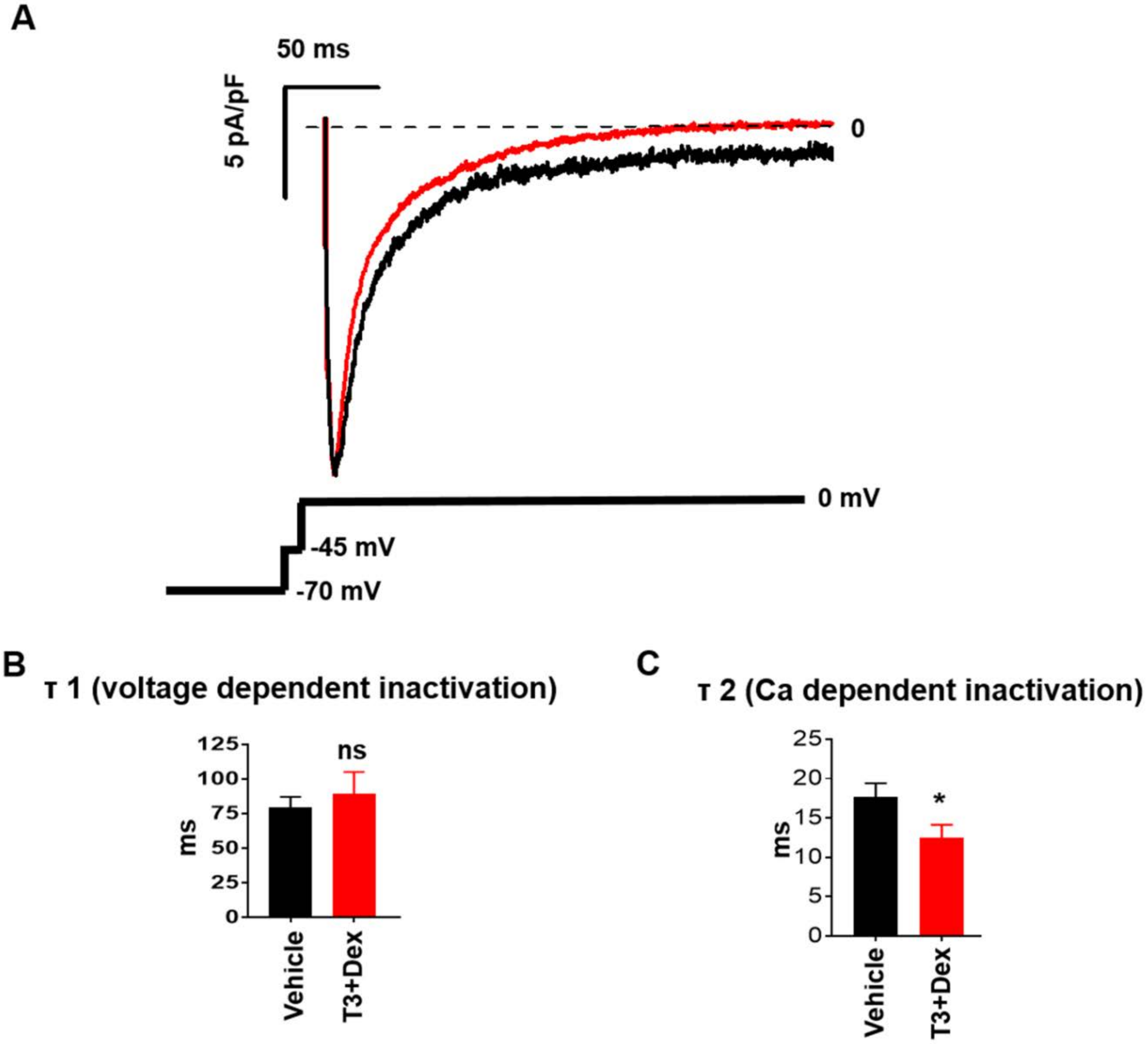

Figure 33: Ca-dependent inactivation of L-type calcium current is accelerated in the T3+Dex treated cells. A) Representative traces of I_{CaL} from a conditioning step of -45 mV to 0 mV in T3+Dex versus vehicle treated cells. Double exponential fit yields estimates of voltage dependent inactivation (tau 1) and calcium dependent inactivation (tau 2). **B-C)** Summary data for tau 1 and tau 2. Data reported as mean ± SEM (n = 9-12). Unpaired, two tailed Student's t-test: $^*p < 0.05$ vs vehicle, ns – non significant. Data collected in collaboration with Dr. Dmytro Kryshtal. Adapted from[124].

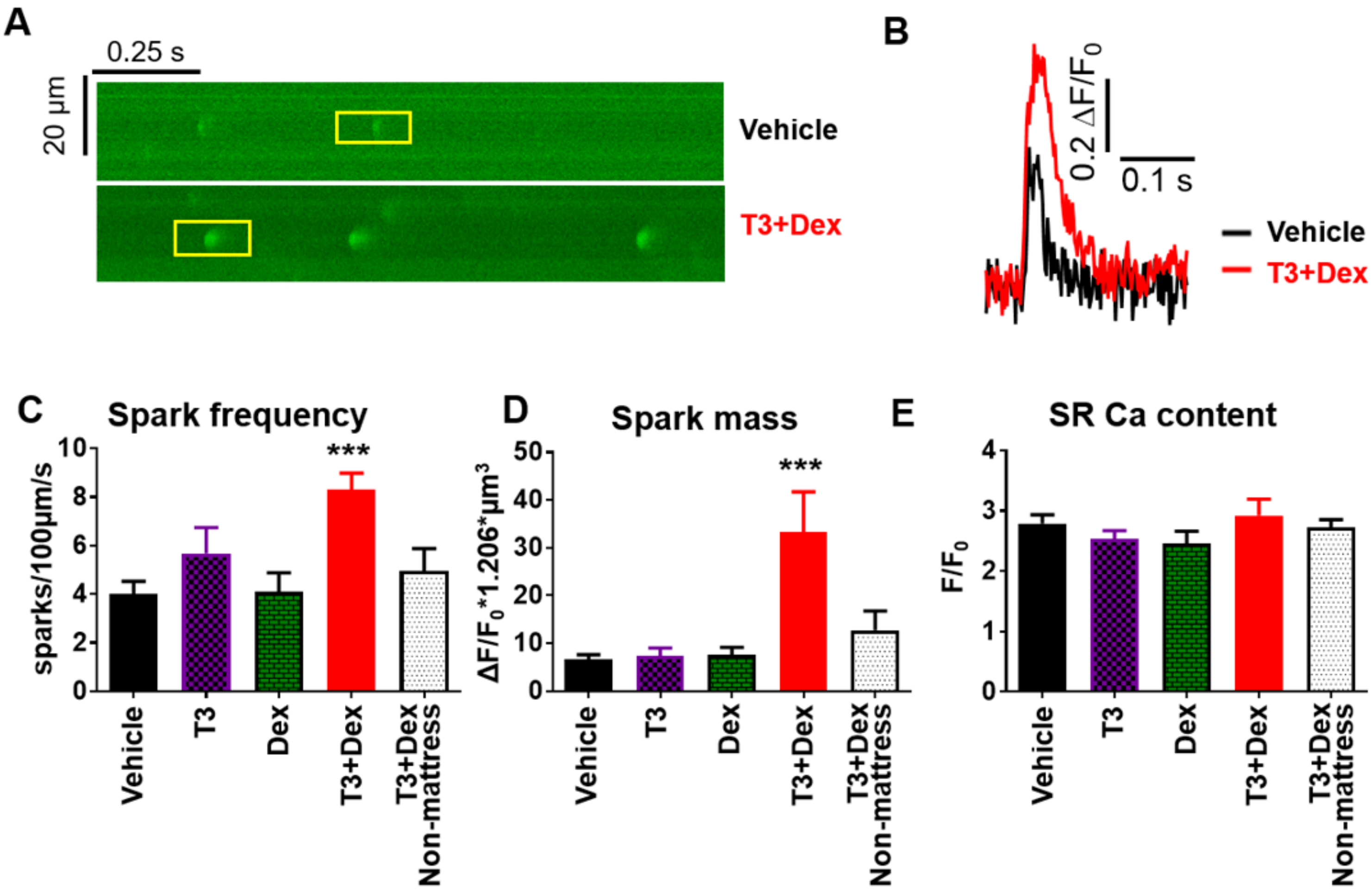

Figure 34: **T3+Dex enhances elementary calcium release (calcium sparks)**
A) Representative line-scans of calcium sparks recorded from saponin permeabilized hiPSC-CM. **B)** Overlay of representative calcium spark. **C-E)** Summary data for spark parameters for the different treatment groups (n = 15-37 cells/group). **F)** Representative cell images and fast Fourier transform of RyR2 immunostaining in T3+Dex and vehicle treated cells. Summary data of peak power of RyR2 immunostaining (n = 8-10 cells/group). All data reported as mean ± SEM; *p < 0.05 and ***p < 0.001 vs vehicle. Data collected in collaboration with Dr. Daniel Blackwell. Adapted from[124].

Table 9: Calcium Spark Parameters of hormone treated hiPSC-CM

Parameter	Vehicle (Mattress)	T3 (Mattress)	Dex (Mattress)	T3+Dex (Mattress)	T3+Dex (Non-mattress)
Spark frequency (sparks/100 µm/s)	4.02 ± 0.51	5.82 ± 1.06	4.09 ± 0.78	8.31 ± 0.67***	4.95 ± 0.94
Spark amplitude ($\Delta F/F_0$)	0.29 ± 0.02	0.26 ± 0.01	0.25 ± 0.01	0.46 ± 0.03**	0.31 ± 0.03
Spark mass ($\Delta F/F_0$*µm^3)	6.62 ± 0.99	7.36 ± 1.64	7.53 ± 1.61	33.36 ± 8.37***	12.76 ± 4.0
FWHM (µm)	2.52 ± 0.06	2.59 ± 0.07	2.56 ± 0.07	2.84 ± 0.05***	2.91 ± 0.07**
FDHM (ms)	27.84 ± 0.86	25.3 ± 0.63	25.42 ± 0.88	36.49 ± 0.86***	27.9 ± 1.21
Time to peak (ms)	16.24 ± 0.61	15.0 ± 0.61	16.73 ± 0.98	21.69 ± 0.78***	16.03 ± 0.82
Caffeine transient amplitude ($\Delta F/F_0$)	2.79 ± 0.15	2.54 ± 0.13	2.46 ± 0.2	2.92 ± 0.27	2.72 ± 0.13

Table 9: Full width half max (FWHM), Full duration half max (FDHM). Data are reported as mean ± SEM. One-way ANOVA with Tukey's post hoc test; *$p < 0.05$, **$p < 0.01$, and ***$p < 0.001$ vs vehicle. Data collected in collaboration with Dr. Daniel Blackwell. Adapted from[124].

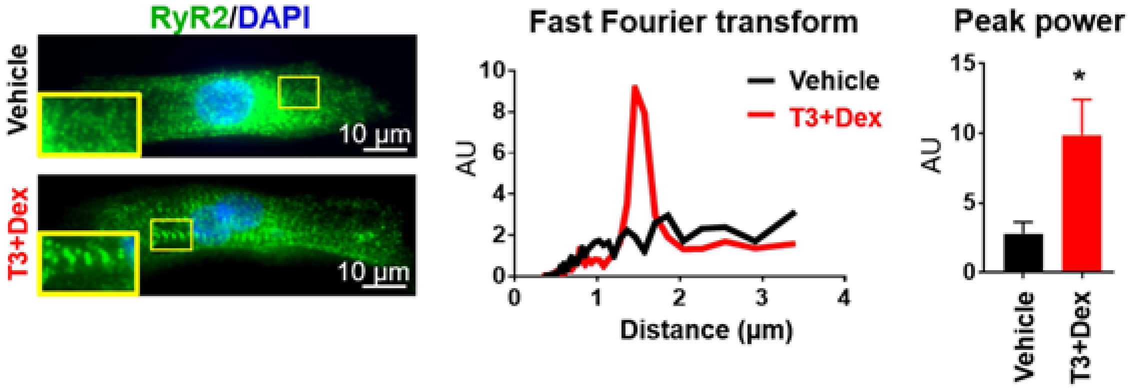

Figure 35: **T3+Dex enhances RyR2 organization.** Representative cell images and fast Fourier transform of RyR2 immunostaining in T3+Dex and vehicle treated cells. Summary data of peak power of RyR2 immunostaining (n = 8-10 cells/group). All data reported as mean ± SEM; *$p < 0.05$ and ***$p < 0.001$ vs vehicle. Data collected in collaboration with Dr. Daniel Blackwell, Dr. Lili Wang, Dr. Michael Frisk, and Dr. William Louch. Adapted from[124].

DISCUSSION

Here we report that a simple culture method – addition of T3+Dex during days 16-30 of cardiac induction followed by a 5 day culture on a Matrigel mattress – was sufficient to generate t-tubule development in hiPSC-CM. Although still less organized than in adult human myocardium, the new t-tubules were electrically coupled to the cell surface, and drastically enhanced CICR and ECC gain. T3+Dex promoted a more ventricular-like RyR2 organization, which likely contributed to the robust appearance of Ca^{2+} sparks and the greater participation of SR calcium handling to the EC coupling process. This finding is also supported by our data showing a significant reduction (**Figure 33)** in LTCC current in T3+Dex treated cells, further evidence for increased coupling between the RyR2 and LTCC that allows for more efficient negative feedback of SR calcium release on LTCC (i.e., increased Ca-dependent inactivation of LTCC, **Figure 34**). The results reported here represent a significant advancement, because previous approaches that accelerate hiPSC-CM maturation (i.e., addition of growth factors, length of cultivation, culturing on various substrate/patterning, in vivo maturation) have not enhanced t-tubule formation or provided evidence of ventricular-like EC coupling to the extent shown here[155].

The Matrigel mattress method (and others) has facilitated maturation of electrophysiological and calcium handling properties of hiPSC-CM, thereby demonstrating the importance of extracellular matrix for maturation[59, 155, 158]. Thyroid and glucocorticoid hormones are essential for optimal fetal and neonatal heart development and can also enhance hiPSC-CM maturation[172]. However, our results suggest that commonly used differentiation medium contains suboptimal concentrations of both hormones. Our findings highlight the importance of increasing fetal maturation factors during hiPSC-CM differentiation as well as the substrate dependence for promoting optimal CM development. Although mechanisms underlying this process are not yet elucidated, our data suggest that addition of T3+Dex primes the CM for functional and structural maturation and, when receiving proper substrate cues, is able to express these improvements.

In summary, our results suggest a permissive role of combined thyroid and glucocorticoid hormones during the cardiac differentiation process which, when coupled with further maturation on Matrigel mattress, is sufficient for robust t-tubule development, enhanced CICR, and more ventricular-like EC coupling. This provides proof of principle that functional t-tubule development can be achieved in single cell culture of hiPSC-CM. The hiPSC-CM structural and functional maturation appear to be mediated by two features: 1. Activation of pathways downstream of thyroid and glucocorticoid receptors and 2. Interaction with an extracellular matrix substrate of physiological stiffness. However, as our work does not provide an exhaustive list of molecular signatures of cardiomyocyte maturation, further assessment of the effects of T3+Dex mattress method on cellular metabolism and gene expression changes specific to EC coupling are still warranted. Furthermore, t-tubule development in T3+Dex treated hiPSC-CM after 5 days is less organized than in adult human myocardium, and more reminiscent to that found in day 15 postnatal rat hearts[178]. Hence, future studies are required to establish optimal culture conditions to achieve further t-tubule maturation (e.g., longer culture time, tuning substrate tension, and optimizing hormone concentrations). Indeed, our discovery encourages investigation of gene expression pathways downstream of thyroid and glucocorticoid receptors and we anticipate this will yield novel targets for further maturation of hiPSC-CM. Nevertheless, the new maturation technique reported here overcomes a major barrier in the stem cell field, which will help improve the utility of hiPSC-CM for disease modeling and enable future research into the molecular pathways underlying t-tubule development.

CHAPTER 4

CONCLUSIONS AND FUTURE DIRECTIONS

Dilated cardiomyopathy (DCM) is a significant contributor to morbidity and mortality worldwide. Curative treatments are non-existent and current strategies manage symptomology and delay disease progression. Although the etiology of DCM is multifactorial, with environment and lifestyle also shaping the progression of disease, the genetic contribution to this disease is well established and increasingly being reported. Current investigations of DCM have relied on the use of animal's models for enhancing our understanding of mechanisms of disease and testing therapeutic strategies. While these models have been useful, results have not always translated into humans. The need for more human like models has coincided with the development of human induced pluripotent stem cell derived cardiomyocyte models of disease. The advent of gene editing tools and progress in hiPSC-CM technology provides the scientific community an opportunity to interrogate specific genetic changes in a human cardiomyocyte-specific manner. Although advancements in these tools has allowed for investigation of DCM from a handful of mutations[115-123], the majority of the studies recapitulate only some aspects of DCM disease pathogenesis with little to no mechanistic insight. For certain DCM causing mutations, the most clinically relevant aspects (contractile deficits and pro-arrhythmic features) cannot be identified using hiPSC-CM models.

Chapter 2 Summary and Future directions

I first investigate hiPSC-CM generated from a patient diagnosed with LMNA cardiomyopathy due to the c.1526dupC mutation to provide insight on modeling this disease in a "dish." **Chapter 2** described the molecular and functional characterization of the LMNA DCM hiPSC-CM versus population control lines, while providing causality of the patient mutation through correction of the mutation using gene editing technology. Patient derived hiPSC-CM display reduced lamin A/C expression. Functional studies showed early deficits in calcium handling and contractility compared to population controls. Using CRISPR/Cas9 gene editing, I corrected the mutation and demonstrated rescue of lamin A/C expression and normalization of the contractile deficits. Future directions and limitations of modeling LMNA cardiomyopathy using patient derived hiPSC-CM include the following:

1. Patient derived cells retain the unique genetic background of that patient. Should there exist multiple variants in genes which act to modify (additive effect) the progression of this disease, it becomes difficult to assess severity and pathogenicity of a single variant. Furthermore, correction of the predicted pathogenic mutation with gene editing may not provide a complete rescue should multiple mutations contribute to pathogenicity. Gene editing of a single mutation into a "clean" well-characterized healthy population control will allow for a more accurate evaluation of single mutations in the absence of contributory genetic backgrounds. Studies incorporating the mutation in a healthy population control will further solidify findings.
2. My studies were predominantly completed comparing patient derived CM with those derived from a population control. Although multiple independent population controls were utilized, comparison of multiple independent lines for every experimental outcome is important to increase accuracy of findings. To definitively establish the cellular phenotype and underlying pathogenic mechanisms, future studies will have to consistently compare the patient derived lines with genetically corrected isogenic control lines.

3. Lamin cardiomyopathy is a progressive disease. Current studies modeling DCM in a “dish” tend to characterize cells at a single time point instead of in a serial fashion. It is important to perform serial measurements to identify the time point prior to the onset of severe phenotypic changes in order to tease out differences between causative mechanisms and secondary effects (e.g. to prevent the situation in which cells have contractile deficits in the setting of apoptosis). The studies in this thesis were performed between days 30-50 but predominantly focused at d35 and d40. Further evaluation is required in a serial fashion to identify best time points for mechanistic studies.

4. Prior investigations modeling LMNA cardiomyopathy did not adapt methods which allow for CM shortening for characterization of calcium kinetics and contractility. The studies performed here use substrate of physiological stiffness (Matrigel mattress) to allow for cellular shortening. Although Matrigel mattress uncovered calcium handling and contractility deficits, studies using improved maturation techniques may further uncover the phenotype.

5. Pro-arrhythmic features were not assessed. Although the CardioExyte96 allows for evaluation of the extracellular field potential to produce an action potential readout (field potential duration [FPD]), early versions of the model only allowed for spontaneous measurements. Cardiac action potential are highly rate dependent, showing significant action potential shortening with increase rate of pacing[184]. As such, the rate dependency of action potential duration is confounding when analyzing electrophysiological properties of spontaneously beating cells (e.g. not accurate to compare AP waveform at 40 bpm vs 90 bpm as it will appear longer). As LMNA hiPSC-CM appeared to have a bradycardic phenotype, these cells cannot be accurately assessed for such properties. To address this, I have implemented a method which allows for extracellular field potential measurement in the monolayer at user specified rate **(see Figure 36A-C)**. Using hiPSC-CM expressing a light sensitive cationic channel (Channelrhodopsin-2), cells can be stimulated in

response to a specific wavelength. Optical pacing provides 3 major advantages: 1) increases the number of measurable wells **(Figure 37A)**, 2) allows for synchronous activation of the monolayer **(Figure 37B)**, and 3) allows for control of the beating rate through pacing. Future studies will use the stimulating optical lid for baseline and pharmacological evaluation of rate-dependent changes in the FPD.

Overall, my findings provide a useful set of reagents for modeling LMNA cardiomyopathy without yet providing significant mechanistic insight. Interestingly, LMNA DCM hiPSC-CM plated on plastic or glass culture dishes did not exhibit contractile deficits or nuclear abnormalities, whereas use of a substrate of physiological stiffness begins to uncover the phenotype. However, the single cell contractile phenotype observed is not as dramatic as in other hiPSC-CM models of sarcomeric DCM[115]. Indeed this is a progressive disease which is not fully observed until the second or third decade of life, so how can we accelerate this process? Maturation on a substrate which enables cellular shortening and thus activates mechanosensitive pathways appears to promote uncovering of the phenotype, as does prolonged culture in monolayer. Further maturation of these cells will potentially uncover a stronger phenotype.

Chapter 3 Summary and Future directions

The maturation status of hiPSC-CM has remained a major limitation impeding implementation. Specifically, the lacking t-tubules are at the core of the electrophysiological immaturity observed in these cells, which if solved would greatly enhance their excitation-contraction coupling. As such, **Chapter 3** of my thesis focuses on maturation of hiPSC-CM. We found that addition of T3 and dexamethasone to during days 16-30 of CM generation combined with culturing on Matrigel mattress was sufficient to initiate t-tubule development at the single cell level, which has not yet been demonstrated in the literature. Consistent with the development of t-tubules, we find enhanced expression and improved localization of proteins associated with t-tubule development at the sarcomere Z-line. Functional characterization demonstrates significant improvements in excitation-contraction coupling with more efficient calcium-induced calcium release as well as accelerated calcium removal. Overall, the hormone technique provides a significant advantage for modeling disease as it creates cells with much improved calcium kinetics, thus increasing the range to uncover deterioration of functional and structural properties. Future directions are provided below:

1. This method was thoroughly characterized for use at the single cell level as treated hiPSC-CM are cultured on Matrigel mattress for 5 days prior to examination. To enable the use of high-throughput methodologies, it is imperative to adapt this technology to the monolayer. Hence, I utilized the CardioExcyte96 using the optical pacing feature to assess the contractile and electrophysiological properties of hormone treated cells **(Figure 38A, B).** Results demonstrate significant shortening of the field potential duration (FPD) suggesting increased repolarization reserve. The impedance waveform measurements for time to peak and baseline were accelerated compared to vehicle treated hiPSC-CM. Although the significance of accelerated impedance kinetics and shortened FPD are speculative, it may facilitate our ability to detect smaller changes in electrophysiological and contractile parameters as there is a greater range for dysfunction.
2. Although hormone treatment allowed for the initiation of t-tubule development in the hiPSC-CM, the underlying mechanisms are not understood. Mechanism of t-tubule development on a whole are not well understood. To examine the changes in gene expression underlying the observed structural and functional maturation we are performing RNA-sequencing for identification of pathways which can be further manipulated for expanded t-tubule development.

3. What are the implications of the hormone method for disease modeling? As I have generated a method to greatly enhance hiPSC-CM maturation, I hypothesize that the new hormone method will allow for examination of mechanisms of cardiac disease progression in LMNA DCM hiPSC-CM. For example, calcium sparks are a validated method for assessing SR calcium leak, a mechanism associated with ventricular arrhythmias[185]. As calcium sparks were not previously robustly measured in vehicle treated hiPSC-CM **(see Figure 34)**, the application of the hormone method will now allow me to assess whether SR calcium leak is present in LMNA DCM hiPSC-CM. Thus, these new experiments can begin to provide insight into the mechanism of arrhythmias observed in LMNA DCM patients. Furthermore, the combined optical pacing and hormone method will allow for a high-throughput evaluation of electrophysiological properties of the LMNA DCM hiPSC-CM generated in this thesis.

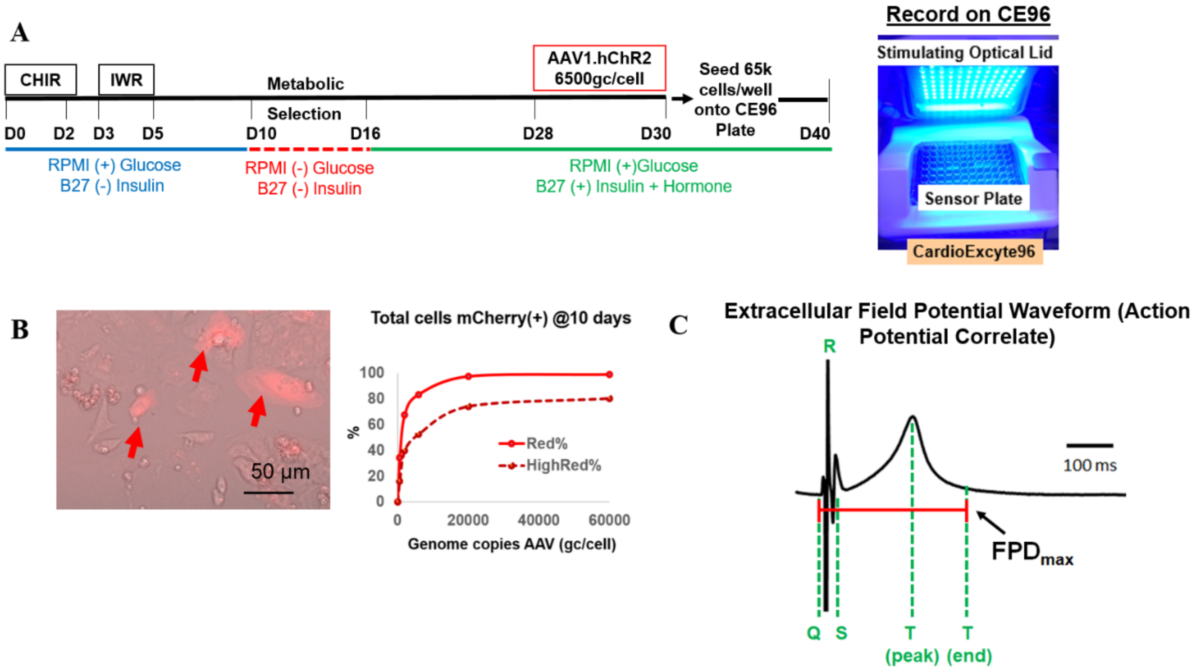

Figure 36: Implementation of optical pacing of hiPSC-CM in monolayer A) Timeline for generation, infection, and plating of hiPSC-CM in monolayer on the CardioExcyte96. **B)** Fluorescent micrograph and flow cytometry evaluation demonstrate sufficient infection of AAV1 expressing Channelrhodopsin-2 with as little as 6000 gc/cell. **C)** Cartoon extracellular field potential showing region defined as the field potential duration (action potential correlate). Data collected and analyzed by Shan Parikh with assistance Andrew Glazer.

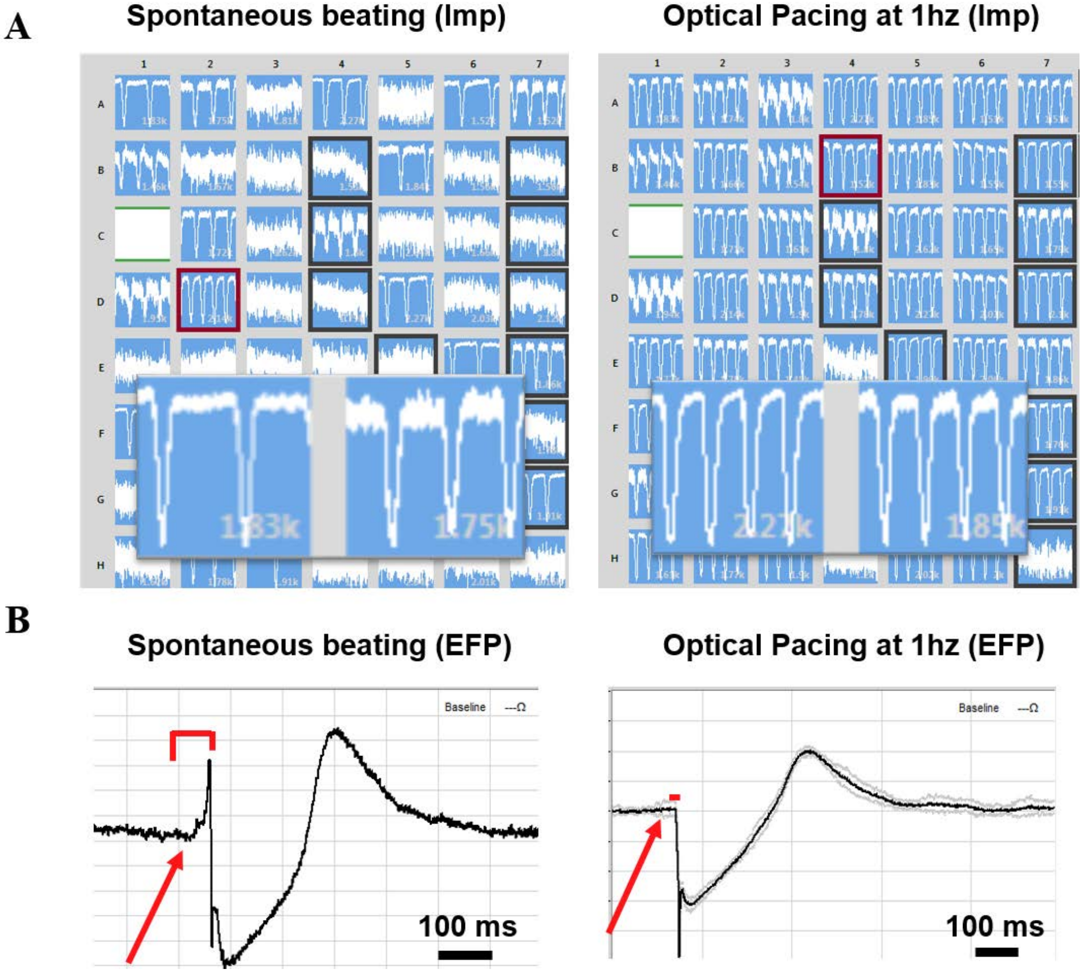

Figure 37: Optical pacing increases yield and accuracy of CardioExcyte96 data collection. A) Spontaneously beating hiPSC-CM do not all demonstrate measurable signal, however implementation of optical pacing greatly facilitates waveform detection and thus data collection. **B)** Optically paced hiPSC-CM in monolayer demonstrate uniform depolarization evident by delayed depolarization on the left and rapid depolarization on the right. Data collected and analyzed by Shan Parikh.

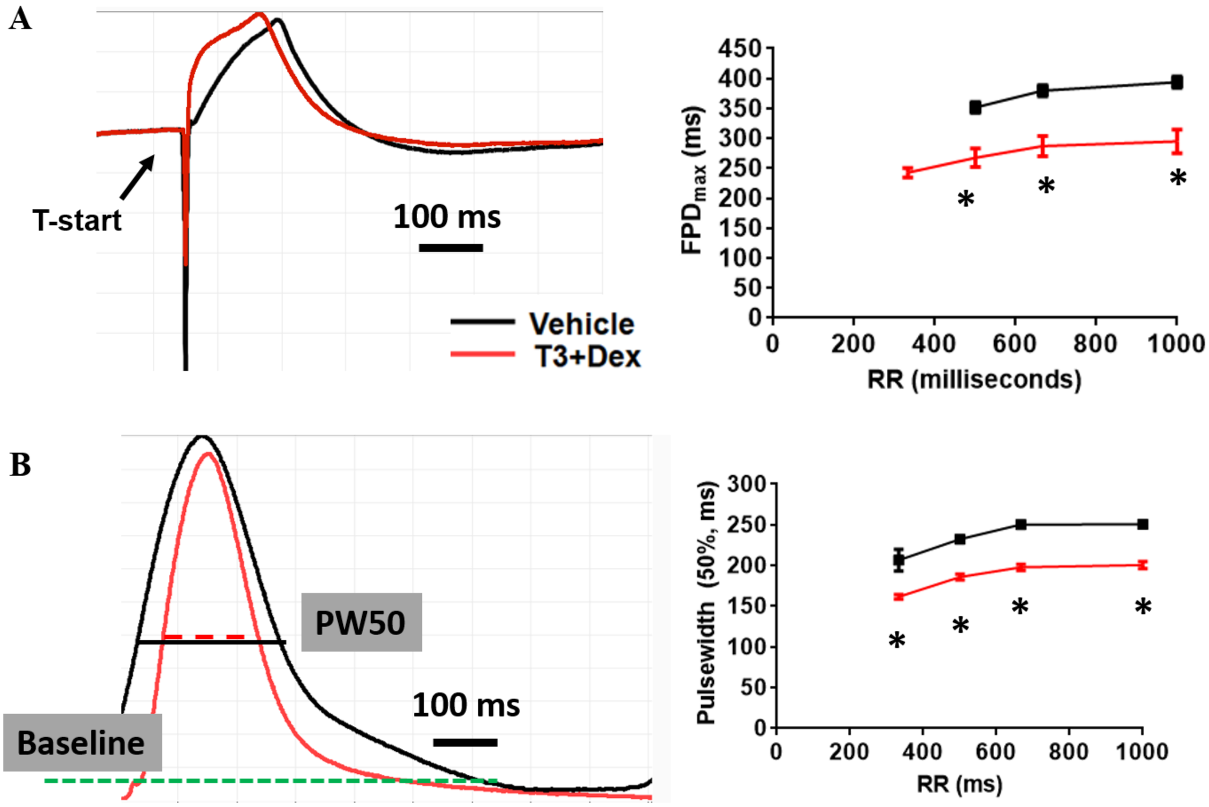

Figure 38: T3+Dex shortens field potential duration and reduces impedance waveform width. A) Representative EFP of T3+Dex versus vehicle treated hiPSC-CM monolayer. Graph demonstrates QT/RR relationship B) Representative impedance waveform of T3+Dex versus vehicle treated hiPSC-CM monolayer. Data shows reduction in pulse width 50% at all pacing rates measured. Data shown as mean ± SEM, *p < 0.001 hormone vs ctrl, student's t test. N = 6-15 from 2 independent differentiations. Data collected and analyzed by Shan Parikh with assistance from Lili Wang and Nikhil Chavali.

REFERENCES

1. Benjamin EJ, Blaha MJ, Chiuve SE, Cushman M, Das SR, Deo R, de Ferranti SD, Floyd J, Fornage M, Gillespie C, Isasi CR, Jimenez MC, Jordan LC, Judd SE, Lackland D, Lichtman JH, Lisabeth L, Liu S, Longenecker CT, Mackey RH, Matsushita K, Mozaffarian D, Mussolino ME, Nasir K, Neumar RW, Palaniappan L, Pandey DK, Thiagarajan RR, Reeves MJ, Ritchey M, Rodriguez CJ, Roth GA, Rosamond WD, Sasson C, Towfighi A, Tsao CW, Turner MB, Virani SS, Voeks JH, Willey JZ, Wilkins JT, Wu JH, Alger HM, Wong SS and Muntner P. Heart Disease and Stroke Statistics-2017 Update: A Report From the American Heart Association. *Circulation*. 2017;135:e146-e603.

2. Laverty H, Benson C, Cartwright E, Cross M, Garland C, Hammond T, Holloway C, McMahon N, Milligan J, Park B, Pirmohamed M, Pollard C, Radford J, Roome N, Sager P, Singh S, Suter T, Suter W, Trafford A, Volders P, Wallis R, Weaver R, York M and Valentin J. How can we improve our understanding of cardiovascular safety liabilities to develop safer medicines? *British journal of pharmacology*. 2011;163:675-93.

3. Gwathmey JK, Tsaioun K and Hajjar RJ. Cardionomics: a new integrative approach for screening cardiotoxicity of drug candidates. *Expert opinion on drug metabolism & toxicology*. 2009;5:647-60.

4. Kaitin KI and DiMasi JA. Pharmaceutical innovation in the 21st century: new drug approvals in the first decade, 2000-2009. *Clinical pharmacology and therapeutics*. 2011;89:183-8.

5. Fordyce CB, Roe MT, Ahmad T, Libby P, Borer JS, Hiatt WR, Bristow MR, Packer M, Wasserman SM, Braunstein N, Pitt B, DeMets DL, Cooper-Arnold K, Armstrong PW, Berkowitz SD, Scott R, Prats J, Galis ZS, Stockbridge N, Peterson ED and Califf RM. Cardiovascular drug development: is it dead or just hibernating? *Journal of the American College of Cardiology*. 2015;65:1567-82.

6. Perlman RL. Mouse models of human disease: An evolutionary perspective. *Evolution, medicine, and public health*. 2016;2016:170-6.

7. Elsea SH and Lucas RE. The mousetrap: what we can learn when the mouse model does not mimic the human disease. *ILAR journal*. 2002;43:66-79.

8. Hunter AJ. Have animal models of disease helped or hindered the drug discovery process? *Annals of the New York Academy of Sciences*. 2011;1245:1-2.

9. Goh KI, Cusick ME, Valle D, Childs B, Vidal M and Barabasi AL. The human disease network. *Proceedings of the National Academy of Sciences of the United States of America*. 2007;104:8685-90.

10. Ravasi T, Suzuki H, Cannistraci CV, Katayama S, Bajic VB, Tan K, Akalin A, Schmeier S, Kanamori-Katayama M, Bertin N, Carninci P, Daub CO, Forrest AR, Gough J, Grimmond S, Han JH, Hashimoto T, Hide W, Hofmann O, Kamburov A, Kaur M, Kawaji H, Kubosaki A, Lassmann T, van Nimwegen E, MacPherson CR, Ogawa C, Radovanovic A, Schwartz A,

Teasdale RD, Tegner J, Lenhard B, Teichmann SA, Arakawa T, Ninomiya N, Murakami K, Tagami M, Fukuda S, Imamura K, Kai C, Ishihara R, Kitazume Y, Kawai J, Hume DA, Ideker T and Hayashizaki Y. An atlas of combinatorial transcriptional regulation in mouse and man. *Cell*. 2010;140:744-52.

11. Seok J, Warren HS, Cuenca AG, Mindrinos MN, Baker HV, Xu W, Richards DR, McDonald-Smith GP, Gao H, Hennessy L, Finnerty CC, Lopez CM, Honari S, Moore EE, Minei JP, Cuschieri J, Bankey PE, Johnson JL, Sperry J, Nathens AB, Billiar TR, West MA, Jeschke MG, Klein MB, Gamelli RL, Gibran NS, Brownstein BH, Miller-Graziano C, Calvano SE, Mason PH, Cobb JP, Rahme LG, Lowry SF, Maier RV, Moldawer LL, Herndon DN, Davis RW, Xiao W and Tompkins RG. Genomic responses in mouse models poorly mimic human inflammatory diseases. *Proceedings of the National Academy of Sciences of the United States of America*. 2013;110:3507-12.

12. Nerbonne JM, Nichols CG, Schwarz TL and Escande D. Genetic manipulation of cardiac K(+) channel function in mice: what have we learned, and where do we go from here? *Circulation research*. 2001;89:944-56.

13. McGivern JV and Ebert AD. Exploiting pluripotent stem cell technology for drug discovery, screening, safety, and toxicology assessments. *Advanced drug delivery reviews*. 2014;69-70:170-8.

14. Sinnecker D, Laugwitz KL and Moretti A. Induced pluripotent stem cell-derived cardiomyocytes for drug development and toxicity testing. *Pharmacology & therapeutics*. 2014;143:246-52.

15. Khanna I. Drug discovery in pharmaceutical industry: productivity challenges and trends. *Drug discovery today*. 2012;17:1088-102.

16. Shi Y, Inoue H, Wu JC and Yamanaka S. Induced pluripotent stem cell technology: a decade of progress. *Nature reviews Drug discovery*. 2017;16:115-130.

17. Chen IY, Matsa E and Wu JC. Induced pluripotent stem cells: at the heart of cardiovascular precision medicine. *Nature reviews Cardiology*. 2016;13:333-49.

18. Sayed N, Liu C and Wu JC. Translation of Human-Induced Pluripotent Stem Cells: From Clinical Trial in a Dish to Precision Medicine. *Journal of the American College of Cardiology*. 2016;67:2161-76.

19. Harris K, Aylott M, Cui Y, Louttit JB, McMahon NC and Sridhar A. Comparison of electrophysiological data from human-induced pluripotent stem cell-derived cardiomyocytes to functional preclinical safety assays. *Toxicological sciences : an official journal of the Society of Toxicology*. 2013;134:412-26.

20. Passini E, Britton OJ, Lu HR, Rohrbacher J, Hermans AN, Gallacher DJ, Greig RJH, Bueno-Orovio A and Rodriguez B. Human In Silico Drug Trials Demonstrate Higher Accuracy than Animal Models in Predicting Clinical Pro-Arrhythmic Cardiotoxicity. *Frontiers in physiology*. 2017;8:668.

21. Takahashi K and Yamanaka S. Induction of pluripotent stem cells from mouse embryonic and adult fibroblast cultures by defined factors. *Cell*. 2006;126:663-76.

22. Takahashi K, Tanabe K, Ohnuki M, Narita M, Ichisaka T, Tomoda K and Yamanaka S. Induction of pluripotent stem cells from adult human fibroblasts by defined factors. *Cell*. 2007;131:861-72.

23. Loh YH, Agarwal S, Park IH, Urbach A, Huo H, Heffner GC, Kim K, Miller JD, Ng K and Daley GQ. Generation of induced pluripotent stem cells from human blood. *Blood*. 2009;113:5476-9.

24. Zhou T, Benda C, Duzinger S, Huang Y, Li X, Li Y, Guo X, Cao G, Chen S, Hao L, Chan YC, Ng KM, Ho JC, Wieser M, Wu J, Redl H, Tse HF, Grillari J, Grillari-Voglauer R, Pei D and Esteban MA. Generation of induced pluripotent stem cells from urine. *Journal of the American Society of Nephrology : JASN*. 2011;22:1221-8.

25. Cai J, Li W, Su H, Qin D, Yang J, Zhu F, Xu J, He W, Guo X, Labuda K, Peterbauer A, Wolbank S, Zhong M, Li Z, Wu W, So KF, Redl H, Zeng L, Esteban MA and Pei D. Generation of human induced pluripotent stem cells from umbilical cord matrix and amniotic membrane mesenchymal cells. *The Journal of biological chemistry*. 2010;285:11227-34.

26. Malik N and Rao MS. A review of the methods for human iPSC derivation. *Methods in molecular biology (Clifton, NJ)*. 2013;997:23-33.

27. Kim D, Kim CH, Moon JI, Chung YG, Chang MY, Han BS, Ko S, Yang E, Cha KY, Lanza R and Kim KS. Generation of human induced pluripotent stem cells by direct delivery of reprogramming proteins. *Cell stem cell*. 2009;4:472-6.

28. Qin H, Zhao A and Fu X. Small molecules for reprogramming and transdifferentiation. *Cellular and molecular life sciences : CMLS*. 2017;74:3553-3575.

29. Ma T, Xie M, Laurent T and Ding S. Progress in the reprogramming of somatic cells. *Circulation research*. 2013;112:562-74.

30. Soares FA, Sheldon M, Rao M, Mummery C and Vallier L. International coordination of large-scale human induced pluripotent stem cell initiatives: Wellcome Trust and ISSCR workshops white paper. *Stem cell reports*. 2014;3:931-9.

31. Hockemeyer D and Jaenisch R. Induced Pluripotent Stem Cells Meet Genome Editing. *Cell stem cell*. 2016;18:573-86.

32. Kim JS. Genome editing comes of age. *Nature protocols*. 2016;11:1573-8.

33. Brazelton VA, Jr., Zarecor S, Wright DA, Wang Y, Liu J, Chen K, Yang B and Lawrence-Dill CJ. A quick guide to CRISPR sgRNA design tools. *GM crops & food*. 2015;6:266-76.

34. Jinek M, Chylinski K, Fonfara I, Hauer M, Doudna JA and Charpentier E. A programmable dual-RNA-guided DNA endonuclease in adaptive bacterial immunity. *Science (New York, NY)*. 2012;337:816-21.

35. Ran FA, Hsu PD, Wright J, Agarwala V, Scott DA and Zhang F. Genome engineering using the CRISPR-Cas9 system. *Nature protocols*. 2013;8:2281-308.

36. Dash BC, Jiang Z, Suh C and Qyang Y. Induced pluripotent stem cell-derived vascular smooth muscle cells: methods and application. *The Biochemical journal*. 2015;465:185-94.

37. Liang X, Potter J, Kumar S, Zou Y, Quintanilla R, Sridharan M, Carte J, Chen W, Roark N, Ranganathan S, Ravinder N and Chesnut JD. Rapid and highly efficient mammalian cell engineering via Cas9 protein transfection. *Journal of biotechnology*. 2015;208:44-53.

38. Paquet D, Kwart D, Chen A, Sproul A, Jacob S, Teo S, Olsen KM, Gregg A, Noggle S and Tessier-Lavigne M. Efficient introduction of specific homozygous and heterozygous mutations using CRISPR/Cas9. *Nature*. 2016;533:125-9.

39. Wang L, Kim K, Parikh S, Cadar AG, Bersell KR, He H, Pinto JR, Kryshtal DO and Knollmann BC. Hypertrophic cardiomyopathy-linked mutation in troponin T causes myofibrillar disarray and pro-arrhythmic action potential changes in human iPSC cardiomyocytes. *Journal of molecular and cellular cardiology*. 2017;114:320-327.

40. Salsman J and Dellaire G. Precision genome editing in the CRISPR era. *Biochemistry and cell biology = Biochimie et biologie cellulaire*. 2017;95:187-201.

41. Maruyama T, Dougan SK, Truttmann MC, Bilate AM, Ingram JR and Ploegh HL. Increasing the efficiency of precise genome editing with CRISPR-Cas9 by inhibition of nonhomologous end joining. *Nature biotechnology*. 2015;33:538-42.

42. Chu VT, Weber T, Wefers B, Wurst W, Sander S, Rajewsky K and Kuhn R. Increasing the efficiency of homology-directed repair for CRISPR-Cas9-induced precise gene editing in mammalian cells. *Nature biotechnology*. 2015;33:543-8.

43. Richardson CD, Ray GJ, DeWitt MA, Curie GL and Corn JE. Enhancing homology-directed genome editing by catalytically active and inactive CRISPR-Cas9 using asymmetric donor DNA. *Nature biotechnology*. 2016;34:339-44.

44. Liang X, Potter J, Kumar S, Ravinder N and Chesnut JD. Enhanced CRISPR/Cas9-mediated precise genome editing by improved design and delivery of gRNA, Cas9 nuclease, and donor DNA. *Journal of biotechnology*. 2017;241:136-146.

45. Itskovitz-Eldor J, Schuldiner M, Karsenti D, Eden A, Yanuka O, Amit M, Soreq H and Benvenisty N. Differentiation of human embryonic stem cells into embryoid bodies compromising the three embryonic germ layers. *Molecular medicine (Cambridge, Mass)*. 2000;6:88-95.

46. Mummery C, Ward-van Oostwaard D, Doevendans P, Spijker R, van den Brink S, Hassink R, van der Heyden M, Opthof T, Pera M, de la Riviere AB, Passier R and Tertoolen L. Differentiation of human embryonic stem cells to cardiomyocytes: role of coculture with visceral endoderm-like cells. *Circulation*. 2003;107:2733-40.

47. Passier R, Oostwaard DW, Snapper J, Kloots J, Hassink RJ, Kuijk E, Roelen B, de la Riviere AB and Mummery C. Increased cardiomyocyte differentiation from human embryonic stem cells in serum-free cultures. *Stem cells (Dayton, Ohio)*. 2005;23:772-80.

48. Freund C, Ward-van Oostwaard D, Monshouwer-Kloots J, van den Brink S, van Rooijen M, Xu X, Zweigerdt R, Mummery C and Passier R. Insulin redirects differentiation from cardiogenic mesoderm and endoderm to neuroectoderm in differentiating human embryonic stem cells. *Stem cells (Dayton, Ohio)*. 2008;26:724-33.

49. Burridge PW, Keller G, Gold JD and Wu JC. Production of de novo cardiomyocytes: human pluripotent stem cell differentiation and direct reprogramming. *Cell stem cell*. 2012;10:16-28.

50. Baharvand H, Azarnia M, Parivar K and Ashtiani SK. The effect of extracellular matrix on embryonic stem cell-derived cardiomyocytes. *Journal of molecular and cellular cardiology*. 2005;38:495-503.

51. Sharma A, Li G, Rajarajan K, Hamaguchi R, Burridge PW and Wu SM. Derivation of highly purified cardiomyocytes from human induced pluripotent stem cells using small molecule-modulated differentiation and subsequent glucose starvation. *Journal of visualized experiments : JoVE*. 2015.

52. Burridge PW, Holmstrom A and Wu JC. Chemically Defined Culture and Cardiomyocyte Differentiation of Human Pluripotent Stem Cells. *Current protocols in human genetics*. 2015;87:21.3.1-15.

53. Sharma A, Marceau C, Hamaguchi R, Burridge PW, Rajarajan K, Churko JM, Wu H, Sallam KI, Matsa E, Sturzu AC, Che Y, Ebert A, Diecke S, Liang P, Red-Horse K, Carette JE, Wu SM and Wu JC. Human induced pluripotent stem cell-derived cardiomyocytes as an in vitro model for coxsackievirus B3-induced myocarditis and antiviral drug screening platform. *Circulation research*. 2014;115:556-66.

54. Stockbridge N, Morganroth J, Shah RR and Garnett C. Dealing with global safety issues : was the response to QT-liability of non-cardiac drugs well coordinated? *Drug safety*. 2013;36:167-82.

55. Shah RR. Cardiac repolarisation and drug regulation: assessing cardiac safety 10 years after the CPMP guidance. *Drug safety*. 2007;30:1093-110.

56. Roden DM. Taking the "idio" out of "idiosyncratic": predicting torsades de pointes. *Pacing and clinical electrophysiology : PACE*. 1998;21:1029-34.

57. Laurila E, Ahola A, Hyttinen J and Aalto-Setala K. Methods for in vitro functional analysis of iPSC derived cardiomyocytes - Special focus on analyzing the mechanical beating behavior. *Biochimica et biophysica acta*. 2016;1863:1864-72.

58. Beussman KM, Rodriguez ML, Leonard A, Taparia N, Thompson CR and Sniadecki NJ. Micropost arrays for measuring stem cell-derived cardiomyocyte contractility. *Methods (San Diego, Calif)*. 2016;94:43-50.

59. Feaster TK, Cadar AG, Wang L, Williams CH, Chun YW, Hempel JE, Bloodworth N, Merryman WD, Lim CC, Wu JC, Knollmann BC and Hong CC. Matrigel Mattress: A Method for the Generation of Single Contracting Human-Induced Pluripotent Stem Cell-Derived Cardiomyocytes. *Circulation research*. 2015;117:995-1000.

60. Scott CW, Zhang X, Abi-Gerges N, Lamore SD, Abassi YA and Peters MF. An impedance-based cellular assay using human iPSC-derived cardiomyocytes to quantify modulators of cardiac contractility. *Toxicological sciences : an official journal of the Society of Toxicology*. 2014;142:331-8.

61. Doerr L, Thomas U, Guinot DR, Bot CT, Stoelzle-Feix S, Beckler M, George M and Fertig N. New easy-to-use hybrid system for extracellular potential and impedance recordings. *Journal of laboratory automation*. 2015;20:175-88.

62. Rajamohan D, Matsa E, Kalra S, Crutchley J, Patel A, George V and Denning C. Current status of drug screening and disease modelling in human pluripotent stem cells. *BioEssays : news and reviews in molecular, cellular and developmental biology*. 2013;35:281-98.

63. Lu HR, Whittaker R, Price JH, Vega R, Pfeiffer ER, Cerignoli F, Towart R and Gallacher DJ. High Throughput Measurement of Ca++ Dynamics in Human Stem Cell-Derived Cardiomyocytes by Kinetic Image Cytometery: A Cardiac Risk Assessment Characterization Using a Large Panel of Cardioactive and Inactive Compounds. *Toxicological sciences : an official journal of the Society of Toxicology*. 2015;148:503-16.

64. Pfeiffer ER, Vega R, McDonough PM, Price JH and Whittaker R. Specific prediction of clinical QT prolongation by kinetic image cytometry in human stem cell derived cardiomyocytes. *Journal of pharmacological and toxicological methods*. 2016;81:263-73.

65. Ando H, Yoshinaga T, Yamamoto W, Asakura K, Uda T, Taniguchi T, Ojima A, Shinkyo R, Kikuchi K, Osada T, Hayashi S, Kasai C, Miyamoto N, Tashibu H, Yamazaki D, Sugiyama A, Kanda Y, Sawada K and Sekino Y. A new paradigm for drug-induced torsadogenic risk assessment using human iPS cell-derived cardiomyocytes. *Journal of pharmacological and toxicological methods*. 2017;84:111-127.

66. Takasuna K, Asakura K, Araki S, Ando H, Kazusa K, Kitaguchi T, Kunimatsu T, Suzuki S and Miyamoto N. Comprehensive in vitro cardiac safety assessment using human stem cell technology: Overview of CSAHi HEART initiative. *Journal of pharmacological and toxicological methods*. 2017;83:42-54.

67. Mulder P, de Korte T, Dragicevic E, Kraushaar U, Printemps R, Vlaming MLH, Braam SR and Valentin JP. Predicting cardiac safety using human induced pluripotent stem cell-derived cardiomyocytes combined with multi-electrode array (MEA) technology: A conference report. *Journal of pharmacological and toxicological methods*. 2018;91:36-42.

68. Koivumaki JT, Naumenko N, Tuomainen T, Takalo J, Oksanen M, Puttonen KA, Lehtonen S, Kuusisto J, Laakso M, Koistinaho J and Tavi P. Structural Immaturity of Human iPSC-Derived Cardiomyocytes: In Silico Investigation of Effects on Function and Disease Modeling. *Frontiers in physiology*. 2018;9:80.

69. Ma J, Guo L, Fiene SJ, Anson BD, Thomson JA, Kamp TJ, Kolaja KL, Swanson BJ and January CT. High purity human-induced pluripotent stem cell-derived cardiomyocytes: electrophysiological properties of action potentials and ionic currents. *American journal of physiology Heart and circulatory physiology*. 2011;301:H2006-17.

70. Goversen B, van der Heyden MAG, van Veen TAB and de Boer TP. The immature electrophysiological phenotype of iPSC-CMs still hampers in vitro drug screening: Special focus on IK1. *Pharmacology & therapeutics*. 2017.

71. Li M, Kanda Y, Ashihara T, Sasano T, Nakai Y, Kodama M, Hayashi E, Sekino Y, Furukawa T and Kurokawa J. Overexpression of KCNJ2 in induced pluripotent stem cell-derived cardiomyocytes for the assessment of QT-prolonging drugs. *Journal of pharmacological sciences*. 2017;134:75-85.

72. Verkerk AO, Veerman CC, Zegers JG, Mengarelli I, Bezzina CR and Wilders R. Patch-Clamp Recording from Human Induced Pluripotent Stem Cell-Derived Cardiomyocytes: Improving Action Potential Characteristics through Dynamic Clamp. *International journal of molecular sciences*. 2017;18.

73. Vaidyanathan R, Markandeya YS, Kamp TJ, Makielski JC, January CT and Eckhardt LL. IK1-enhanced human-induced pluripotent stem cell-derived cardiomyocytes: an improved cardiomyocyte model to investigate inherited arrhythmia syndromes. *American journal of physiology Heart and circulatory physiology*. 2016;310:H1611-21.

74. Rojas SV, Kensah G, Rotaermel A, Baraki H, Kutschka I, Zweigerdt R, Martin U, Haverich A, Gruh I and Martens A. Transplantation of purified iPSC-derived cardiomyocytes in myocardial infarction. *PloS one*. 2017;12:e0173222.

75. Ye L, Chang YH, Xiong Q, Zhang P, Zhang L, Somasundaram P, Lepley M, Swingen C, Su L, Wendel JS, Guo J, Jang A, Rosenbush D, Greder L, Dutton JR, Zhang J, Kamp TJ, Kaufman DS, Ge Y and Zhang J. Cardiac repair in a porcine model of acute myocardial infarction with human induced pluripotent stem cell-derived cardiovascular cells. *Cell stem cell*. 2014;15:750-61.

76. Chong JJ, Yang X, Don CW, Minami E, Liu YW, Weyers JJ, Mahoney WM, Van Biber B, Cook SM, Palpant NJ, Gantz JA, Fugate JA, Muskheli V, Gough GM, Vogel KW, Astley CA, Hotchkiss CE, Baldessari A, Pabon L, Reinecke H, Gill EA, Nelson V, Kiem HP, Laflamme MA

and Murry CE. Human embryonic-stem-cell-derived cardiomyocytes regenerate non-human primate hearts. *Nature*. 2014;510:273-7.

77. Shiba Y, Gomibuchi T, Seto T, Wada Y, Ichimura H, Tanaka Y, Ogasawara T, Okada K, Shiba N, Sakamoto K, Ido D, Shiina T, Ohkura M, Nakai J, Uno N, Kazuki Y, Oshimura M, Minami I and Ikeda U. Allogeneic transplantation of iPS cell-derived cardiomyocytes regenerates primate hearts. *Nature*. 2016;538:388-391.

78. Masoudpour H and Laflamme MA. Cardiac repair with pluripotent stem cell-derived cardiomyocytes: Proof of concept but new challenges. *The Journal of thoracic and cardiovascular surgery*. 2017;154:945-948.

79. Eisner DA, Caldwell JL, Kistamas K and Trafford AW. Calcium and Excitation-Contraction Coupling in the Heart. *Circulation research*. 2017;121:181-195.

80. Knollmann BC. New roles of calsequestrin and triadin in cardiac muscle. *The Journal of physiology*. 2009;587:3081-7.

81. Lock JT, Parker I and Smith IF. A comparison of fluorescent Ca(2)(+) indicators for imaging local Ca(2)(+) signals in cultured cells. *Cell calcium*. 2015;58:638-48.

82. Hwang HS, Kryshtal DO, Feaster TK, Sanchez-Freire V, Zhang J, Kamp TJ, Hong CC, Wu JC and Knollmann BC. Comparable calcium handling of human iPSC-derived cardiomyocytes generated by multiple laboratories. *Journal of molecular and cellular cardiology*. 2015;85:79-88.

83. Brette F and Orchard C. Resurgence of cardiac t-tubule research. *Physiology (Bethesda, Md)*. 2007;22:167-73.

84. van den Berg CW, Okawa S, Chuva de Sousa Lopes SM, van Iperen L, Passier R, Braam SR, Tertoolen LG, del Sol A, Davis RP and Mummery CL. Transcriptome of human foetal heart compared with cardiomyocytes from pluripotent stem cells. *Development (Cambridge, England)*. 2015;142:3231-8.

85. Rao C, Prodromakis T, Kolker L, Chaudhry UA, Trantidou T, Sridhar A, Weekes C, Camelliti P, Harding SE, Darzi A, Yacoub MH, Athanasiou T and Terracciano CM. The effect of microgrooved culture substrates on calcium cycling of cardiac myocytes derived from human induced pluripotent stem cells. *Biomaterials*. 2013;34:2399-411.

86. Itzhaki I, Rapoport S, Huber I, Mizrahi I, Zwi-Dantsis L, Arbel G, Schiller J and Gepstein L. Calcium handling in human induced pluripotent stem cell derived cardiomyocytes. *PloS one*. 2011;6:e18037.

87. Lee YK, Ng KM, Lai WH, Chan YC, Lau YM, Lian Q, Tse HF and Siu CW. Calcium homeostasis in human induced pluripotent stem cell-derived cardiomyocytes. *Stem cell reviews*. 2011;7:976-86.

88. Denning C, Borgdorff V, Crutchley J, Firth KS, George V, Kalra S, Kondrashov A, Hoang MD, Mosqueira D, Patel A, Prodanov L, Rajamohan D, Skarnes WC, Smith JG and Young LE. Cardiomyocytes from human pluripotent stem cells: From laboratory curiosity to industrial biomedical platform. *Biochimica et biophysica acta*. 2016;1863:1728-48.

89. Lieu DK, Liu J, Siu CW, McNerney GP, Tse HF, Abu-Khalil A, Huser T and Li RA. Absence of transverse tubules contributes to non-uniform Ca(2+) wavefronts in mouse and human embryonic stem cell-derived cardiomyocytes. *Stem cells and development*. 2009;18:1493-500.

90. Brette F and Orchard C. T-tubule function in mammalian cardiac myocytes. *Circulation research*. 2003;92:1182-92.

91. Gherghiceanu M, Barad L, Novak A, Reiter I, Itskovitz-Eldor J, Binah O and Popescu LM. Cardiomyocytes derived from human embryonic and induced pluripotent stem cells: comparative ultrastructure. *Journal of cellular and molecular medicine*. 2011;15:2539-51.

92. Soeller C and Cannell MB. Examination of the transverse tubular system in living cardiac rat myocytes by 2-photon microscopy and digital image-processing techniques. *Circulation research*. 1999;84:266-75.

93. Jayasinghe I, Crossman D, Soeller C and Cannell M. Comparison of the organization of T-tubules, sarcoplasmic reticulum and ryanodine receptors in rat and human ventricular myocardium. *Clinical and experimental pharmacology & physiology*. 2012;39:469-76.

94. Manfra O, Frisk M and Louch WE. Regulation of Cardiomyocyte T-Tubular Structure: Opportunities for Therapy. *Current heart failure reports*. 2017;14:167-178.

95. Kawai M, Hussain M and Orchard CH. Excitation-contraction coupling in rat ventricular myocytes after formamide-induced detubulation. *The American journal of physiology*. 1999;277:H603-9.

96. Brette F, Komukai K and Orchard CH. Validation of formamide as a detubulation agent in isolated rat cardiac cells. *American journal of physiology Heart and circulatory physiology*. 2002;283:H1720-8.

97. Christe G. Localization of K(+) channels in the tubules of cardiomyocytes as suggested by the parallel decay of membrane capacitance, IK(1) and IK(ATP) during culture and by delayed IK(1) response to barium. *Journal of molecular and cellular cardiology*. 1999;31:2207-13.

98. Komukai K, Brette F, Yamanushi TT and Orchard CH. K(+) current distribution in rat sub-epicardial ventricular myocytes. *Pflugers Archiv : European journal of physiology*. 2002;444:532-8.

99. Clark RB, Tremblay A, Melnyk P, Allen BG, Giles WR and Fiset C. T-tubule localization of the inward-rectifier K(+) channel in mouse ventricular myocytes: a role in K(+) accumulation. *The Journal of physiology*. 2001;537:979-92.

100. Mitcheson JS, Hancox JC and Levi AJ. Action potentials, ion channel currents and transverse tubule density in adult rabbit ventricular myocytes maintained for 6 days in cell culture. *Pflugers Archiv : European journal of physiology*. 1996;431:814-27.

101. Goversen B, van der Heyden MAG, van Veen TAB and de Boer TP. The immature electrophysiological phenotype of iPSC-CMs still hampers in vitro drug screening: Special focus on IK1. *Pharmacology & therapeutics*. 2018;183:127-136.

102. Satin J, Itzhaki I, Rapoport S, Schroder EA, Izu L, Arbel G, Beyar R, Balke CW, Schiller J and Gepstein L. Calcium handling in human embryonic stem cell-derived cardiomyocytes. *Stem cells (Dayton, Ohio)*. 2008;26:1961-72.

103. Snir M, Kehat I, Gepstein A, Coleman R, Itskovitz-Eldor J, Livne E and Gepstein L. Assessment of the ultrastructural and proliferative properties of human embryonic stem cell-derived cardiomyocytes. *American journal of physiology Heart and circulatory physiology*. 2003;285:H2355-63.

104. Mannhardt I, Breckwoldt K, Letuffe-Breniere D, Schaaf S, Schulz H, Neuber C, Benzin A, Werner T, Eder A, Schulze T, Klampe B, Christ T, Hirt MN, Huebner N, Moretti A, Eschenhagen T and Hansen A. Human Engineered Heart Tissue: Analysis of Contractile Force. *Stem cell reports*. 2016;7:29-42.

105. Shadrin IY, Allen BW, Qian Y, Jackman CP, Carlson AL, Juhas ME and Bursac N. Cardiopatch platform enables maturation and scale-up of human pluripotent stem cell-derived engineered heart tissues. *Nature communications*. 2017;8:1825.

106. Ronaldson-Bouchard K, Ma SP, Yeager K, Chen T, Song L, Sirabella D, Morikawa K, Teles D, Yazawa M and Vunjak-Novakovic G. Advanced maturation of human cardiac tissue grown from pluripotent stem cells. *Nature*. 2018;556:239-243.

107. Mathew T, Williams L, Navaratnam G, Rana B, Wheeler R, Collins K, Harkness A, Jones R, Knight D, O'Gallagher K, Oxborough D, Ring L, Sandoval J, Stout M, Sharma V and Steeds RP. Diagnosis and assessment of dilated cardiomyopathy: a guideline protocol from the British Society of Echocardiography. *Echo research and practice*. 2017;4:G1-g13.

108. McNally EM and Mestroni L. Dilated Cardiomyopathy: Genetic Determinants and Mechanisms. *Circulation research*. 2017;121:731-748.

109. Morales A, Painter T, Li R, Siegfried JD, Li D, Norton N and Hershberger RE. Rare variant mutations in pregnancy-associated or peripartum cardiomyopathy. *Circulation*. 2010;121:2176-82.

110. Ware JS, Li J, Mazaika E, Yasso CM, DeSouza T, Cappola TP, Tsai EJ, Hilfiker-Kleiner D, Kamiya CA, Mazzarotto F, Cook SA, Halder I, Prasad SK, Pisarcik J, Hanley-Yanez K, Alharethi R, Damp J, Hsich E, Elkayam U, Sheppard R, Kealey A, Alexis J, Ramani G, Safirstein J, Boehmer J, Pauly DF, Wittstein IS, Thohan V, Zucker MJ, Liu P, Gorcsan J, 3rd, McNamara DM, Seidman CE, Seidman JG and Arany Z. Shared Genetic Predisposition in

Peripartum and Dilated Cardiomyopathies. *The New England journal of medicine*. 2016;374:233-41.

111. Michels VV, Moll PP, Miller FA, Tajik AJ, Chu JS, Driscoll DJ, Burnett JC, Rodeheffer RJ, Chesebro JH and Tazelaar HD. The frequency of familial dilated cardiomyopathy in a series of patients with idiopathic dilated cardiomyopathy. *The New England journal of medicine*. 1992;326:77-82.

112. Burkett EL and Hershberger RE. Clinical and genetic issues in familial dilated cardiomyopathy. *Journal of the American College of Cardiology*. 2005;45:969-81.

113. Hershberger RE, Norton N, Morales A, Li D, Siegfried JD and Gonzalez-Quintana J. Coding sequence rare variants identified in MYBPC3, MYH6, TPM1, TNNC1, and TNNI3 from 312 patients with familial or idiopathic dilated cardiomyopathy. *Circulation Cardiovascular genetics*. 2010;3:155-61.

114. Kinnamon DD, Morales A, Bowen DJ, Burke W and Hershberger RE. Toward Genetics-Driven Early Intervention in Dilated Cardiomyopathy: Design and Implementation of the DCM Precision Medicine Study. *Circulation Cardiovascular genetics*. 2017;10.

115. Sun N, Yazawa M, Liu J, Han L, Sanchez-Freire V, Abilez OJ, Navarrete EG, Hu S, Wang L, Lee A, Pavlovic A, Lin S, Chen R, Hajjar RJ, Snyder MP, Dolmetsch RE, Butte MJ, Ashley EA, Longaker MT, Robbins RC and Wu JC. Patient-specific induced pluripotent stem cells as a model for familial dilated cardiomyopathy. *Science translational medicine*. 2012;4:130ra47.

116. Wu H, Lee J, Vincent LG, Wang Q, Gu M, Lan F, Churko JM, Sallam KI, Matsa E, Sharma A, Gold JD, Engler AJ, Xiang YK, Bers DM and Wu JC. Epigenetic Regulation of Phosphodiesterases 2A and 3A Underlies Compromised beta-Adrenergic Signaling in an iPSC Model of Dilated Cardiomyopathy. *Cell stem cell*. 2015;17:89-100.

117. Hinson JT, Chopra A, Nafissi N, Polacheck WJ, Benson CC, Swist S, Gorham J, Yang L, Schafer S, Sheng CC, Haghighi A, Homsy J, Hubner N, Church G, Cook SA, Linke WA, Chen CS, Seidman JG and Seidman CE. HEART DISEASE. Titin mutations in iPS cells define sarcomere insufficiency as a cause of dilated cardiomyopathy. *Science (New York, NY)*. 2015;349:982-6.

118. Broughton KM, Li J, Sarmah E, Warren CM, Lin YH, Henze MP, Sanchez-Freire V, Solaro RJ and Russell B. A myosin activator improves actin assembly and sarcomere function of human-induced pluripotent stem cell-derived cardiomyocytes with a troponin T point mutation. *American journal of physiology Heart and circulatory physiology*. 2016;311:H107-17.

119. Siu CW, Lee YK, Ho JC, Lai WH, Chan YC, Ng KM, Wong LY, Au KW, Lau YM, Zhang J, Lay KW, Colman A and Tse HF. Modeling of lamin A/C mutation premature cardiac aging using patient-specific induced pluripotent stem cells. *Aging*. 2012;4:803-822.

120. Lee YK, Lau YM, Cai ZJ, Lai WH, Wong LY, Tse HF, Ng KM and Siu CW. Modeling Treatment Response for Lamin A/C Related Dilated Cardiomyopathy in Human Induced Pluripotent Stem Cells. *Journal of the American Heart Association*. 2017;6.

121. Karakikes I, Stillitano F, Nonnenmacher M, Tzimas C, Sanoudou D, Termglinchan V, Kong CW, Rushing S, Hansen J, Ceholski D, Kolokathis F, Kremastinos D, Katoulis A, Ren L, Cohen N, Gho JM, Tsiapras D, Vink A, Wu JC, Asselbergs FW, Li RA, Hulot JS, Kranias EG and Hajjar RJ. Correction of human phospholamban R14del mutation associated with cardiomyopathy using targeted nucleases and combination therapy. *Nature communications*. 2015;6:6955.

122. Wyles SP, Li X, Hrstka SC, Reyes S, Oommen S, Beraldi R, Edwards J, Terzic A, Olson TM and Nelson TJ. Modeling structural and functional deficiencies of RBM20 familial dilated cardiomyopathy using human induced pluripotent stem cells. *Human molecular genetics*. 2016;25:254-65.

123. Streckfuss-Bomeke K, Tiburcy M, Fomin A, Luo X, Li W, Fischer C, Ozcelik C, Perrot A, Sossalla S, Haas J, Vidal RO, Rebs S, Khadjeh S, Meder B, Bonn S, Linke WA, Zimmermann WH, Hasenfuss G and Guan K. Severe DCM phenotype of patient harboring RBM20 mutation S635A can be modeled by patient-specific induced pluripotent stem cell-derived cardiomyocytes. *Journal of molecular and cellular cardiology*. 2017;113:9-21.

124. Parikh SS, Blackwell DJ, Gomez-Hurtado N, Frisk M, Wang L, Kim K, Dahl CP, Fiane AE, Tonnessen T, Kryshtal DO, Louch WE and Knollmann BC. Thyroid and Glucocorticoid Hormones Promote Functional T-tubule Development in Human-Induced Pluripotent Stem Cell Derived Cardiomyocytes. *Circulation research*. 2017.

125. Pugh TJ, Kelly MA, Gowrisankar S, Hynes E, Seidman MA, Baxter SM, Bowser M, Harrison B, Aaron D, Mahanta LM, Lakdawala NK, McDermott G, White ET, Rehm HL, Lebo M and Funke BH. The landscape of genetic variation in dilated cardiomyopathy as surveyed by clinical DNA sequencing. *Genetics in medicine : official journal of the American College of Medical Genetics*. 2014;16:601-8.

126. Scharner J, Gnocchi VF, Ellis JA and Zammit PS. Genotype-phenotype correlations in laminopathies: how does fate translate? *Biochemical Society transactions*. 2010;38:257-62.

127. Hasselberg NE, Haland TF, Saberniak J, Brekke PH, Berge KE, Leren TP, Edvardsen T and Haugaa KH. Lamin A/C cardiomyopathy: young onset, high penetrance, and frequent need for heart transplantation. *European heart journal*. 2018;39:853-860.

128. van Berlo JH, de Voogt WG, van der Kooi AJ, van Tintelen JP, Bonne G, Yaou RB, Duboc D, Rossenbacker T, Heidbuchel H, de Visser M, Crijns HJ and Pinto YM. Meta-analysis of clinical characteristics of 299 carriers of LMNA gene mutations: do lamin A/C mutations portend a high risk of sudden death? *Journal of molecular medicine (Berlin, Germany)*. 2005;83:79-83.

129. Perovanovic J, Dell'Orso S, Gnochi VF, Jaiswal JK, Sartorelli V, Vigouroux C, Mamchaoui K, Mouly V, Bonne G and Hoffman EP. Laminopathies disrupt epigenomic developmental programs and cell fate. *Science translational medicine*. 2016;8:335ra58.

130. Brayson D and Shanahan CM. Current insights into LMNA cardiomyopathies: Existing models and missing LINCs. *Nucleus (Austin, Tex)*. 2017;8:17-33.

131. Davidson PM and Lammerding J. Broken nuclei--lamins, nuclear mechanics, and disease. *Trends in cell biology*. 2014;24:247-56.

132. Stroud MJ, Banerjee I, Veevers J and Chen J. Linker of nucleoskeleton and cytoskeleton complex proteins in cardiac structure, function, and disease. *Circulation research*. 2014;114:538-48.

133. Ouellette AC, Mathew J, Manickaraj AK, Manase G, Zahavich L, Wilson J, George K, Benson L, Bowdin S and Mital S. Clinical genetic testing in pediatric cardiomyopathy: Is bigger better? *Clinical genetics*. 2018;93:33-40.

134. Ackerman MJ. Genetic purgatory and the cardiac channelopathies: Exposing the variants of uncertain/unknown significance issue. *Heart rhythm : the official journal of the Heart Rhythm Society*. 2015;12:2325-31.

135. Cadar AG, Feaster TK, Durbin MD and Hong CC. Production of Single Contracting Human Induced Pluripotent Stem Cell-Derived Cardiomyocytes: Matrigel Mattress Technique. *Current protocols in stem cell biology*. 2017;42:4a.14.1-4a.14.7.

136. Saj M, Bilinska ZT, Tarnowska A, Sioma A, Bolongo P, Sobieszczanska-Malek M, Michalak E, Golen D, Mazurkiewicz L, Malek L, Walczak E, Fidzianska A, Grzybowski J, Przybylski A, Zielinski T, Korewicki J, Tesson F and Ploski R. LMNA mutations in Polish patients with dilated cardiomyopathy: prevalence, clinical characteristics, and in vitro studies. *BMC medical genetics*. 2013;14:55.

137. Chen W, Huo J, Ma A, Bai L and Liu P. A novel mutation of the LMNA gene in a family with dilated cardiomyopathy, conduction system disease, and sudden cardiac death of young females. *Molecular and cellular biochemistry*. 2013;382:307-11.

138. Arbustini EA, Pasotti M, Pilotto A, Repetto A, Grasso M and Diegoli M. Gene symbol: CMD1A. Disease: Dilated cardiomyopathy associated with conduction system disease. *Human genetics*. 2005;117:295.

139. Lek M, Karczewski KJ, Minikel EV, Samocha KE, Banks E, Fennell T, O'Donnell-Luria AH, Ware JS, Hill AJ, Cummings BB, Tukiainen T, Birnbaum DP, Kosmicki JA, Duncan LE, Estrada K, Zhao F, Zou J, Pierce-Hoffman E, Berghout J, Cooper DN, Deflaux N, DePristo M, Do R, Flannick J, Fromer M, Gauthier L, Goldstein J, Gupta N, Howrigan D, Kiezun A, Kurki MI, Moonshine AL, Natarajan P, Orozco L, Peloso GM, Poplin R, Rivas MA, Ruano-Rubio V, Rose SA, Ruderfer DM, Shakir K, Stenson PD, Stevens C, Thomas BP, Tiao G, Tusie-Luna MT, Weisburd B, Won HH, Yu D, Altshuler DM, Ardissino D, Boehnke M, Danesh J, Donnelly S, Elosua R, Florez JC, Gabriel SB, Getz G, Glatt SJ, Hultman CM, Kathiresan S, Laakso M, McCarroll S, McCarthy MI, McGovern D, McPherson R, Neale BM, Palotie A, Purcell SM, Saleheen D, Scharf JM, Sklar P, Sullivan PF, Tuomilehto J, Tsuang MT, Watkins HC, Wilson JG, Daly MJ and MacArthur DG. Analysis of protein-coding genetic variation in 60,706 humans. *Nature*. 2016;536:285-91.

140. Wang L, Kryshtal DO, Kim K, Parikh S, Cadar AG, Bersell KR, He H, Pinto JR and Knollmann BC. Myofilament Calcium-Buffering Dependent Action Potential Triangulation in

Human-Induced Pluripotent Stem Cell Model of Hypertrophic Cardiomyopathy. *Journal of the American College of Cardiology*. 2017;70:2600-2602.

141. Laurini E, Martinelli V, Lanzicher T, Puzzi L, Borin D, Chen SN, Long CS, Lee P, Mestroni L, Taylor MRG, Sbaizero O and Pricl S. Biomechanical defects and rescue of cardiomyocytes expressing pathologic nuclear lamins. *Cardiovascular research*. 2018.

142. Scharner J, Brown CA, Bower M, Iannaccone ST, Khatri IA, Escolar D, Gordon E, Felice K, Crowe CA, Grosmann C, Meriggioli MN, Asamoah A, Gordon O, Gnocchi VF, Ellis JA, Mendell JR and Zammit PS. Novel LMNA mutations in patients with Emery-Dreifuss muscular dystrophy and functional characterization of four LMNA mutations. *Human mutation*. 2011;32:152-67.

143. Arimura T, Helbling-Leclerc A, Massart C, Varnous S, Niel F, Lacene E, Fromes Y, Toussaint M, Mura AM, Keller DI, Amthor H, Isnard R, Malissen M, Schwartz K and Bonne G. Mouse model carrying H222P-Lmna mutation develops muscular dystrophy and dilated cardiomyopathy similar to human striated muscle laminopathies. *Human molecular genetics*. 2005;14:155-69.

144. Wolf CM, Wang L, Alcalai R, Pizard A, Burgon PG, Ahmad F, Sherwood M, Branco DM, Wakimoto H, Fishman GI, See V, Stewart CL, Conner DA, Berul CI, Seidman CE and Seidman JG. Lamin A/C haploinsufficiency causes dilated cardiomyopathy and apoptosis-triggered cardiac conduction system disease. *Journal of molecular and cellular cardiology*. 2008;44:293-303.

145. Liang G and Zhang Y. Genetic and epigenetic variations in iPSCs: potential causes and implications for application. *Cell stem cell*. 2013;13:149-59.

146. Kumar S, Baldinger SH, Gandjbakhch E, Maury P, Sellal JM, Androulakis AF, Waintraub X, Charron P, Rollin A, Richard P, Stevenson WG, Macintyre CJ, Ho CY, Thompson T, Vohra JK, Kalman JM, Zeppenfeld K, Sacher F, Tedrow UB and Lakdawala NK. Long-Term Arrhythmic and Nonarrhythmic Outcomes of Lamin A/C Mutation Carriers. *Journal of the American College of Cardiology*. 2016;68:2299-2307.

147. Carmosino M, Gerbino A, Schena G, Procino G, Miglionico R, Forleo C, Favale S and Svelto M. The expression of Lamin A mutant R321X leads to endoplasmic reticulum stress with aberrant Ca(2+) handling. *Journal of cellular and molecular medicine*. 2016;20:2194-2207.

148. Li YF and Wang X. The role of the proteasome in heart disease. *Biochimica et biophysica acta*. 2011;1809:141-9.

149. Sieprath T, Darwiche R and De Vos WH. Lamins as mediators of oxidative stress. *Biochemical and biophysical research communications*. 2012;421:635-9.

150. Sieprath T, Corne TD, Nooteboom M, Grootaert C, Rajkovic A, Buysschaert B, Robijns J, Broers JL, Ramaekers FC, Koopman WJ, Willems PH and De Vos WH. Sustained accumulation of prelamin A and depletion of lamin A/C both cause oxidative stress and mitochondrial dysfunction but induce different cell fates. *Nucleus (Austin, Tex)*. 2015;6:236-46.

151. Mirza M, Marston S, Willott R, Ashley C, Mogensen J, McKenna W, Robinson P, Redwood C and Watkins H. Dilated cardiomyopathy mutations in three thin filament regulatory proteins result in a common functional phenotype. *The Journal of biological chemistry*. 2005;280:28498-506.

152. Venkatraman G, Harada K, Gomes AV, Kerrick WG and Potter JD. Different functional properties of troponin T mutants that cause dilated cardiomyopathy. *The Journal of biological chemistry*. 2003;278:41670-6.

153. Carballo S, Robinson P, Otway R, Fatkin D, Jongbloed JD, de Jonge N, Blair E, van Tintelen JP, Redwood C and Watkins H. Identification and functional characterization of cardiac troponin I as a novel disease gene in autosomal dominant dilated cardiomyopathy. *Circulation research*. 2009;105:375-82.

154. Willott RH, Gomes AV, Chang AN, Parvatiyar MS, Pinto JR and Potter JD. Mutations in Troponin that cause HCM, DCM AND RCM: what can we learn about thin filament function? *Journal of molecular and cellular cardiology*. 2010;48:882-92.

155. Kolanowski TJ, Antos CL and Guan K. Making human cardiomyocytes up to date: Derivation, maturation state and perspectives. *International journal of cardiology*. 2017.

156. Kamakura T, Makiyama T, Sasaki K, Yoshida Y, Wuriyanghai Y, Chen J, Hattori T, Ohno S, Kita T, Horie M, Yamanaka S and Kimura T. Ultrastructural maturation of human-induced pluripotent stem cell-derived cardiomyocytes in a long-term culture. *Circulation journal : official journal of the Japanese Circulation Society*. 2013;77:1307-14.

157. Lundy SD, Zhu WZ, Regnier M and Laflamme MA. Structural and functional maturation of cardiomyocytes derived from human pluripotent stem cells. *Stem cells and development*. 2013;22:1991-2002.

158. Ribeiro AJ, Ang YS, Fu JD, Rivas RN, Mohamed TM, Higgs GC, Srivastava D and Pruitt BL. Contractility of single cardiomyocytes differentiated from pluripotent stem cells depends on physiological shape and substrate stiffness. *Proceedings of the National Academy of Sciences of the United States of America*. 2015;112:12705-10.

159. Pioner JM, Racca AW, Klaiman JM, Yang KC, Guan X, Pabon L, Muskheli V, Zaunbrecher R, Macadangdang J, Jeong MY, Mack DL, Childers MK, Kim DH, Tesi C, Poggesi C, Murry CE and Regnier M. Isolation and Mechanical Measurements of Myofibrils from Human Induced Pluripotent Stem Cell-Derived Cardiomyocytes. *Stem cell reports*. 2016;6:885-96.

160. Sun X and Nunes SS. Bioengineering Approaches to Mature Human Pluripotent Stem Cell-Derived Cardiomyocytes. *Frontiers in cell and developmental biology*. 2017;5:19.

161. Jacot JG, McCulloch AD and Omens JH. Substrate stiffness affects the functional maturation of neonatal rat ventricular myocytes. *Biophysical journal*. 2008;95:3479-87.

162. Huethorst E, Hortigon M, Zamora-Rodriguez V, Reynolds PM, Burton F, Smith G and Gadegaard N. Enhanced Human-Induced Pluripotent Stem Cell Derived Cardiomyocyte Maturation Using a Dual Microgradient Substrate. *ACS biomaterials science & engineering*. 2016;2:2231-2239.

163. Herron TJ, Rocha AM, Campbell KF, Ponce-Balbuena D, Willis BC, Guerrero-Serna G, Liu Q, Klos M, Musa H, Zarzoso M, Bizy A, Furness J, Anumonwo J, Mironov S and Jalife J. Extracellular Matrix-Mediated Maturation of Human Pluripotent Stem Cell-Derived Cardiac Monolayer Structure and Electrophysiological Function. *Circulation Arrhythmia and electrophysiology*. 2016;9:e003638.

164. Li M, Iismaa SE, Naqvi N, Nicks A, Husain A and Graham RM. Thyroid hormone action in postnatal heart development. *Stem cell research*. 2014;13:582-91.

165. Rog-Zielinska EA, Thomson A, Kenyon CJ, Brownstein DG, Moran CM, Szumska D, Michailidou Z, Richardson J, Owen E, Watt A, Morrison H, Forrester LM, Bhattacharya S, Holmes MC and Chapman KE. Glucocorticoid receptor is required for foetal heart maturation. *Human molecular genetics*. 2013;22:3269-82.

166. Kahaly GJ and Dillmann WH. Thyroid hormone action in the heart. *Endocrine reviews*. 2005;26:704-28.

167. White P, Burton KA, Fowden AL and Dauncey MJ. Developmental expression analysis of thyroid hormone receptor isoforms reveals new insights into their essential functions in cardiac and skeletal muscles. *FASEB journal : official publication of the Federation of American Societies for Experimental Biology*. 2001;15:1367-76.

168. Mai W, Janier MF, Allioli N, Quignodon L, Chuzel T, Flamant F and Samarut J. Thyroid hormone receptor alpha is a molecular switch of cardiac function between fetal and postnatal life. *Proceedings of the National Academy of Sciences of the United States of America*. 2004;101:10332-7.

169. Yang X, Rodriguez M, Pabon L, Fischer KA, Reinecke H, Regnier M, Sniadecki NJ, Ruohola-Baker H and Murry CE. Tri-iodo-l-thyronine promotes the maturation of human cardiomyocytes-derived from induced pluripotent stem cells. *Journal of molecular and cellular cardiology*. 2014;72:296-304.

170. Rog-Zielinska EA, Craig MA, Manning JR, Richardson RV, Gowans GJ, Dunbar DR, Gharbi K, Kenyon CJ, Holmes MC, Hardie DG, Smith GL and Chapman KE. Glucocorticoids promote structural and functional maturation of foetal cardiomyocytes: a role for PGC-1alpha. *Cell death and differentiation*. 2015;22:1106-16.

171. Oakley RH, Ren R, Cruz-Topete D, Bird GS, Myers PH, Boyle MC, Schneider MD, Willis MS and Cidlowski JA. Essential role of stress hormone signaling in cardiomyocytes for the prevention of heart disease. *Proceedings of the National Academy of Sciences of the United States of America*. 2013;110:17035-40.

172. Birket MJ, Ribeiro MC, Kosmidis G, Ward D, Leitoguinho AR, van de Pol V, Dambrot C, Devalla HD, Davis RP, Mastroberardino PG, Atsma DE, Passier R and Mummery CL. Contractile Defect Caused by Mutation in MYBPC3 Revealed under Conditions Optimized for Human PSC-Cardiomyocyte Function. *Cell reports*. 2015;13:733-45.

173. Ribeiro MC, Tertoolen LG, Guadix JA, Bellin M, Kosmidis G, D'Aniello C, Monshouwer-Kloots J, Goumans MJ, Wang YL, Feinberg AW, Mummery CL and Passier R. Functional maturation of human pluripotent stem cell derived cardiomyocytes in vitro--correlation between contraction force and electrophysiology. *Biomaterials*. 2015;51:138-50.

174. Burridge PW, Matsa E, Shukla P, Lin ZC, Churko JM, Ebert AD, Lan F, Diecke S, Huber B, Mordwinkin NM, Plews JR, Abilez OJ, Cui B, Gold JD and Wu JC. Chemically defined generation of human cardiomyocytes. *Nature methods*. 2014;11:855-60.

175. Frisk M, Koivumaki JT, Norseng PA, Maleckar MM, Sejersted OM and Louch WE. Variable t-tubule organization and Ca2+ homeostasis across the atria. *American journal of physiology Heart and circulatory physiology*. 2014;307:H609-20.

176. Yndestad A, Finsen AV, Ueland T, Husberg C, Dahl CP, Oie E, Vinge LE, Sjaastad I, Sandanger O, Ranheim T, Dickstein K, Kjekshus J, Damas JK, Fiane AE, Hilfiker-Kleiner D, Lipp M, Gullestad L, Christensen G and Aukrust P. The homeostatic chemokine CCL21 predicts mortality and may play a pathogenic role in heart failure. *PloS one*. 2012;7:e33038.

177. Picht E, Zima AV, Blatter LA and Bers DM. SparkMaster: automated calcium spark analysis with ImageJ. *American journal of physiology Cell physiology*. 2007;293:C1073-81.

178. Ziman AP, Gomez-Viquez NL, Bloch RJ and Lederer WJ. Excitation-contraction coupling changes during postnatal cardiac development. *Journal of molecular and cellular cardiology*. 2010;48:379-86.

179. Cheng H, Lederer WJ and Cannell MB. Calcium sparks: elementary events underlying excitation-contraction coupling in heart muscle. *Science (New York, NY)*. 1993;262:740-4.

180. Zhang GQ, Wei H, Lu J, Wong P and Shim W. Identification and characterization of calcium sparks in cardiomyocytes derived from human induced pluripotent stem cells. *PloS one*. 2013;8:e55266.

181. Li S, Cheng H, Tomaselli GF and Li RA. Mechanistic basis of excitation-contraction coupling in human pluripotent stem cell-derived ventricular cardiomyocytes revealed by Ca2+ spark characteristics: direct evidence of functional Ca2+-induced Ca2+ release. *Heart rhythm : the official journal of the Heart Rhythm Society*. 2014;11:133-40.

182. Zhu WZ, Santana LF and Laflamme MA. Local control of excitation-contraction coupling in human embryonic stem cell-derived cardiomyocytes. *PloS one*. 2009;4:e5407.

183. Fatima A, Xu G, Shao K, Papadopoulos S, Lehmann M, Arnaiz-Cot JJ, Rosa AO, Nguemo F, Matzkies M, Dittmann S, Stone SL, Linke M, Zechner U, Beyer V, Hennies HC, Rosenkranz S, Klauke B, Parwani AS, Haverkamp W, Pfitzer G, Farr M, Cleemann L, Morad M, Milting H,

Hescheler J and Saric T. In vitro modeling of ryanodine receptor 2 dysfunction using human induced pluripotent stem cells. *Cellular physiology and biochemistry : international journal of experimental cellular physiology, biochemistry, and pharmacology*. 2011;28:579-92.

184. Boyett MR and Jewell BR. Analysis of the effects of changes in rate and rhythm upon electrical activity in the heart. *Progress in biophysics and molecular biology*. 1980;36:1-52.

185. Fauconnier J, Thireau J, Reiken S, Cassan C, Richard S, Matecki S, Marks AR and Lacampagne A. Leaky RyR2 trigger ventricular arrhythmias in Duchenne muscular dystrophy. *Proceedings of the National Academy of Sciences of the United States of America*. 2010;107:1559-64.